

QUANTUM INTERFERENCE EFFECTS IN PRECISION
SPECTROSCOPY OF HELIUM FINE STRUCTURE

ALAIN MARSMAN

A DISSERTATION SUBMITTED TO THE FACULTY OF GRADUATE
STUDIES
IN PARTIAL FULFILMENT OF THE REQUIREMENTS
FOR THE DEGREE OF

DOCTOR OF PHILOSOPHY

GRADUATE PROGRAM IN PHYSICS AND ASTRONOMY
YORK UNIVERSITY
TORONTO, ONTARIO
JUNE 2016

© Alain Marsman, 2016

Abstract

Precision spectroscopy of atomic helium fine structure provides a means of testing fundamental few-body theory as well as determining the fine-structure constant α , which characterizes electromagnetic interactions in nature. Progress in both experiment and theory has led to increasingly precise values for the splittings between the $n=2$ triplet P states of helium, and at the current level of uncertainty, quantum interference can be a significant source of systematic error in measurements of the fine-structure intervals.

This work deals with these quantum interference effects, which are due to coherent excitation of the atom to multiple neighboring states, and may result in substantial shifts in the measured positions of resonance line centers, even if the transition frequencies of adjacent resonances are thousands of natural widths away. The scale of the shifts depends on the measurement technique and the experimental parameters, and therefore a selection of the most precise measurements of the helium fine-structure intervals are analyzed in order to calculate the relevant interference effects. The inclusion of these interference shifts leads to greater consistency

between values obtained by several different experimental techniques, and furthers the program of obtaining a high-precision value of the fine-structure constant by comparison between experiment and theory.

Acknowledgements

I am grateful to my supervisors, Professors Marko Horbatsch and Eric Hessels, for inviting me to be a part of this interesting and fruitful research project, and for their guidance and patience over the past five years.

I would also like to thank Prof. Tom Kirchner, and the members of my examination committee, for their valuable comments, suggestions, and encouragement.

Thanks are due to Prof. Roman Koniuk for his recommendation that enabled me to return to graduate studies, and of course to Marlene Caplan, for all her support and patient help in navigating through the many practical details of my graduate career at York.

Table of Contents

Abstract	ii
Acknowledgements	iv
Table of Contents	v
List of Tables	viii
List of Figures	ix
1 Introduction	1
1.1 Helium Energy Levels and 2^3P Fine Structure	3
1.2 Interference Shifts	7
2 Quantum Interference in Precision Spectroscopy	12
2.1 Spectral Interference	12
2.2 The Four-level System	15
2.3 Density-matrix Equations	16

2.4	Reduced Equations	20
2.5	Application to Helium Spectroscopy	24
3	Laser Spectroscopy in a Narrow Thermal Beam	28
3.1	Measurement Technique	28
3.2	Theoretical Description	31
3.3	Correction to the 2^3P_1 — 2^3P_2 Interval	37
4	Saturated-fluorescence Spectroscopy	42
4.1	Measurement Technique	43
4.2	Theoretical Description	46
4.2.1	Density-matrix Equations	46
4.2.2	Reduced Equations	49
4.3	Fluorescence Lineshapes	51
4.4	AC-Stark Shifts	55
4.5	Interference Shifts	61
4.5.1	Scale and Sign of Interference Shifts	64
5	Saturated-absorption Spectroscopy	68
5.1	Measurement Technique	68
5.1.1	Systematic Effects	71
5.2	Theoretical Description	73

5.3	Absorption Lineshapes	75
5.4	Interference Shifts	81
5.5	Correction to the 2^3P_1 — 2^3P_2 Interval	84
6	Microwave Spectroscopy	87
6.1	Measurement Technique	88
6.2	Theoretical Description	90
6.3	Single Microwave Pulse Shifts	96
6.4	Microwave SOF Shifts	100
7	Conclusion	107
A	Master Equations	113
A.1	The Two-level Atom	114
A.1.1	Rotating-wave Approximation	115
A.1.2	Corotating Frame	116
A.1.3	Density-matrix Equations	117
A.2	The Three-level Atom	117
A.3	The Four-level Atom	119
A.4	General Systems	122
A.5	Rabi Frequency Conventions	122
B	Matrix Elements	124

List of Tables

4.1	AC-Stark and interference shifts for F_0 and $F_{\pm 1}$ fluorescence	60
4.2	Dependence of AC-Stark and interference shifts on beam Doppler width	63
6.1	Single-microwave-pulse frequency shifts extrapolated to zero field intensity	100
6.2	SOF frequency shifts extrapolated to zero microwave intensity . . .	105
B.1	Electric-dipole matrix elements between metastable and excited triplet states.	126

List of Figures

1.1	Energy level diagram for atomic helium, including the $n=2$ triplet state fine-structure.	4
1.2	Measurements and theory for the 2^3P fine-structure intervals in helium.	9
2.1	The relative shift in the line center of a resonance due to a neighboring resonance.	14
2.2	A four-level model atom illustrating quantum interference between resonant and non-resonant transitions.	15
2.3	Measurement of the 2^3S_1 -to- 2^3P_1 resonance as a four-level system	26
3.1	He triplet transitions driven by a circularly-polarized laser field	29
3.2	Intensity profile for an atom traveling through a Gaussian laser beam.	34
3.3	Interference shifts in transition lineshapes	35
3.4	Dependence of interference shifts for the 2^3P_1 — 2^3P_2 interval on laser intensity and interaction time.	38
3.5	Correction to the 2^3P_1 — 2^3P_2 fine-structure interval	40

4.1	Saturated-fluorescence measurement of the 2^3S_1 -to- 2^3P_1 and 2^3S_1 -to- 2^3P_0 resonances	44
4.2	F_0 fluorescence signals for the 2^3S_1 -to- 2^3P_1 resonance	53
4.3	Amplitude and width of the 2^3S_1 -to- 2^3P_1 saturated-fluorescence dip	55
4.4	Convergence of AC-Stark and interference shifts of the 2^3S_1 -to- 2^3P_1 saturated-fluorescence dips	58
4.5	Contour graphs for AC-Stark and interference shifts versus interaction times T_L and laser intensities I_0	61
5.1	Saturated-absorption measurement of the $2^3S_{1,m_J=1}$ -to- $2^3P_{1,m_J=1}$ transition	70
5.2	Phase- and Doppler-averaged saturated-absorption line shapes for the 2^3S_1 -to- 2^3P_1 resonance	78
5.3	Shifts in the 2^3S_1 -to- 2^3P_1 resonance as a function of included Doppler groups.	79
5.4	Line widths of the 2^3S_1 -to- 2^3P_1 resonance as a function of included Doppler groups.	80
5.5	Line widths of the 2^3S_1 -to- 2^3P_1 resonance over a range of interaction times and laser intensities.	82
5.6	Shifts in the 2^3P_1 — 2^3P_2 interval over a range of interaction times and laser intensities.	84

6.1	A direct microwave measurement of the He fine-structure intervals .	89
6.2	Timing profiles for single and dual microwave pulses	91
6.3	Line shape of the 2^3P_1 -to- 2^3P_2 resonance obtained using a single microwave pulse	97
6.4	Shifts of the 2^3P_1 -to- 2^3P_2 resonance versus magnetic field amplitude	99
6.5	SOF line shape of the 2^3P_1 -to- 2^3P_2 resonance	101
6.6	SOF shifts of the 2^3P_1 -to- 2^3P_2 resonance versus magnetic field am- plitude	104
7.1	Corrected measurements for the 2^3P fine-structure intervals in helium.	108

1 Introduction

This thesis presents an analysis of quantum interference effects in precision spectroscopy of helium fine-structure. This systematic source of error is due to excitation of off-resonant transitions, and must be accounted for in order to ensure consistency between experimental values of the helium $n = 2$ triplet P fine-structure intervals, and also to make a comparison with theory possible to a high degree of accuracy.

More than fifty years ago, C. Schwartz initiated a theoretical program to calculate the fine-structure energy spacings in atomic helium [1]. This program was motivated not only by a desire to advance the quantum-electrodynamics (QED) theory of this simplest multi-electron atom, but also to obtain a more accurate value of the fine-structure constant α , which characterizes the strength of the electromagnetic interaction in nature. As he suggested, the relatively long lifetime (≈ 98 ns) and large spacing (≈ 30 GHz) of the lowest-lying helium triplet states allows measurement of the fine-structure splittings to a higher accuracy than is possible in hydrogen spectroscopy (at the time, to a level of 10^{-6}), and thus a determination of

the fine-structure constant to a part-per-million precision could be made by combining these improved experimental data with comparably-accurate theoretical values. In the intervening decades, both theoretical [2–8] and experimental [9–18] progress has been made to obtain the fine-structure intervals to ever-higher precision.

The recommended value [19] of the fine-structure constant, from the 2014 Committee on Data for Science and Technology (CODATA 2014), is $\alpha = 7.2973525664(17) \times 10^{-3}$, which has an uncertainty of less than a part per billion (ppb). This value is derived from a combination of independent determinations of α , involving a variety of physical systems, including measurement of single-particle characteristics, atomic level structure, and the electrical properties of solid-state systems. The most accurate value of the fine-structure constant to date has been obtained from a combination of theory [20] and measurements [21] of the electron’s anomalous magnetic moment, $g - 2$. The value of α has also been found by measuring the velocity and deBroglie wavelength [22] of a neutron beam to obtain the ratio h/m_n . Analogous experiments have been performed using Cesium [23, 24] and Rubidium [25] atomic recoil to measure h/m_{Cs} and h/m_{Rb} , respectively, to high precision. Probing of muonium ground-state hyperfine structure [26] is another technique used to determine α . Finally, values of α obtained from electrical measurements based on the AC-Josephson [27] and quantum-Hall [28] effects were also incorporated into the CODATA value quoted above.

Curiously, values of α derived from the fine-structure intervals themselves (which

provided the name for α) have not attained the same level of accuracy as in the above mentioned methods. A competitive determination of α using helium spectroscopy will require both a greater consistency among experimental values, and an improvement in the theoretical uncertainty than is presently the case. An analysis of interference effects will contribute to resolving the former of these constraints.

1.1 Helium Energy Levels and 2^3P Fine Structure

The schematic in Fig. 1.1 depicts the low-lying energy levels of atomic helium, including the excited $n = 2$ triplet states. The ground state is a spin singlet with electronic configuration $1s^2$, where both electrons occupy the ground state orbital, with antiparallel spins. It is denoted by 1^1S_0 , where the notation $n^{2S+1}L_J$ represents a multi-electron state with a combined spin quantum number S , combined orbital angular-momentum quantum number L (with the labels "S","P","D", etc. indicating $L = 0, 1, 2, \dots$), and total angular-momentum quantum number J . The ground state therefore has $S = 0$, $L = 0$ and $J = 0$.

In all stable excited configurations, one electron remains in the ground state, while the other occupies a higher-energy orbital. Excited states are either spin singlets ($S = 0$, with antiparallel spins) or spin triplets ($S = 1$, with parallel spins), and the two sets of states are not connected by single-photon dipole transitions. The triplet states have lower energies than the corresponding singlet states. This

is due to the symmetric nature of the triplet spin state, which necessitates an anti-symmetric spatial wavefunction, as required by the Pauli exclusion principle. The electrons in triplet states thus experience a smaller probability to be found close together than those in singlet states (which have symmetric spatial wavefunctions), remaining on average further apart in space, and therefore contributing less potential energy from the repulsive electron-electron interaction.

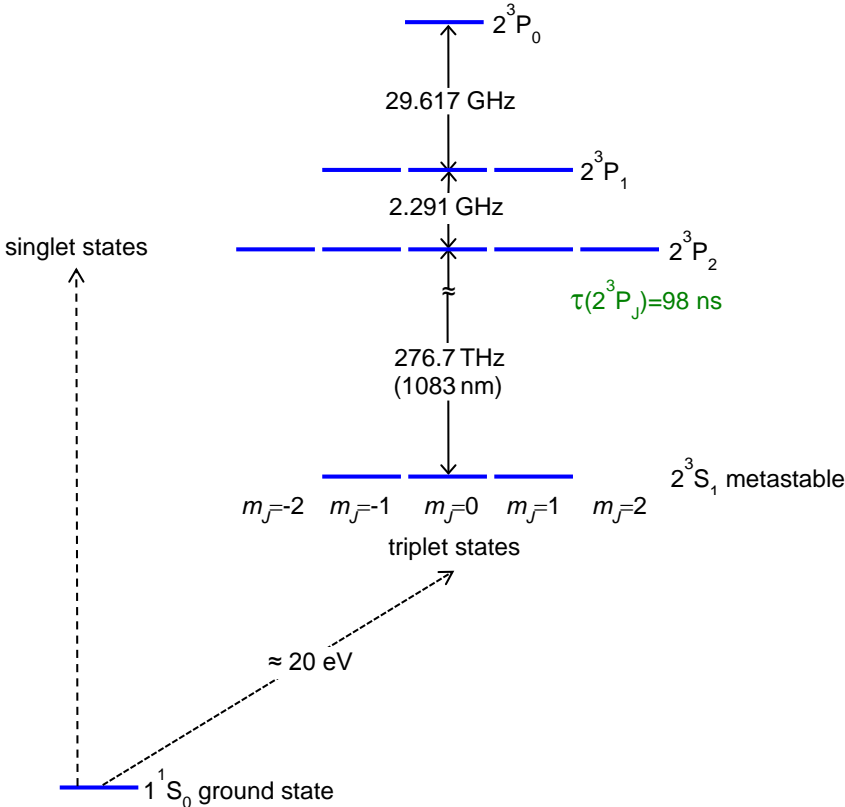


Figure 1.1: The lowest-lying energy levels of atomic helium (not to scale), showing the $n=2$ triplet states, with the 2.3- and 29.6-GHz fine-structure intervals indicated. The 2^3S_1 metastable state, with a lifetime of 7900 s, and the 2^3P excited states, with a lifetime of 98 ns, are separated by an infrared frequency transition.

The first excited triplet state of helium is the metastable 2^3S_1 state ($1s2s$), which lies about 20 eV above the ground state. It is the longest-lived neutral atomic excited state [29], with a lifetime of 7900 seconds that makes it a convenient initial state for precision spectroscopy. The next excited states are the 2^3P_J states, which are separated from the metastable state by a 277 THz (1083 nm, infrared) transition, and have a lifetime of $\tau \approx 98$ ns. This lifetime corresponds to a natural linewidth of 1.63 MHz. The 2^3P_J states are split into three fine-structure levels (with $J=0, 1$, or 2), and the differences between these energy levels are the focus of the precision spectroscopy discussed in this work. There are two independent intervals $\Delta f_{J,J'}$: the small interval $\Delta f_{1,2} \approx 2.291$ GHz, and the large interval $\Delta f_{0,1} \approx 29.617$ GHz.

The theoretical description of the helium fine-structure as a bound two-electron system expresses the intervals as perturbative series expansions in the fine-structure constant α :

$$\Delta E_{(J,J')} = m_e c^2 (\alpha^4 \mathcal{E}^{(4)} + \alpha^5 \mathcal{E}^{(5)} + \alpha^6 \mathcal{E}^{(6)} + \alpha^7 \mathcal{E}^{(7)} + \dots), \quad (1.1)$$

where $m_e c^2$ is the electron rest-energy, and the expansion coefficients $\mathcal{E}^{(n)}$ may include terms of the form $\ln(\alpha)$. The series incorporates corrections for relativistic and radiative effects such as vacuum polarization, the electron self-energy, and two-photon exchange between electrons. The current state of the art [8] includes calculations of the terms up to $m_e \alpha^7$ and $m_e \alpha^6 (m_e/M)$, where M is the mass of

the helium nucleus.

Consistency between the measured and predicted values of the smaller 2^3P_1 — 2^3P_2 splitting (2.3 GHz) provides a check of the accuracy of He QED theory, as this interval is less sensitive to the value of α due to its small size. The larger 2^3P_0 — 2^3P_1 interval (29.6 GHz) can be used to extract a value of the fine-structure constant by comparing the measured value of $\Delta f_{0,1}$ and its theoretical expansion in powers of α (Eq. (1.1)). With increasingly accurate values available for these intervals, determination of α to the level of a part per billion from a comparison between experiment and theory may soon be possible.

In order to measure the fine-structure intervals to sufficient accuracy that a comparison with theory can be made, experimental techniques must contend with numerous systematic effects. When probing an atomic sample with an applied electromagnetic field, the observed spectra are affected by both external and internal atomic degrees of freedom. The Doppler shift due to the translational motion of an atom relative to the direction of propagation of the exciting field needs to be considered, as well as the effects of atom-atom and atom-photon collisions, which can alter the velocity distribution of an atomic population. Perturbations to the atom's internal energy levels are also present, including Zeeman shifts caused by external magnetic fields, and power-dependent shifts that depend on the intensity of the applied field. All of these aforementioned effects have been carefully accounted for in precision measurements, leading to sub-kilohertz accuracy in the determined

values of the fine-structure spacings.

1.2 Interference Shifts

Given that measurements of the fine-structure intervals are now made to a precision in the hundreds of Hz, the effect of quantum interference between neighboring resonances becomes an important source of systematic error. Such interference occurs when an applied field excites two or more transitions in an atomic system, resulting in a range of interference phenomena that include narrowing of spectral lines, cancellation or phase control of spontaneous emission, and distortions of Lorentzian line shapes [30–32]. Of particular interest are shifts in the resonance line centers that are of comparable magnitude to the accuracy of the measurement. These shifts can persist in the limit of zero power of the exciting field, and may involve even quite distant off-resonant transitions, so they must be taken into account.

Quantum-mechanical interference effects originate when an applied oscillatory field that is tuned to a particular atomic resonance also drives transitions to off-resonant states. The atom can then release its absorbed energy through different decay pathways that coherently interfere with each other to cause distortions in the line shape, which manifest themselves as shifts in the measured center of the resonance profile. Analytical studies [33, 34] of three- and four-level model atoms interacting with a simple sinusoidal pulse of finite duration have demonstrated sig-

nificant shifts in the line shapes, even when neighboring resonances are separated by many natural line widths. These shifts remain even in the limit of zero field intensity, and have a scale that depends on the width of the resonance, the separation between the neighboring states, and also on the specific observable used to construct the resonance profile. For realistic experimental situations, where more atomic levels are involved, and the applied field has a more complicated time-dependent form, a numerical approach is required to simulate the specific details of a particular measurement technique.

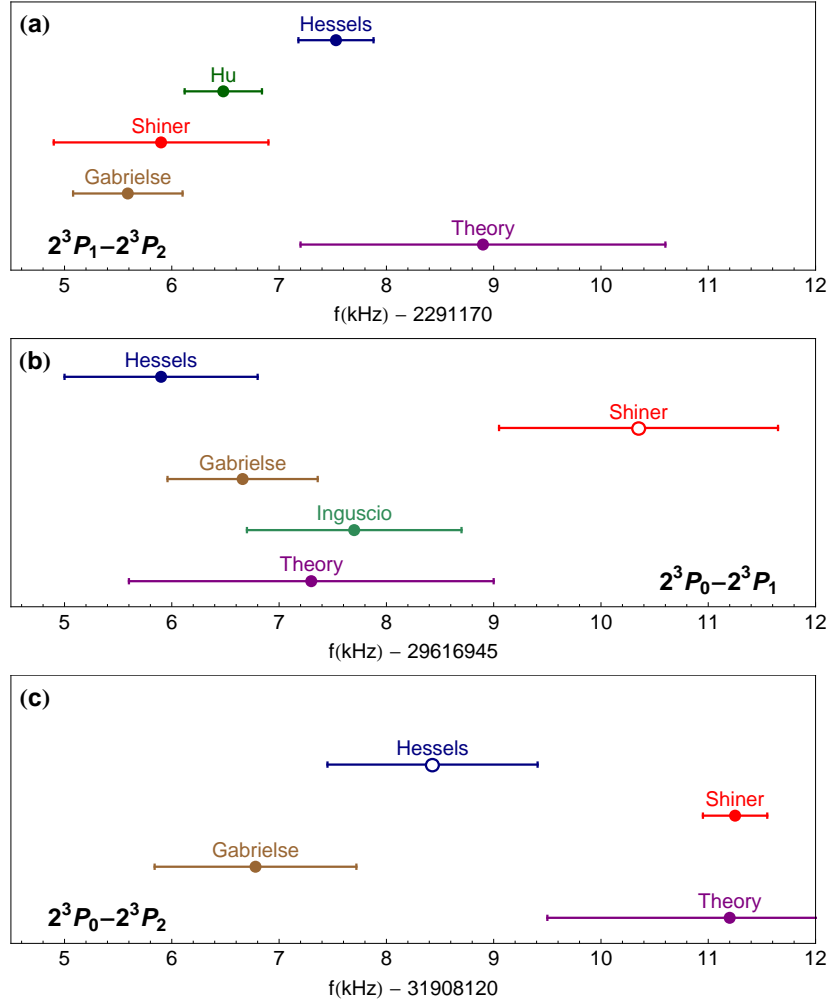


Figure 1.2: Measurements and theory for the 2^3P fine-structure intervals in helium. The measurements of the $2^3P_1-2^3P_2$, $2^3P_0-2^3P_1$, and $2^3P_0-2^3P_2$ intervals are shown in (a), (b), and (c) respectively, with points labeled according to the group performing the experiment. Filled symbols denote direct measurements, while open symbols represent inferred values based on measurements of the other two intervals. The points labeled Theory show the calculations of Pachucki and Yerokhin [8] adjusted for the CODATA 2014 [19] value of α .

In this thesis the effect of quantum interference is considered for the five experimental techniques that have led to the most precise measurements of the he-

lium 2^3P fine structure. These measurements and their uncertainties are shown in Fig. 1.2, along with the values of the intervals predicted by QED theory. It can be seen that for each interval, while individual experimental values are measured to the kHz level or better, the consistency of the experimental measurements, and the consistency between the measurements and theory are to within a few kHz of each other. It is the aim of this work to calculate the interference shift present in each of the experimental determinations and apply appropriate corrections. These corrections bring the measured values into better agreement with theory and with each other.

Chapter 2 provides an outline of how quantum interference in precision spectroscopy is characterized, and introduces the theoretical formalism that will be used in the remaining chapters to model each type of experiment. In Chapter 3 an analysis follows of interference effects in the Shiner-group experiment using laser spectroscopy of 2^3S -to- 2^3P transitions in a narrow-angular-spread atomic beam [17, 35]. In Chapter 4 details are presented about quantum interference in the more complicated Inguscio-group experiment, based on saturated-fluorescence laser spectroscopy in a broad- angular-spread atomic beam [36]. In Chapter 5 the impact of interference in the Gabrielse-group measurement using saturated-absorption spectroscopy in a gas cell [15] is discussed. Finally, Chapter 6 deals with fine-structure measurements (Hessels group) which use microwave spectroscopy that directly drives transitions between the 2^3P_J states [13], including an experiment that

uses the Ramsey technique of separated oscillatory fields [16]. For each method, a separate calculation of the quantum-mechanical interference effect is necessary, with computationally-intense numerical solution of density-matrix equations describing the evolution of atomic population, as well as modeling of the specific experimental situation. A theoretical derivation of density-matrix equations from a master equation is covered in Appendix [A](#).

2 Quantum Interference in Precision Spectroscopy

2.1 Spectral Interference

In the context of precision spectroscopy, the natural line shape for an atomic transition that is probed near resonance can be distorted by quantum interference with off-resonant transitions to neighboring states. This small deviation results in a shift in the extracted line center that is potentially significant for the accuracy of the measurement.

The effect of a neighboring resonance on the ideal Lorentzian line shape form can be illustrated [37] with a simple model of two classical electric dipole moments \vec{q}_1 and \vec{q}_2 oscillating with respective resonant frequencies ω_1 and ω_2 . The observed spectrum due to an applied driving field of frequency ω is given by the square-modulus of the sum of two complex Lorentzian functions:

$$I(\omega) = \left| \frac{\vec{q}_1}{i(\omega - \omega_1) + \Gamma_1/2} + \frac{\vec{q}_2 e^{i\varphi}}{i(\omega - \omega_2) + \Gamma_2/2} \right|^2, \quad (2.1)$$

where Γ_1 and Γ_2 are the line widths of the individual resonances, and φ is a phase angle that allows \vec{q}_1 and \vec{q}_2 to be represented by real quantities. The resulting

intensity spectrum is a combination of the two individual Lorentzian functions for independent oscillators at ω_1 and ω_2 , plus a third cross-term that depends on the relative orientation of the dipoles, and their phase-difference φ . In the case of orthogonal dipoles (i.e., $\vec{q}_1 \cdot \vec{q}_2 = 0$) this interference term vanishes.

The impact of a distant resonance, and in particular the effect of interference, on the determination of a spectral line center may be seen by generating the spectrum with and without the cross-term in Eq. (2.1). A Lorentzian function fitted to one of the two spectral lines is used to extract the line center, while varying the separation of the resonant frequencies. Fig. 2.1 shows the deviations from the expected line center ω_1 of the first resonance as a function of the separation $\Delta\omega = \omega_2 - \omega_1$ of the two features. For simplicity, the line widths are set to be equal ($\Gamma_1 = \Gamma_2 = \Gamma$), and the dipole moments have equal magnitudes and zero relative phase ($|\vec{q}_1| = |\vec{q}_2|$, $\varphi = 0$).

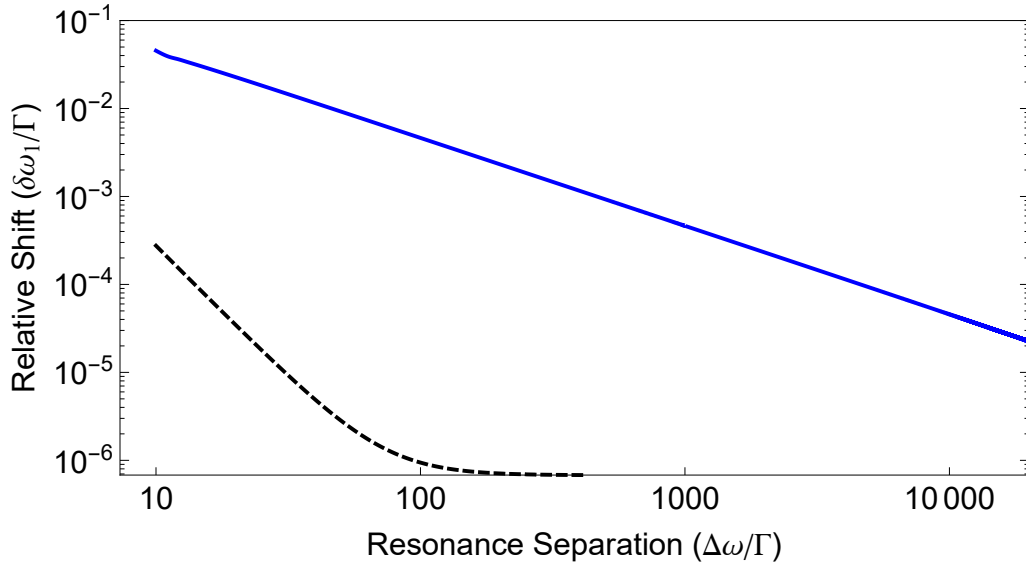


Figure 2.1: The relative shift $\delta\omega_1/\Gamma$ in the line center of one component of a double-line spectrum. The center frequency ω_1 is obtained by fitting a Lorentzian profile to the feature, while varying the relative separation $\Delta\omega/\Gamma = (\omega_2 - \omega_1)/\Gamma$ between the two resonances, where Γ is the line width of either resonance. The black dashed line shows the shift that would have resulted if the interference term in Eq. (2.1) is ignored, while the blue line is the shift that results when the complete model of Eq. (2.1) is used.

The black dashed line shows the expected shift in the line center when the spectrum is modeled as a simple sum of two Lorentzians (in other words, for the typical case where interference effects are ignored). The perturbation to the spectral feature of interest is seen to rapidly fall off as the resonances are separated, and one can therefore neglect the effect when the separation $\Delta\omega$ is large. However, when the spectrum is realistically calculated using Eq. (2.1), the resulting shift in the measured line center (the blue line in Fig. 2.1) is orders of magnitude larger, and is not negligible even when the separation of the resonances extends to thousands

of natural line widths.

2.2 The Four-level System

A representative system that models quantum interference is the four-level atom [34] shown in Fig. 2.2, with two ground states (denoted $|0\rangle$ and $|1\rangle$) and two excited states ($|2\rangle$ and $|3\rangle$). An applied field couples the ground state $|1\rangle$ to both of the upper levels, which can radiatively decay down to either of the two ground states. The second ground state ($|0\rangle$) is not coupled to either of the excited levels, and is therefore a dark state, so that any population that decays to $|0\rangle$ will remain there.

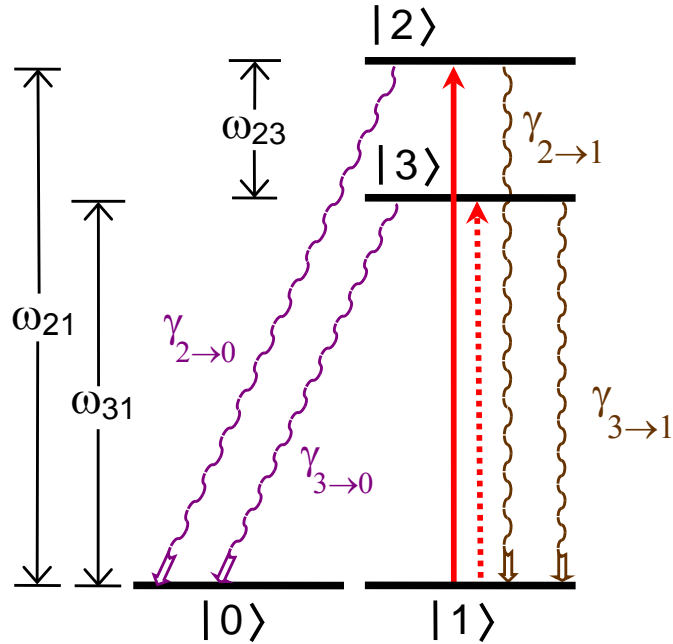


Figure 2.2: A four-level model atom, illustrating quantum interference between resonant (solid line) and non-resonant (dashed line) transitions. Radiative decay paths are shown with matching colors for interfering processes.

There are consequently two quantum-mechanical paths by which the atom can be excited and subsequently decay to a particular ground state, and these two processes can coherently interfere with one another. One pair of interfering pathways in Fig. 2.2 is the resonant excitation (solid arrow) from the ground state $|1\rangle$ to the excited state $|2\rangle$, with subsequent decay back to $|1\rangle$. This process interferes with the off-resonant excitation (dashed arrow) to state $|3\rangle$ and a similar decay to $|1\rangle$. The second pair of interfering pathways involves the same excitation processes as the first, but with decay to the dark $|0\rangle$ state instead. When the driving field is tuned close to one of the excited-state transitions, the amplitude for excitation to the off-resonance state is very small. However, the interference in the decay paths can affect the transfer of atomic population sufficiently to cause a distortion in the line shape and a resultant shift in the derived resonant frequency.

2.3 Density-matrix Equations

To study the effect of quantum interference on a measurement of a particular transition frequency in the four-level atom, it is necessary to model the evolution of population in the ground and excited states, incorporating the physics of Rabi oscillations, spontaneous decay, and optical pumping that results from prolonged interaction with the driving field. This can be achieved using a density-matrix formalism.

The interaction energy of the atom with an electric field (e.g., the field from a laser) that couples the ground state to the excited levels is given by $V(t) = e\vec{E}(t) \cdot \vec{r}$, in the electric-dipole approximation. For a monochromatic plane wave of frequency ω , peak intensity I_0 , and linear polarization \hat{z} , the electric field experienced by the atom is

$$\vec{E}(t) = \hat{z}E_0f(t)\cos(\omega t + \varphi), \quad (2.2)$$

where $E_0 = \sqrt{\frac{2I_0}{\epsilon_0 c}}$, φ is a phase, and $f(t)$ is a function that defines the time-varying amplitude of the field. I_0 is the maximum intensity of the field in W/m^2 (for which it is assumed that $f = 1$), ϵ_0 is the vacuum permittivity, and c is the speed of light.

If the transition frequencies ω_{21} and ω_{31} shown in Fig. 2.2 are much larger than the detuning of the applied field from either state $|2\rangle$ or state $|3\rangle$ (i.e., $\omega_{21}, \omega_{31} \gg \omega_{23}$), we can apply the rotating-wave approximation [38], in which the non-resonant $\exp[-i(\omega t + \varphi)]$ part of $\cos(\omega t + \varphi)$ is ignored. In this approximation, the density-matrix equations describing population transfer in the four-level system (see Ap-

pendix A) may be written as [34, 43]:

$$\begin{aligned} \dot{\rho}_{11} = & \frac{i\Omega_2^*}{2}\rho_{12} - \frac{i\Omega_2}{2}\rho_{21} + \frac{i\Omega_3^*}{2}\rho_{13} - \frac{i\Omega_3}{2}\rho_{31} \\ & + \gamma_{2\rightarrow 1}\rho_{22} + \gamma_{3\rightarrow 1}\rho_{33} + \gamma_{23\rightarrow 1}(\rho_{23} + \rho_{32}) \end{aligned} \quad (2.3a)$$

$$\dot{\rho}_{22} = \frac{i\Omega_2}{2}\rho_{21} - \frac{i\Omega_2^*}{2}\rho_{12} - \gamma_2\rho_{22} - \frac{\gamma_{23}}{2}(\rho_{23} + \rho_{32}) \quad (2.3b)$$

$$\dot{\rho}_{33} = \frac{i\Omega_3}{2}\rho_{31} - \frac{i\Omega_3^*}{2}\rho_{13} - \gamma_3\rho_{33} - \frac{\gamma_{23}}{2}(\rho_{23} + \rho_{32}) \quad (2.3c)$$

$$\dot{\rho}_{12} = \frac{i\Omega_2}{2}(\rho_{11} - \rho_{22}) - \frac{i\Omega_3}{2}\rho_{32} - \frac{\gamma_{23}}{2}\rho_{13} - \left(\frac{\gamma_2}{2} + i\Delta_2\right)\rho_{12} \quad (2.3d)$$

$$\dot{\rho}_{13} = \frac{i\Omega_3}{2}(\rho_{11} - \rho_{33}) - \frac{i\Omega_2}{2}\rho_{23} - \frac{\gamma_{23}}{2}\rho_{12} - \left(\frac{\gamma_3}{2} + i\Delta_3\right)\rho_{13} \quad (2.3e)$$

$$\dot{\rho}_{23} = \frac{i\Omega_3}{2}\rho_{21} - \frac{i\Omega_2^*}{2}\rho_{13} - \frac{\gamma_{23}}{2}(\rho_{22} + \rho_{33}) - \left(\frac{\gamma_2}{2} + \frac{\gamma_3}{2} + i\omega_{23}\right)\rho_{23}. \quad (2.3f)$$

The diagonal density-matrix elements ρ_{11} , ρ_{22} , and ρ_{33} in Eqs. (2.3) represent the populations in the ground and excited states, while the off-diagonal elements $\rho_{12} = \rho_{21}^*$, $\rho_{13} = \rho_{31}^*$, and $\rho_{23} = \rho_{32}^*$ represent correlations between states. If the system starts in the $|1\rangle$ state, the initial value of ρ_{11} is 1, with all other entries set to zero. The equations for $\dot{\rho}_{01}$, $\dot{\rho}_{02}$, and $\dot{\rho}_{03}$ are not required, as none of these quantities appear in the right-hand side of Eqs. (2.3), and the population in the dark state $|0\rangle$ (i.e., ρ_{00}) can be found from the condition $\rho_{00} + \rho_{11} + \rho_{22} + \rho_{33} = 1$.

In Eqs. (2.3), $\Delta_2 = \omega - \omega_{21}$ and $\Delta_3 = \omega - \omega_{31}$ are the detuning of the laser frequency ω from the $|1\rangle \rightarrow |2\rangle$ and $|1\rangle \rightarrow |3\rangle$ transitions, respectively, where ω_{21} and ω_{31} are the frequencies shown in Fig. 2.2. The quantities $\Omega_2(t)$ and $\Omega_3(t)$ in the above equations are the time-dependent Rabi frequencies associated with the

driven transitions between the ground state $|1\rangle$ and the two excited states $|2\rangle$ and $|3\rangle$, and are given by:

$$\Omega_2(t) = eE_0f(t)e^{i\varphi}\langle 1|z|2\rangle/\hbar, \quad (2.4)$$

$$\Omega_3(t) = eE_0f(t)e^{i\varphi}\langle 1|z|3\rangle/\hbar. \quad (2.5)$$

The spontaneous-decay terms in Eqs. (2.3) involve the quantities

$$\gamma_{i\rightarrow j} = \frac{e^2|\omega_{ij}|^3}{3\pi\epsilon_0\hbar c^3}\langle j|\vec{r}|i\rangle \cdot \langle i|\vec{r}|j\rangle \approx \frac{e^2\bar{\omega}^3}{3\pi\epsilon_0\hbar c^3}\langle j|\vec{r}|i\rangle \cdot \langle i|\vec{r}|j\rangle, \quad (2.6a)$$

$$\gamma_{23\rightarrow j} = \frac{e^2|\omega_{2j}|^3}{3\pi\epsilon_0\hbar c^3}\langle j|\vec{r}|2\rangle \cdot \langle 3|\vec{r}|j\rangle \approx \frac{e^2\bar{\omega}^3}{3\pi\epsilon_0\hbar c^3}\langle j|\vec{r}|2\rangle \cdot \langle 3|\vec{r}|j\rangle. \quad (2.6b)$$

The values $\gamma_{2\rightarrow 0}$, $\gamma_{2\rightarrow 1}$, $\gamma_{3\rightarrow 0}$, and $\gamma_{3\rightarrow 1}$ are the partial rates for radiative decay from $|2\rangle$ and $|3\rangle$ to $|0\rangle$ and $|1\rangle$ (as shown in Fig. 2.2), with total decay rates $\gamma_2 = \gamma_{2\rightarrow 0} + \gamma_{2\rightarrow 1}$ and $\gamma_3 = \gamma_{3\rightarrow 0} + \gamma_{3\rightarrow 1}$. These last two rates have the same value $\gamma = 1/\tau$ because the $|1\rangle$ -to- $|2\rangle$ and $|1\rangle$ -to- $|3\rangle$ frequency intervals ω_{21} and ω_{31} can be approximated by the average value $\bar{\omega}$ in Eqs. (2.6) (since $\omega_{21}, \omega_{31} \gg \omega_{23}$). The off-diagonal terms $\gamma_{23\rightarrow 0}$ and $\gamma_{23\rightarrow 1}$ (with $\gamma_{23} = \gamma_{23\rightarrow 0} + \gamma_{23\rightarrow 1}$) represent interference between the partial decay rates, and contribute to shifts in the resonance line shapes. These terms are particularly important for experimental signals that depend strongly on decay processes, such as fluorescence measurements or final-state population counts. Calculations using density matrix equations often neglect these cross-damping terms and therefore do not include these decay-path interference effects [31, 39].

2.4 Reduced Equations

The set of Eqs. (2.3) can be integrated over the time T that the atom interacts with the applied field, to determine the final population in each state. However, this integration may be numerically challenging due to the fast oscillations caused by the large ω_{23} term, and may require very small time steps to accurately solve the equations.

If the applied field is very closely tuned to the $|1\rangle \rightarrow |2\rangle$ transition of Fig. 2.2, very little population is excited to the far-off-resonance $|3\rangle$ state. The quantities $\gamma_{i \rightarrow j}$ and $|\gamma_{23 \rightarrow j}|$ are $\lesssim \gamma$, the natural line width of the resonance, and, to avoid broadening of the line shape, $|\Omega_{2,3}|$ and $2\pi/T$ must in practice be $\lesssim \gamma$ as well. Finally, the field-detuning $|\Delta_2|$ also takes on values $\lesssim \gamma$ (i.e., of the same order as the line width) as it scans across the $|1\rangle \rightarrow |2\rangle$ resonance. Assuming all of these frequencies ($\gamma_{i \rightarrow j}$, $|\gamma_{23 \rightarrow j}|$, $|\Omega_{2,3}|$, $2\pi/T$, and $|\Delta_2|$) are much smaller than ω_{23} , the separation between the measured and distant resonances, one can define [34] an ordering-parameter η , which is the ratio of these two frequency scales.

Having introduced η as the ratio of a very small to a much-larger frequency, the tiny amount of population transferred to the off-resonant $|3\rangle$ state is of second order in η , and can thus be ignored ($\rho_{33} \lesssim \eta^2$). Furthermore, by taking linear combinations of Eqs. (2.3) and discarding terms of $\mathcal{O}(\eta^2)$, one can also eliminate the ρ_{13} , ρ_{31} , ρ_{23} , and ρ_{32} elements, which are an order of η smaller than the dominant

quantities $\rho_{11}, \rho_{22}, \rho_{12}$ and ρ_{21} , .

The reduction process is illustrated by considering the equation for $\dot{\rho}_{11}$ (Eq. (2.3)(a)).

Elimination of explicit dependence on the elements $\rho_{13}, \rho_{31}, \rho_{23}$, and ρ_{32} , can be achieved by forming the following linear combination of Eqs. (2.3)(a), (e), and (f):

$$(a) + \left(\left[\frac{i}{2} \cdot \frac{\Omega_3^*}{\frac{\gamma_3}{2} + i\Delta_3} \right] (e) + c.c. \right) + \left(\left[\frac{\gamma_{23 \rightarrow 1}}{\frac{\gamma_2}{2} + \frac{\gamma_3}{2} + i\omega_{23}} \right] (f) + c.c. \right). \quad (2.7)$$

This operation yields a new equation for the modified quantity $\tilde{\rho}_{11} = \rho_{11} + \frac{i}{2} \frac{\Omega_3^*}{\frac{\gamma_3}{2} + i\Delta_3} \rho_{13} -$

$\frac{i}{2} \frac{\Omega_3}{\frac{\gamma_3}{2} - i\Delta_3} \rho_{31}$, with the left-hand side given by

$$\begin{aligned} \dot{\tilde{\rho}}_{11} &= \dot{\rho}_{11} + \frac{i}{2} \frac{\Omega_3^*}{\frac{\gamma_3}{2} + i\Delta_3} \dot{\rho}_{13} - \frac{i}{2} \frac{\Omega_3}{\frac{\gamma_3}{2} - i\Delta_3} \dot{\rho}_{31} \\ &= \frac{d}{dt} \left[\rho_{11} + \frac{i}{2} \frac{\Omega_3^*}{\frac{\gamma_3}{2} + i\Delta_3} \rho_{13} - \frac{i}{2} \frac{\Omega_3}{\frac{\gamma_3}{2} - i\Delta_3} \rho_{31} \right] \\ &\simeq \dot{\rho}_{11}, \end{aligned} \quad (2.8)$$

where in the final step, the terms involving the first-order elements ρ_{13} and ρ_{31} have been neglected, as multiplication by coefficients of $\mathcal{O}(\eta)$ makes these terms $\mathcal{O}(\eta^2)$ overall.

The right-hand side of the equation becomes:

$$\begin{aligned}
RHS = & \left[-\frac{|\Omega_3|^2}{4} \left(\frac{1}{\frac{\gamma_3}{2} + i\Delta_3} + \frac{1}{\frac{\gamma_3}{2} - i\Delta_3} \right) \right] \rho_{11} \\
& + \left[\frac{i}{2}\Omega_2^* - \frac{i}{2}\Omega_3^* \left(\frac{1}{2} \frac{\gamma_{23}}{\frac{\gamma_3}{2} + i\Delta_3} + \frac{\gamma_{23 \rightarrow 1}}{\frac{\gamma_2}{2} + \frac{\gamma_3}{2} - i\omega_{23}} \right) \right] \rho_{12} + c.c. \\
& + \left[\gamma_{2 \rightarrow 1} - \frac{\gamma_{23}}{2} \gamma_{23 \rightarrow 1} \left(\frac{1}{\frac{\gamma_2}{2} + \frac{\gamma_3}{2} + i\omega_{23}} + \frac{1}{\frac{\gamma_2}{2} + \frac{\gamma_3}{2} - i\omega_{23}} \right) \right] \rho_{22} \\
& - \left[\frac{i}{2} \frac{\Omega_2^* \gamma_{23 \rightarrow 1}}{\frac{\gamma_2}{2} + \frac{\gamma_3}{2} + i\omega_{23}} \right] \rho_{13} + c.c. \\
& + \left[\frac{1}{4} \frac{\Omega_2 \Omega_3^*}{\frac{\gamma_3}{2} + i\Delta_3} \right] \rho_{23} + c.c. \tag{2.9}
\end{aligned}$$

The coefficient of ρ_{11} and the second term of the ρ_{22} coefficient have the form $\frac{1}{a+ib} + \frac{1}{a-ib} = \frac{2a}{a^2+b^2}$, and therefore they are of $\mathcal{O}(\eta^2)$ since $\omega_{23}^2, \Delta_3^2 = (\Delta_2 + \omega_{23})^2 \gg \gamma_2^2, \gamma_3^2$. The first-order elements ρ_{13} and ρ_{23} are multiplied by $\mathcal{O}(\eta)$ coefficients, making these terms $\mathcal{O}(\eta^2)$ as well.

The surviving terms are $\gamma_{2 \rightarrow 1} \rho_{22}$ (which is of order η^0) and the ρ_{12} term, which is complete to $\mathcal{O}(\eta)$. The latter term may be simplified using the approximations $\frac{\gamma_3}{2} + i(\Delta_2 + \omega_{23}) \approx i\omega_{23}$ and $\frac{\gamma_2}{2} + \frac{\gamma_3}{2} - i\omega_{23} \approx -i\omega_{23}$. This leads to an expression for the right-hand side which is correct up to order η :

$$\begin{aligned}
RHS \approx & \left[\frac{i}{2}\Omega_2^* - \frac{i}{2}\Omega_3^* \left(\frac{1}{2} \frac{\gamma_{23}}{\frac{\gamma_3}{2} + i\Delta_3} + \frac{\gamma_{23 \rightarrow 1}}{\frac{\gamma_2}{2} + \frac{\gamma_3}{2} - i\omega_{23}} \right) \right] \rho_{12} + c.c. \\
= & \left[\frac{i}{2}\Omega_2^* - \frac{i}{2}\Omega_3^* \left(\frac{1}{2} \frac{\gamma_{23}}{i\omega_{23}} + \frac{\gamma_{23 \rightarrow 1}}{-i\omega_{23}} \right) \right] \rho_{12} + c.c. \\
= & \left[\frac{i}{2}\Omega_2^* - \frac{i}{2}\Omega_3^* \left(\frac{\gamma_{23} - 2\gamma_{23 \rightarrow 1}}{2\omega_{23}} \right) \right] \rho_{12} + c.c. \tag{2.10}
\end{aligned}$$

A similar procedure may be carried out on the equations for the dominant

density-matrix elements $\dot{\rho}_{12}, \dot{\rho}_{21}$ and $\dot{\rho}_{22}$, forming linear combinations using the equations for the first-order elements $\rho_{13}, \rho_{31}, \rho_{23}, \rho_{32}$ to cancel the latter quantities out, and discarding terms of $\mathcal{O}(\eta^2)$.

The resulting reduced equations, which are complete to $\mathcal{O}(\eta)$, are:

$$\begin{aligned} \dot{\rho}_{11} = & \frac{i}{2} \left(\Omega_2^* + i \frac{\gamma_{23} - 2\gamma_{23 \rightarrow 1}}{2\omega_{23}} \Omega_3^* \right) \rho_{12} - \frac{i}{2} \left(\Omega_2 - i \frac{\gamma_{23} - 2\gamma_{23 \rightarrow 1}}{2\omega_{23}} \Omega_3 \right) \rho_{21} \\ & + \gamma_{2 \rightarrow 1} \rho_{22} \end{aligned} \quad (2.11a)$$

$$\dot{\rho}_{22} = \frac{i}{2} \left(\Omega_2 + i \frac{\gamma_{23}}{2\omega_{23}} \Omega_3 \right) \rho_{21} - \frac{i}{2} \left(\Omega_2^* - i \frac{\gamma_{23}}{2\omega_{23}} \Omega_3^* \right) \rho_{12} - \gamma_2 \rho_{22} \quad (2.11b)$$

$$\begin{aligned} \dot{\rho}_{12} = & \frac{i}{2} \left(\Omega_2 + i \frac{\gamma_{23}}{2\omega_{23}} \Omega_3 \right) \rho_{11} - \frac{i}{2} \left(\Omega_2 - i \frac{\gamma_{23}}{2\omega_{23}} \Omega_3 \right) \rho_{22} \\ & - \left(\frac{\gamma_2}{2} + i \left[\Delta_2 + \frac{\gamma_{23}^2 + |\Omega_3|^2}{4\omega_{23}} \right] \right) \rho_{12}. \end{aligned} \quad (2.11c)$$

Equations (2.11)(a)-(c) involve the dominant ρ_{11} , ρ_{12} , ρ_{21} , and ρ_{22} components of the density matrix, and include order- η perturbations due to the distant off-resonance state $|3\rangle$. The $\frac{|\Omega_3|^2}{4\omega_{23}}$ term is the usual AC-Stark shift of the $|1\rangle$ state, which extrapolates to zero with decreasing laser intensity. The terms of form $\frac{\Omega_3 \gamma_{23 \rightarrow 1}}{2\omega_{23}}$ represent interference in the decay pathways. The presence of these types of terms leads to a shift in the resonance line center, which does not vanish in the limit of zero laser intensity.

The reduced expressions in Eqs. (2.11) lack the fast oscillations found in Eqs. (2.3), and thus require a factor of η fewer time steps for the numerical integration, while

the results of these integrations agree with those from Eqs. (2.3) to order η^2 .

2.5 Application to Helium Spectroscopy

The preceding discussion of quantum interference is relevant to measurements of helium fine-structure using laser spectroscopy. In this section it is shown that the assumptions associated with the rotating-wave approximation and the derivation of the reduced equations (Eq. (2.11)) are valid for such laser measurements.

For laser spectroscopy from the 2^3S_1 state (see Fig. 2.3), an atomic sample is typically prepared in one of the metastable states, and a 1083-nm laser drives transitions to the 2^3P_J excited states. Fine-structure spacings may be determined by taking the difference between any two such transition frequencies. While the laser frequency is tuned close to resonance with one of the 2^3P_J states, off-resonant transitions to different states $2^3P_{J \neq J}$ can also occur. As the atoms decay back to the metastable states, quantum interference between two or more radiative-decay pathways distorts the observed line shape for the transition of interest. In principle, the laser field can drive transitions to an infinite number of higher-energy bound states ($n > 2$) in the helium atom, but these transitions are orders of magnitude farther away from the main resonance than the nearest neighboring 2^3P state, so that their effect is negligible.

The particular role that interference plays depends on the detection signal used

to obtain the line shape. For example, an experimental signal may be based on level populations, either counting the atoms in an initially-empty metastable state after it is repopulated by optical pumping from the initial state, or by measuring the depletion of the initially-populated state. Some measurements are based on detection of the fluorescence emitted from spontaneous decay, while others detect the absorption of the incident light as the laser frequency is tuned across a resonance. Each of these detection techniques may involve different excitation and decay pathways, and hence different interfering processes.

As an example, Figure 2.3 shows the schematic for a measurement of the 2^3S_1 -to- 2^3P_1 resonance, which may be mapped directly to the four-level model atom. The population is initially in the $2^3S_1(m_J=1)$ metastable state, which corresponds to $|1\rangle$ in the four-level model, and is excited (solid arrow) to the $2^3P_1(m_J=1)$ state (analogous to $|2\rangle$) by a linearly-polarized laser tuned to near that transition. A small amount of population is also transferred (dotted arrow) to the far-off-resonance $2^3P_2(m_J=1)$ state ($|3\rangle$).

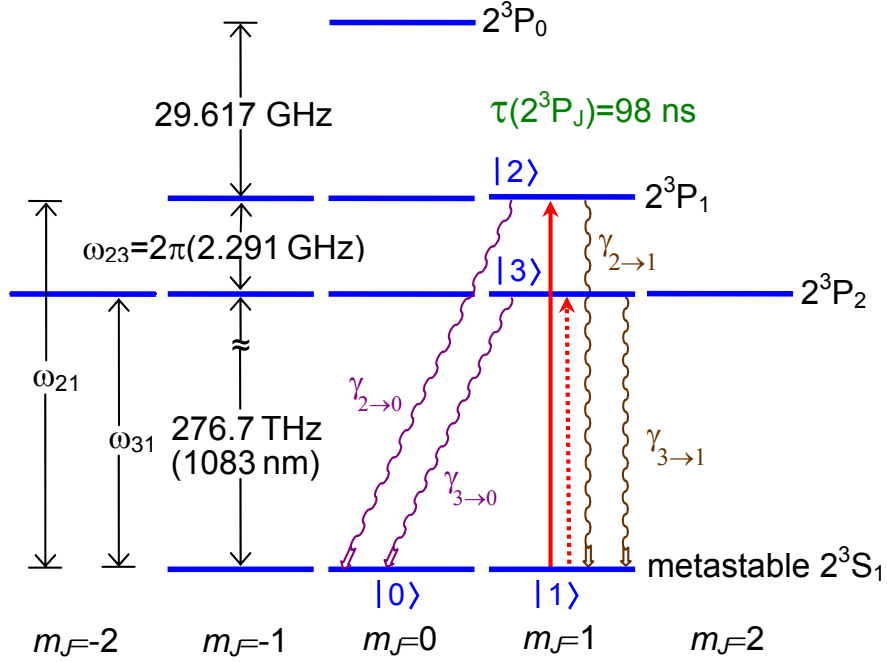


Figure 2.3: The $n=2$ triplet energy levels of helium, depicting the measurement of the $2^3S_1(m_J=1)$ -to- $2^3P_1(m_J=1)$ resonance. Only the four numbered states are involved in the measurement. The radiative decay paths are shown, with matching colors for interfering processes.

The atoms can decay back to $|1\rangle$, or to the $2^3S_1(m_J=0)$ state ($|0\rangle$), which plays the role of the dark state due to the electric-dipole-forbidden $2^3S_1(m_J=0)$ -to- $2^3P_1(m_J=0)$ transition. Thus only the four numbered states play a significant role in the measurement. The radiative decay paths are shown, each one having an allowed electric-dipole 2^3S -to- 2^3P transition.

Depending on how the measurement signal is obtained, different interference processes come into play. For instance, the count of atoms transferred to the dark state $|0\rangle$ is affected by the two interfering pathways: $|1\rangle \rightarrow |2\rangle \rightarrow |0\rangle$ and $|1\rangle \rightarrow$

$|3\rangle \rightarrow |0\rangle$. These two pathways are also relevant if the emitted circularly-polarized fluorescence is measured to form the line shape. On the other hand, if only linearly-polarized fluorescence is detected, then the interference between the $|1\rangle \rightarrow |2\rangle \rightarrow |1\rangle$ and $|1\rangle \rightarrow |3\rangle \rightarrow |1\rangle$ processes is important.

The applicability of Eqs. (2.3), which use the rotating-wave approximation, to these laser measurements is certainly justified, as the optical transition frequencies from the metastable to the 2^3P states (i.e., ω_{21} and ω_{31} in Fig. 2.3) are much larger than the detuning of the laser from the transition to any of the 2^3P states (≈ 277 THz vs. $\lesssim 30$ GHz). Furthermore, the reduced Eqs. (2.11) are valid as well, since the separation between the measured and the off-resonant transition ($\omega_{23} = 2\pi(2291 \text{ MHz})$ in the figure) is much larger than the natural line width $\gamma = 2\pi(1.63 \text{ MHz})$. The ordering-parameter η , which is the ratio of these two frequency scales, is therefore of magnitude $\frac{1.63}{2291} \simeq 10^{-3}$. The use of Eqs. (2.11) thus requires three orders of magnitude fewer time steps for numerical integration than Eqs. (2.3), and the results of integrating Eqs. (2.11) and Eqs. (2.3) agree to approximately a part-per-million ($\sim \eta^2$).

3 Laser Spectroscopy in a Narrow Thermal Beam

In a first analysis of interference effects, we calculate interference shifts that apply for an existing precision laser measurement of the 2^3P_1 — 2^3P_2 fine-structure interval [35], performed using a well-collimated beam of thermal He atoms. Both the 2^3S_1 -to- 2^3P_1 and 2^3S_1 -to- 2^3P_2 transitions are measured in this experiment, and the interval is found from the difference of the two resonant frequencies. The resultant interference shift (calculated in this chapter) is -1.2 kHz, which is larger than the 1.0-kHz measurement uncertainty in Ref. [35], even though the separation between the two resonances is more than 1400 times the natural line width of 1.63 MHz.

3.1 Measurement Technique

The experiment in [35] is performed by preparing a thermal beam of metastable He atoms via electron bombardment. An inhomogeneous magnetic field is used to deflect $2^3S_1(m=\pm 1)$ atoms out of the beam and thus select the population in the $2^3S_1(m=0)$ state. These atoms then pass through a uniform magnetic field, where a circularly-polarized 1083-nm Gaussian laser beam (perpendicular to the atomic

beam) drives transitions to the $2^3P_{1,2}(m=+1)$ states (see red arrows in Fig. 3.1). After the atoms pass through the laser beam and spontaneous emission has repopulated the $2^3S_1(m=+1)$ state, a second inhomogeneous magnetic field selects these $m=+1$ atoms by deflecting them to a detector, where they are counted to obtain the measurement signal. The sub-milliradian collimation of the atomic beam minimizes Doppler broadening effects, while the laser intensity is kept sufficiently low to avoid power broadening of the resonance. This technique allows the measured line width to approach the natural line width.

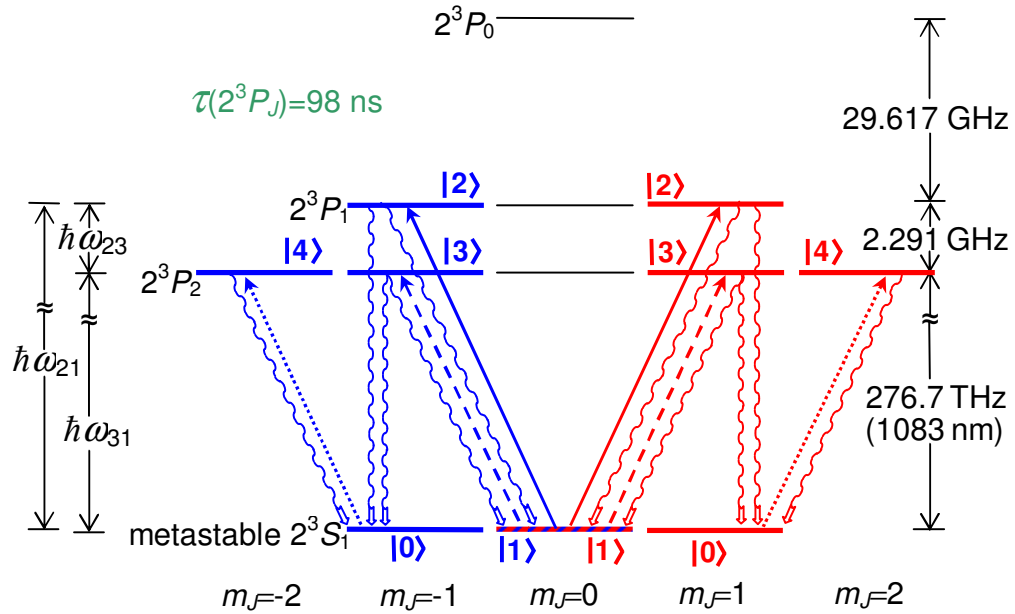


Figure 3.1: The $n=2$ He triplet energy levels. Population starts in $|1\rangle$ and interacts with a circularly-polarized laser field, either σ_+ (red), or σ_- (blue), which drives both $|1\rangle \rightarrow |2\rangle$ (solid arrow) and $|1\rangle \rightarrow |3\rangle$ (dashed arrow) transitions. The cycling transition (dotted arrow) and the allowed radiative decay paths are also shown.

The atomic transitions involved in the measurement are shown in Fig. 3.1. The

population is initially in the $2^3S_1(m=0)$ state (labeled $|1\rangle$), and a 1083-nm laser with σ_+ polarization (red) drives transitions to both the $2^3P_1(m=+1)$ state (labeled $|2\rangle$) and the $2^3P_2(m=+1)$ state (labeled $|3\rangle$). These transitions are shown as solid and dashed arrows, respectively. Excited atoms can then radiatively decay back to $|1\rangle$, or repopulate the $2^3S_1(m=+1)$ level (denoted $|0\rangle$ in the figure).

Atoms in the $|0\rangle$ state can be excited to the $2^3P_2(m=+2)$ state (labeled $|4\rangle$), but this state can only decay back to $|0\rangle$, and thus population in the $|0\rangle$ state cycles back and forth between these two levels. After having passed through the laser beam, and after sufficient time has elapsed to allow for radiative decay, all of these cycling atoms will ultimately occupy the $2^3S_1(m=+1)$ ($|0\rangle$) state.

When a σ_+ laser is tuned to near the $2^3S_1(m=0)$ -to- $2^3P_1(m=+1)$ transition, atoms are pumped to the $2^3S_1(m=+1)$ state by excitation and subsequent radiative decay. The amplitude for this resonant process interferes with the much smaller amplitude for the off-resonant pathway, from $2^3S_1(m=0)$ to $2^3P_2(m=+1)$ and then down to $2^3S_1(m=+1)$, leading to a shift in the line shape. Alternately, when measuring the $2^3S_1(m=0)$ -to- $2^3P_2(m=+1)$ resonance, this dominant pathway interferes with the now-small amplitude for driving population from $2^3S_1(m=0)$ to $2^3P_1(m=+1)$ and then decaying to $2^3S_1(m=+1)$, resulting in an effect of equal magnitude but opposite sign.

The preceding description is equally valid if the incident laser has the opposite (σ_-) polarization. This case is depicted in Fig. 3.1 using blue color-coding. De-

pending on the tuning of the laser frequency, atoms in the same initial $2^3S_1(m=0)$ state are driven to either the $2^3P_1(m=-1)$ state ($|1\rangle \rightarrow |2\rangle$, solid arrow) or to the $2^3P_2(m=-1)$ state ($|1\rangle \rightarrow |3\rangle$, dashed arrow), and accumulate in the $2^3S_1(m=-1)$ ($|0\rangle$) state via spontaneous decay. The $|0\rangle \leftrightarrow |4\rangle$ cycling transition is now between the $2^3S_1(m=-1)$ and $2^3S_2(m=-2)$ states. Once again, quantum-mechanical interference between the resonant and off-resonant optical pumping pathways leads to an identical shift in the resonance line shape.

3.2 Theoretical Description

The atomic states involved in the measurement can be directly mapped to the four-level model of Eqs. (2.11), with both states in the $|0\rangle \leftrightarrow |4\rangle$ cycling transition decoupled from the other states when probing the 2^3S_1 -to- 2^3P_2 resonance.

The partial decay rates of Eqs. (2.11) are obtained from the electric-dipole matrix-elements (see Appendix B) as: $\gamma_{2\rightarrow 1} = \gamma_{3\rightarrow 1} = \gamma_{2\rightarrow 0} = \gamma_{3\rightarrow 0} = \gamma/2$, $\gamma_{23\rightarrow 1} = \pm\gamma/2$, and $\gamma_{23\rightarrow 0} = \mp\gamma/2$ (for σ_{\pm} polarization respectively). The total rates are therefore $\gamma_2 = \gamma_3 = \gamma$, and $\gamma_{23} = 0$. Here $\gamma = 1/\tau$, where $\tau = 97.9$ ns is the lifetime of the 2^3P states.

In the electric-dipole approximation, the electric field of the circularly-polarized (σ_{\pm}) 1083-nm laser experienced by the atom is

$$\vec{E}(t) = E_0 G(t) \frac{1}{\sqrt{2}} [\hat{x} \cos(\omega t + \phi) \pm \hat{y} \sin(\omega t + \phi)], \quad (3.1)$$

where $E_0 = \sqrt{\frac{2I_0}{\epsilon_0 c}}$, and $G(t) = \exp[-2(t - t_L)^2/T_L^2]$ models the profile of the electric field seen by the atom as it passes through the Gaussian beam with peak intensity I_0 , as shown in Fig. 3.2.

This field expression gives time-dependent Rabi frequencies, in the rotating-wave approximation, of:

$$\Omega_2(t) = \frac{1}{\sqrt{2}} e E_0 G(t) \langle 1 | x \mp iy | 2 \rangle / \hbar, \quad (3.2)$$

$$\Omega_3(t) = \frac{1}{\sqrt{2}} e E_0 G(t) \langle 1 | x \mp iy | 3 \rangle / \hbar. \quad (3.3)$$

From the ratio of the matrix elements one finds that Ω_2 and Ω_3 are related by $\Omega_2 = \pm \Omega_3$ (for σ_{\pm} polarization). Substituting these values into Eqs. (2.11), the resulting reduced density-matrix equations for this four-level system are:

$$\dot{\rho}_{11} = \left(\frac{i\Omega_2^*(t)}{2} + \frac{\gamma\Omega_2^*(t)}{4\omega_{23}} \right) \rho_{12} - \left(\frac{i\Omega_2(t)}{2} - \frac{\gamma\Omega_2(t)}{4\omega_{23}} \right) \rho_{21} + \frac{\gamma}{2} \rho_{22}, \quad (3.4a)$$

$$\dot{\rho}_{12} = \frac{i\Omega_2(t)}{2} \rho_{11} - \left(\frac{\gamma}{2} + i\Delta_2'(t) \right) \rho_{12} - \frac{i\Omega_2(t)}{2} \rho_{22}, \quad (3.4b)$$

$$\dot{\rho}_{22} = \frac{i\Omega_2(t)}{2} \rho_{21} - \frac{i\Omega_2^*(t)}{2} \rho_{12} - \gamma \rho_{22}. \quad (3.4c)$$

Here,

$$\Delta_2'(t) = \Delta_2 + \frac{|\Omega_3(t)|^2}{4\omega_{23}}, \quad (3.5)$$

where $\Delta_2 = \omega - \omega_{21}$ is the amount by which the laser is detuned from the $|1\rangle \rightarrow |2\rangle$ transition. Note that Eq. (3.4) is valid for both σ_+ and σ_- polarizations, since the sign differences from $\Omega_3 = \pm \Omega_2$ and from $\gamma_{23 \rightarrow 1} = \pm \gamma/2$ cancel out.

The difference between Δ'_2 and Δ_2 represents a shift in the resonance which is just the usual AC-Stark shift for the interval. Its magnitude is relatively small for the laser intensities considered here, and approaches zero with decreasing laser intensity. In contrast, the nonzero value of $\gamma_{23 \rightarrow 1}$ results in the ω_{23}^{-1} interference terms, which lead to a larger shift in the resonance line center, that, unlike the AC-Stark shift, does not extrapolate to zero as the laser intensity goes to zero.

The details of the timing profile used to model an atom's transit through the laser beam can be seen in Fig. 3.2. The atom starts in $|1\rangle$ at a time t_i before it enters the beam, and then experiences a Gaussian intensity profile, with $1/e$ width T_L , and peak intensity I_0 at time t_L . The width is determined by the speed of the atom, and the maximum intensity is a function of the laser power, beam waist, and the atom's trajectory through the laser beam. The atoms that end up in $|0\rangle$ are detected at a later time t_f , after the atom has traversed the laser beam and sufficient time has passed for the 2^3P excited-state atoms to radiatively decay back to the 2^3S metastable states.

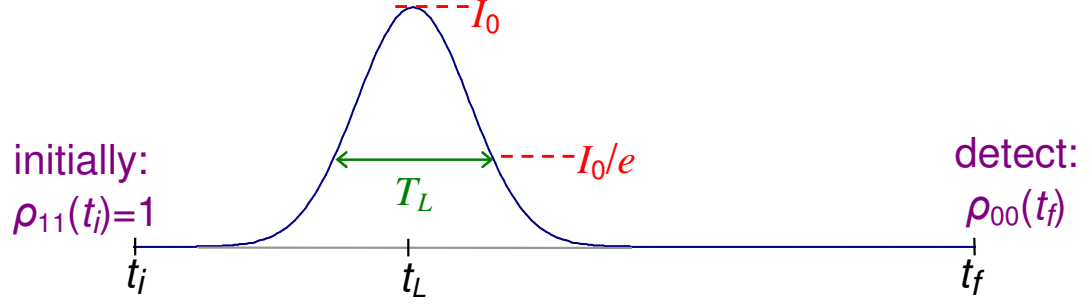


Figure 3.2: Intensity profile for an atom traveling through a Gaussian laser beam with peak intensity I_0 . The atom starts in $|1\rangle$ of Fig. 3.1, and the final population of $|0\rangle$ is determined after it has left the laser beam, and the 2^3P atoms have decayed back to the 2^3S states.

For a given choice of laser intensity I_0 , frequency ω , and timing parameters T_L , t_L and t_f , Eq. (3.4) can be numerically solved to obtain the final population in states $|1\rangle$ and $|2\rangle$ ($\rho_{11}(t_f)$ and $\rho_{22}(t_f)$ respectively). Since all of the population has radiatively decayed to either $|0\rangle$ or $|1\rangle$ by time t_f , the detection signal is given by $\rho_{00}(t_f) = 1 - \rho_{11}(t_f)$.

Numerical integration, using an adaptive-step solver, is performed for a set of laser frequencies near the resonance, leading to a calculated line shape for the $2^3S_1-2^3P_1$ transition, an example of which is shown in Fig. 3.3(a). Fig. 3.3(c) shows the difference between this line shape and the one obtained by setting the interference term $\gamma_{23\rightarrow 1}=0$. This difference, caused by the quantum-mechanical interference with the distant $|1\rangle\rightarrow|3\rangle$ transition, is not symmetric about the line center, and hence results in a shift in the observed resonance.

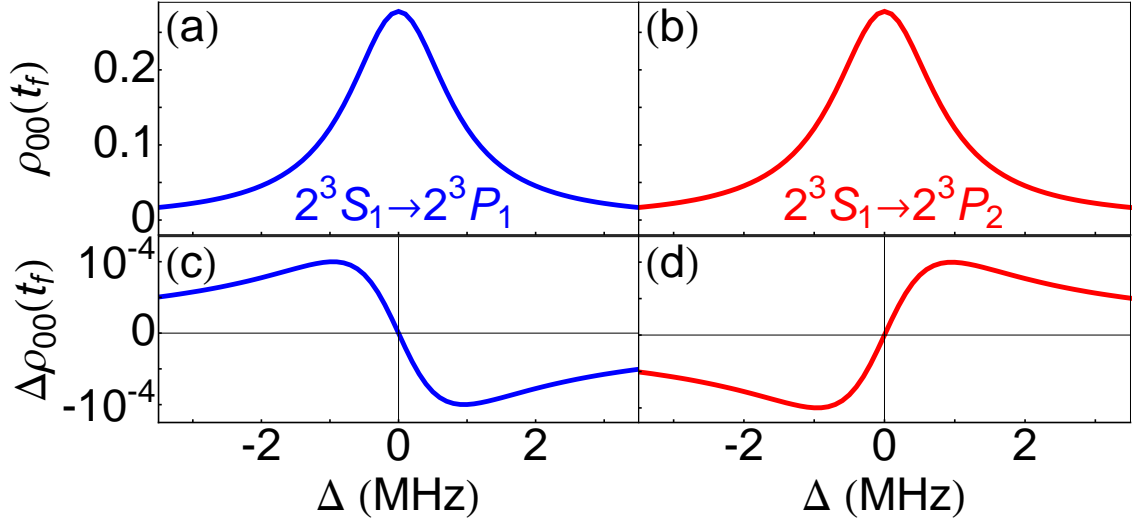


Figure 3.3: Lineshapes of the $|1\rangle \rightarrow |2\rangle$ (a) and $|1\rangle \rightarrow |3\rangle$ (b) resonances of Fig. 3.1, obtained from numerical integration of Eq. (3.4) for the laser beam of Fig. 3.2 with $T_L=4 \mu\text{s}$ and $I_0=10 \mu\text{W}/\text{cm}^2$. The differences, (c) and (d), are shown between these line shapes and those obtained by setting the interference term $\gamma_{23 \rightarrow 1}=0$.

The derivation of Eqs. (2.11) assumed a laser close to the resonant frequency of the $|1\rangle \rightarrow |2\rangle$ transition, but a similar derivation can be performed when the frequency ω is nearly in resonance with the $|1\rangle \rightarrow |3\rangle$ transition instead, leading to a set of equations analogous to Eq. (3.4), but with $|2\rangle$ and $|3\rangle$ interchanged. Since $\omega_{32}=-\omega_{23}$ and $|\Omega_2|^2 = |\Omega_3|^2$, the interference shifts for the $|1\rangle \rightarrow |2\rangle$ and $|1\rangle \rightarrow |3\rangle$ resonances are equal in magnitude and opposite in sign, as can be seen in Fig. 3.3(d).

The effect on the deduced $2^3P_1-2^3P_2$ interval is thus twice the absolute shift for either of the laser transitions. In this case, the 2^3S_1 -to- 2^3P_1 transition is negatively shifted to a lower frequency, while the 2^3S_1 -to- 2^3P_2 resonance has a positive shift to

a higher frequency, resulting in a smaller observed fine-structure interval. A positive correction for interference effects must therefore be applied to the measured interval.

Accordingly, only the line shape of the 2^3S_1 -to- 2^3P_1 transition needs to be computed, and the shift in the line center can be doubled to obtain the total shift for the 2^3P_1 — 2^3P_2 interval. Repeating the procedure with the interference term $\gamma_{23\rightarrow 1}$ set to zero lets one subtract out the AC Stark shift. This is of interest because the usual experimental analysis accounts for the AC Stark shift by extrapolating to zero laser power, but ignores the interference shift.

Determining the position of the line center is in theory as simple as finding the maximum of the computed resonance profile, where the first-derivative is zero. In practice, however, it is difficult to calculate values with sufficient precision to model this part of the line shape accurately. Fitting the profile to a Lorentzian or other function to extract the center is also possible, but distortions in the line shape due to quantum interference may pose a challenge to obtaining a stable and accurate fit. Instead, a robust and well-defined shift can be calculated by averaging the frequencies at the half-maximum points of the line shape, where the slope is largest, and where a Lorentzian fit is most sensitive. This approach incorporates any asymmetries in the line shape into an effective shift in the resonance center, and is consistent with experiment, where the data taken near the half-maximum points is most important for determining the line center.

3.3 Correction to the 2^3P_1 — 2^3P_2 Interval

Computations are carried out for a range of laser intensities I_0 and timing-profile widths T_L to generate the contour plot of Fig. 3.4. The interference shift for the 2^3P_1 — 2^3P_2 interval is shown here, with the black dashed line indicating a resonance with FWHM of 1.8 MHz. This contour value (1.1 times the natural line width of 1.63 MHz) was chosen in accordance with the measured line shape shown in [35], and represents the experimental regime of interest.

The region above the black dashed line corresponds to increasingly higher laser powers and longer interaction times, resulting in wider line shapes and larger shifts. Below this line, where the resonance profiles are narrower and exhibit a smaller interference shift, there is a large area with little variation in the magnitude of the shift, and the interference shift along the black dashed line is approximately constant.

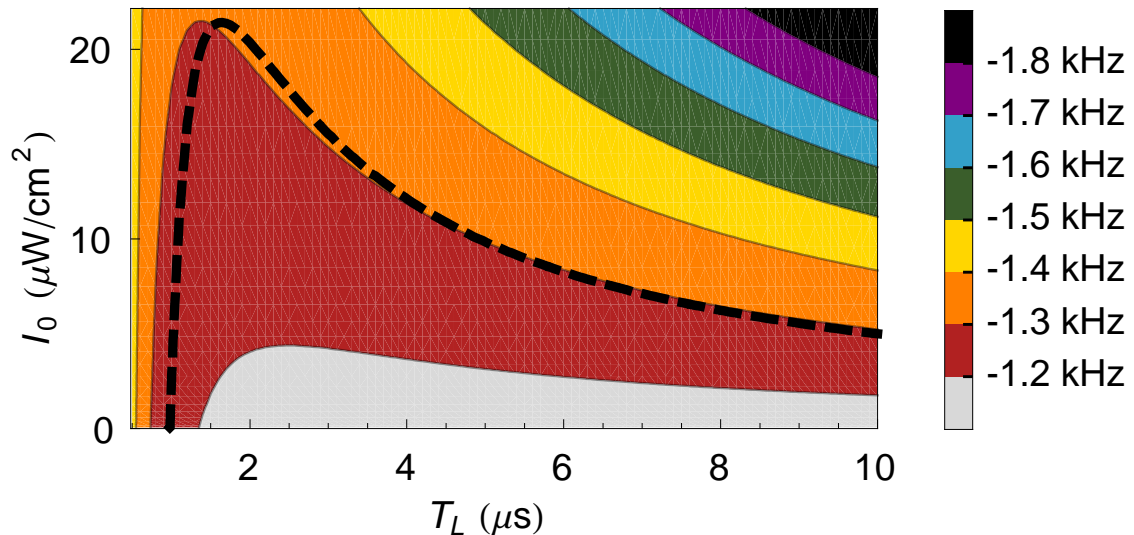


Figure 3.4: A contour plot of the shift (in kHz) for the 2^3P_1 — 2^3P_2 interval as a function of laser intensity and interaction time. The shift is in addition to the small AC Stark shift of Eq. (3.5), and results from quantum-mechanical interference. The dashed-line contour indicates where the FWHM of the resonance is equal to 1.8 MHz (the experimentally observed width).

The experiment of [35] determined the line center of a resonance by sampling pairs of data points about symmetric frequency offsets $\pm\Delta f$ from the center of the transition. Each such measurement yielded a line center f_0 as a function of the slope of the signal $S(f)$ at the frequency step Δf , and the difference between the signal on either side of the peak:

$$f_0 = \frac{1}{2}[S(\Delta f) - S(-\Delta f)] / \left. \frac{dS}{df} \right|_{\Delta f}. \quad (3.6)$$

The majority of data were taken close to the half-maximum of the line shape, where the slope is largest, but other frequency steps were used to test for systematic effects. The measured values of the fine-structure interval as a function of Δf are shown

in Fig. 3.5, with their average value indicated by the blue line.

The authors argued [35] that their data supports the notion that the determination of f_0 was independent of the choice of Δf . As can be seen in panels (c) and (d) of Fig. 3.3, the effect of quantum-mechanical interference on the line shape depends on frequency, so the observed interference shift according to Eq. (3.6) will depend on the choice of Δf . Failure to account for this misses a systematic effect at a level which is significant given the measurement uncertainty.

In the current analysis, each experimental data point is corrected by sampling the computed line shapes at the corresponding frequency offsets $\pm\Delta f$ and applying Eq. (3.6) to calculate the interference shift in the line center caused by the distortion in the resonance profile at those offsets. This procedure results in the values of the fine-structure interval determined using different frequency steps becoming consistent with each other (the red data points in Fig. 3.5).

Of particular note is the point at $\Delta f=1.5$ MHz, which has a 3.2σ discrepancy with the other measurements. The correction due to the relatively larger interference effect at this Δf resolves this discrepancy, bringing the adjusted value in line with the other data points. The final corrected value for the interval (the red dashed line of Fig. 3.5) is $2\,291\,177.1 \pm 1.0$ kHz, which includes an average correction of 1.2 ± 0.1 kHz, consistent with the shifts of Fig. 3.4.

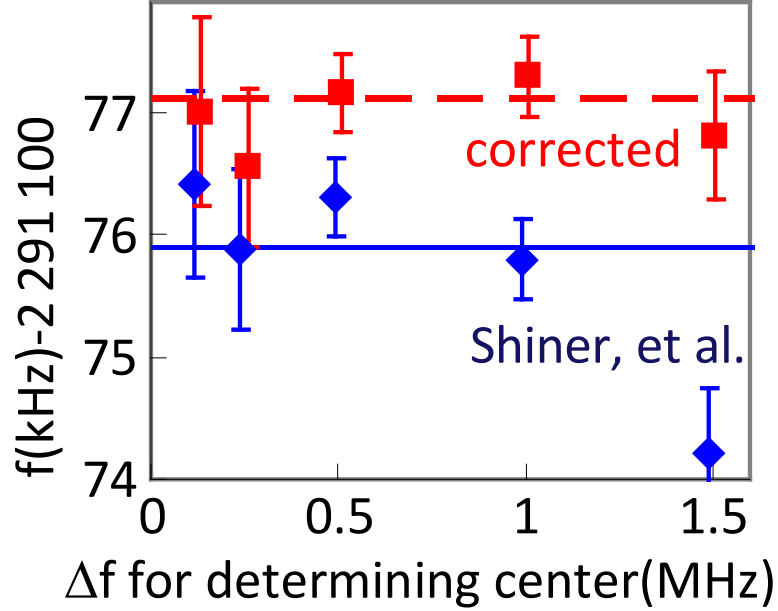


Figure 3.5: The $2^3P_1-2^3P_2$ fine-structure interval inferred from signals at $\pm\Delta f$. The diamonds and uncertainties are from [35], and the solid line is the final result presented in that work. The squares are corrected for the calculated interference shifts.

Another laser measurement of the $2^3P_1-2^3P_2$ interval was made by Hu, et. al. [18], also using a well-collimated atomic beam. This experiment uses transverse laser-cooling to prepare an intense, narrow beam of metastable He atoms in the $2^3S_1(m=1)$ state, and then drives transitions to either $2^3P_1(m=1)$ or $2^3P_2(m=1)$ with a linearly-polarized laser. Radiative decay repopulates the $2^3S_1(m=0)$ state, whose count forms the basis of the measurement signal. The resonant transitions take place in a uniform magnetic field that lifts the degeneracy of the magnetic sub-levels.

The states involved in their measurement are identical to those of Fig. 2.3,

and thus the four-level system of Eqs. (2.11) can once again be used to calculate quantum-interference effects. The four-level model applies even when probing the $2^3S_1(m=1)$ -to- $2^3P_2(m=1)$ transition, as the allowed $2^3S_1(m=0)$ -to- $2^3P_2(m=0)$ transition is Zeeman-shifted out of resonance, and thus $2^3S_1(m=0)$ can still be considered a dark state in this case.

The authors of [18] carried out an analysis of their experiment based on our model, and their reported value of $2\,291\,177.69 \pm 0.36$ kHz for the interval includes an interference correction of 1.21 ± 0.16 kHz. This result is consistent with the preceding treatment which analyzes the shift for the measurement of [35].

4 Saturated-fluorescence Spectroscopy

A determination of the 2^3P fine-structure has also been performed using the technique of saturated-fluorescence spectroscopy [36]. Both the small 2^3P_1 — 2^3P_2 and large 2^3P_0 — 2^3P_1 splittings have been measured, with uncertainties of 11.0 and 1.0 kHz, respectively. Due its higher level of precision, the following analysis of quantum interference focuses on the 2^3P_0 — 2^3P_1 interval.

The saturated-fluorescence method uses a relatively uncollimated atomic beam, whose broad 90 MHz Doppler-width is mitigated by Doppler-free spectroscopy to obtain resonance line widths of the order of 10 MHz. This complicates the calculation of the resonance line shapes, since the fluorescence signal receives contributions from the entire range of transverse velocities present in the atomic beam.

Some experimental parameters of the measurements of Ref. [36] are not known in detail, including the sensitivity of the detector to the polarization of the fluorescence radiation. Therefore, calculations of the interference shifts in the two resonances used to determine the 2^3P_0 — 2^3P_1 interval are done for specific polarizations, and it is seen that the actual interference shift observed would depend on the sensitivity

of the measurement to the polarization states of the emitted radiation. Thus, the effect of quantum interference on the experimental results can only be estimated.

4.1 Measurement Technique

In the saturated-fluorescence measurement of [36], a beam of metastable atoms with a wide angular spread intersects (at a right angle) a pair of counter-propagating laser beams which drive the 2^3S -to- 2^3P transitions. Figure 4.1 shows the energy levels and spontaneous decay paths relevant to the measurement. The initial population is equally distributed among the three metastable ground states, and the fluorescence from spontaneous decay back to 2^3S is detected as the laser scans across the resonance. The two laser beams (created by retro-reflection) are oriented perpendicularly to the center line of the atomic beam, and have identical frequency, waist size, linear polarization, and intensity, which is above the saturation intensity for the transition.

When the laser frequency is tuned close to a resonance, a reduction in fluorescence is observed, resulting in a characteristic, narrow dip in the Doppler-broadened signal. This dip arises because each of the counter-propagating laser beams excites a different group of atoms when the frequency is off-resonance, i.e., addressing only those moving atoms that are Doppler-shifted back into resonance with a particular beam. When the laser is on resonance, however, both beams couple to the same

velocity-class (those atoms with a small transverse velocity), thus exciting fewer atoms and resulting in less fluorescence. In the experiment of [36], this feature has a power-broadened width of approximately 10 MHz, about six times the natural line width.

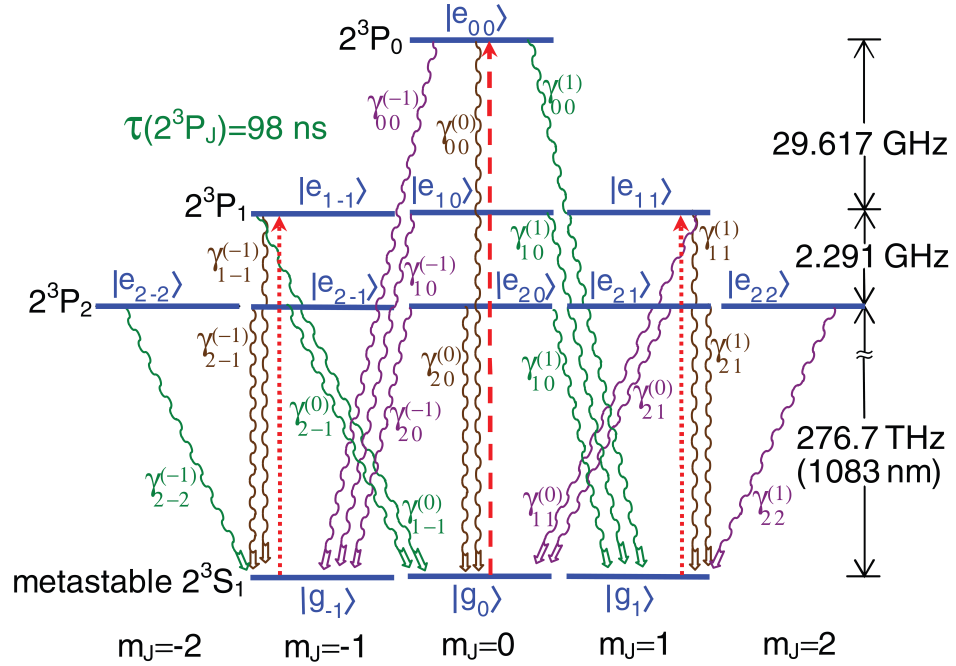


Figure 4.1: Laser-driven transitions for a saturated-fluorescence measurement of the 2^3S_1 -to- 2^3P_1 (dotted lines) and 2^3S_1 -to- 2^3P_0 (dashed line) resonances. All radiative-decay paths are shown, indicating fluorescence with F_+ (green), F_- (purple), and F_0 (brown) polarization.

The driven atomic transitions and spontaneous decays involved in the measurement are shown in Fig. 4.1. The labels F_0 , F_+ and F_- denote fluorescence emitted by radiative decay from an excited state to a metastable state with a change in the magnetic quantum number of $\Delta m_J = 0$, $\Delta m_J = +1$ and $\Delta m_J = -1$, respectively.

When probing the 2^3S_1 -to- 2^3P_1 resonance, metastable atoms in the $2^3S_1(m = \pm 1)$ states (labeled $|g_{\pm 1}\rangle$ in the diagram) are excited by the linearly-polarized laser to $2^3P_1(m = \pm 1)$ (denoted $|e_{1\pm 1}\rangle$), as indicated by the dotted arrows in Fig. 4.1. The atoms can decay to $2^3S_1(m = 0)$ ($|g_0\rangle$ in the figure) by emission of F_{\mp} radiation, remaining in this dark state. Alternatively, decay back to $2^3S_1(m = \pm 1)$ is possible by emission of a linearly-polarized (F_0) photon, and the atoms can then undergo repeated excitation.

Both of these fluorescence channels are affected by quantum-mechanical interference with off-resonant transitions. While the laser is tuned to the 2^3S_1 -to- 2^3P_1 resonance, it also drives the distant 2^3S_1 -to- 2^3P_2 transition, and the two possible decay pathways back to $2^3S_1(m = \pm 1)$ via F_0 fluorescence interfere with each other. These decay paths are shown in Fig. 4.1 by the brown arrows. Similarly, decay by F_{\mp} fluorescence to $2^3S_1(m = 0)$ also involves two interfering processes, indicated by the green arrows for F_+ , and purple arrows for F_- radiation.

When measuring the 2^3S_1 -to- 2^3P_0 transition on the other hand, only those metastable atoms in $2^3S_1(m = 0)$ are driven by the laser to $2^3P_0(m = 0)$ ($|e_{00}\rangle$ in the figure), as indicated by the dashed arrow in Fig. 4.1. Excited atoms can then decay back to $2^3S_1(m = 0)$ through F_0 fluorescence, or to $2^3S_1(m = \pm 1)$ by emission of F_{\pm} radiation.

Once again, both fluorescence processes are perturbed by decays from an off-resonant state, in this case the $2^3P_2(m = 0)$ state ($|e_{20}\rangle$ in the figure). The F_0 fluores-

cence includes interference between decay from either $2^3P_0(m=0)$ or $2^3P_2(m=0)$ to $2^3S_1(m=0)$ while the F_{\pm} radiation resulting from decay to $2^3S_1(m=\pm 1)$ is similarly affected.

4.2 Theoretical Description

4.2.1 Density-matrix Equations

The two laser beams (propagating along \hat{y} and $-\hat{y}$) form a standing wave, with the total electric field experienced by the atom as it passes through the region of interaction given by

$$\vec{E}(t) = \hat{z}E_S(t) \cos(\omega t - \bar{\phi}), \quad (4.1)$$

with a time-dependent envelope

$$E_S(t) = 2E_0 \cos(\Delta\omega_D t + \Delta\phi/2) e^{-2(t-t_L)^2/T_L^2}. \quad (4.2)$$

Here, $E_0 = \sqrt{\frac{2I_0}{\epsilon_0 c}}$, $\bar{\phi}$ and $\Delta\phi$ are the average and difference of the phases of the two laser beams, and I_0 is the peak intensity of a single laser beam, in W/m^2 . The parameter t_L is the time at which the atom passes through the center of the laser beam, while the width T_L determines the interaction time between the atom and the laser, and is based on the speed of the atom and the waist of the laser beam. The Doppler-shift $\Delta\omega_D$ seen by the moving atom also modulates the amplitude of the electric field, so that atoms with a large $\Delta\omega_D$ sample the entire region of

the standing wave between node and anti-node, while at small Doppler shifts, the relative phase of the laser beams determines which part of the standing wave the atom intersects.

Again, using the rotating-wave approximation, one can ignore the non-resonant $e^{-i\omega t}$ term of the cosine in Eq. (4.2). In this approximation, using the notation of Fig. 4.1, the general density-matrix equations for the n=2 triplet states can be written as [31, 34, 39, 40] (see also Appendix A):

$$\dot{\rho}_{g_{\mu}g_{\mu'}} = \sum_{j,m,j',m'} \gamma_{\mu j m}^{\mu' j' m'} \rho_{e_{j m} e_{j' m'}} + \frac{i}{2} \sum_{j,m} \left(\Omega_{\mu' j m}^* \rho_{g_{\mu} e_{j m}} - \Omega_{\mu j m} \rho_{e_{j m} g_{\mu'}} \right) \quad (4.3a)$$

$$\begin{aligned} \dot{\rho}_{e_{j m} e_{j' m'}} &= -i(\omega_j - \omega_{j'}) \rho_{e_{j m} e_{j' m'}} + \frac{i}{2} \sum_{\mu} \left(\Omega_{\mu j' m'} \rho_{e_{j m} g_{\mu}} - \Omega_{\mu j m}^* \rho_{g_{\mu} e_{j' m'}} \right) \\ &\quad - \frac{1}{2} \sum_{\mu, j''} \left(\gamma_{\mu j m}^{\mu' j'' m} \rho_{e_{j'' m} e_{j' m'}} + \gamma_{\mu j' m'}^{\mu' j'' m} \rho_{e_{j m} e_{j'' m'}} \right) \end{aligned} \quad (4.3b)$$

$$\begin{aligned} \dot{\rho}_{g_{\mu} e_{j m}} &= -i(\omega - \omega_j) \rho_{g_{\mu} e_{j m}} - \frac{1}{2} \sum_{\mu', j', m'} \gamma_{\mu' j m}^{\mu' j' m'} \rho_{g_{\mu} e_{j' m'}} \\ &\quad + \frac{i}{2} \sum_{\mu'} \Omega_{\mu' j m} \rho_{g_{\mu} g_{\mu'}} - \frac{i}{2} \sum_{j', m'} \Omega_{\mu j' m'} \rho_{e_{j' m'} e_{j m}} \end{aligned} \quad (4.3c)$$

These equations extend the four-level Eqs. (2.3) to include all of the triplet states, with $\mu = 0, \pm 1$, $j = 0, 1$, or 2 , and $m = -j \dots j$. The diagonal density-matrix elements $\rho_{g_{\mu}g_{\mu}}$ and $\rho_{e_{j m}e_{j m}}$ represent the population in the ground states $|g_{\mu}\rangle$ and excited states $|e_{j m}\rangle$, respectively, while the off-diagonal elements $\rho_{g_{\mu}g_{\mu'}}$, $\rho_{e_{j m}e_{j' m'}}$ and $\rho_{g_{\mu}e_{j m}}$ express correlations between different states.

The Rabi frequencies $\Omega_{\mu jm}(t)$ and generalized decay rates $\gamma_{\mu jm}^{\mu'j'm'}$ are given by the following expressions:

$$\Omega_{\mu jm}(t) = \frac{eE_S(t)}{\hbar} \langle g_\mu | z | e_{jm} \rangle, \quad (4.4a)$$

$$\gamma_{\mu jm}^{\mu'j'm'} = \frac{e^2 \bar{\omega}^3}{3\pi \epsilon_0 \hbar c^3} \langle g_\mu | \vec{r} | e_{jm} \rangle \cdot \langle e_{j'm'} | \vec{r} | g_{\mu'} \rangle. \quad (4.4b)$$

The quantities $\gamma_{\mu jm}^{\mu jm} \equiv \gamma_{jm}^{(\mu)}$ are the partial decay rates from excited states $|e_{jm}\rangle$ to the metastable states $|g_\mu\rangle$ (cf. $\gamma_{i \rightarrow j}$ of Eqs. (2.6)), while the those of the form $\gamma_{\mu jm}^{\mu'j'm'}$ are the cross-damping rates generalizing $\gamma_{23 \rightarrow j}$ of Eq. (2.6), and are responsible for interference effects.

The dipole matrix-elements in Eqs. (4.4) can be calculated using:

$$\langle g_\mu | r_q | e_{jm} \rangle = \frac{(-1)^{1-\mu}}{\sqrt{3}/\sqrt{2j+1}} \begin{pmatrix} 1 & 1 & j \\ -\mu & q & m \end{pmatrix} 4.385 a_0. \quad (4.5)$$

where a_0 is the Bohr radius and the brackets denote a Wigner-3j symbol. The radial factor in Eq. (4.5) is obtained without the use of explicit helium wavefunctions, by equating the theoretical expression for the total rate of decay from the 2^3P_J states to the numerical value $\gamma = 1/\tau$ (where $\tau = 97.9$ ns is the lifetime of the states [41]).

See Appendix B for details.

4.2.2 Reduced Equations

The general density-matrix Eqs. (4.3) comprise 144 coupled equations, whose numerical solution is computationally intensive due to the size of the system and the presence of the large $(\omega_j - \omega_{j'})$ frequency terms. The same reduction process that was applied to the four-level system in chapter 2 can be used to simplify the equations, by considering a laser tuned close to one of the triplet helium levels ($2^3P_{j=J}$), so that very little population is driven to the off-resonant levels ($2^3P_{j' \neq J}$).

As in the four-level case, an ordering parameter η is defined as the ratio of the small frequency scales in Eqs. (4.3) ($\gamma_{\mu jm}^{\mu' j' m'}$, $\Omega_{\mu jm}$, and $\Delta = \omega - \omega_J$) to the large (1000 times greater) fine structure splittings between the resonant and off-resonant states ($\omega_{Jj'} = \omega_J - \omega_{j'}$).

Following [33, 34], the η^2 terms (e.g., $\rho_{e_{j'm} e_{j'm}}$) can be ignored and the density matrix elements of order η (e.g., $\rho_{e_{Jm} e_{j'm}}$ and $\rho_{e_{j'm} g_\mu}$) can be eliminated to give modified equations for the dominant density matrix elements that are complete to

order η :

$$\begin{aligned} \dot{\rho}_{g_\mu g_{\mu'}} &= i(\epsilon_{\mu'} - \epsilon_\mu) \rho_{g_\mu g_{\mu'}} + \frac{i}{2} \sum_m \left[\Omega_{\mu' J m}^* \rho_{g_\mu e_{J m}} - \Omega_{\mu J m} \rho_{e_{J m} g_{\mu'}} \right] \\ &+ \sum_{m, \mu''} \left[\zeta_{\mu \mu' \mu''}^{J m} \rho_{g_{\mu''} e_{J m}} + (\zeta_{\mu' \mu \mu''}^{J m})^* \rho_{e_{J m} g_{\mu''}} \right] + \sum_{m, m'} \gamma_{\mu J m}^{\mu' J m'} \rho_{e_{J m} e_{J m'}} \end{aligned} \quad (4.6a)$$

$$\dot{\rho}_{e_{J m} e_{J m'}} = -\gamma \rho_{e_{J m} e_{J m'}} - \frac{i}{2} \sum_\mu \left[\Omega_{\mu J m}^* \rho_{g_\mu e_{J m'}} - \Omega_{\mu J m'} \rho_{e_{J m} g_\mu} \right] \quad (4.6b)$$

$$\begin{aligned} \dot{\rho}_{g_\mu e_{J m}} &= \frac{i}{2} \sum_{\mu'} \Omega_{\mu' J m} \rho_{g_\mu g_{\mu'}} - \frac{i}{2} \sum_{m'} \Omega_{\mu J m'} \rho_{e_{J m'} e_{J m}} \\ &- \frac{1}{2} \sum_{\mu'} \gamma_{\mu' J m}^{\mu' J m} \rho_{g_\mu e_{J m'}} - i(\omega - \omega_J + \epsilon_\mu) \rho_{g_\mu e_{J m}} \end{aligned} \quad (4.6c)$$

The first-order corrections due to interference with off-resonant states (those with $j' \neq J$) are expressed as:

$$\epsilon_\mu = \sum_{j' \neq J, m'} \frac{|\Omega_{\mu j' m'}|^2}{4\omega_{J j'}} \quad (4.7a)$$

$$\zeta_{\mu \mu' \mu''}^{J m} = \sum_{j \neq J, m'} \frac{\Omega_{\mu' j m}^* \gamma_{\mu j m'}^{\mu' J m}}{2\omega_{J j}} \quad (4.7b)$$

The ϵ_μ terms in Eq. (4.7) correspond to the AC-Stark shift corrections in Eqs. (2.11)(c), while the quantities $\zeta_{\mu \mu' \mu''}^{J m}$ are the generalized equivalents of the interference shift terms in Eq. (2.11)(a).

Eqs. (4.6) give 16, 36 or 64 equations for $J=0, 1$ or 2 , respectively. They lack the fast oscillations found in Eqs. (4.3), and thus require a factor of η (3 orders

of magnitude) fewer time steps for the numerical integration. The results of these integrations agree with those from Eqs. (4.3) to order η^2 (i.e., to better than a part per million).

4.3 Fluorescence Lineshapes

The fluorescence emitted by the laser-excited atoms can be obtained from the spontaneous-decay terms in the $\dot{\rho}_{e_{jm}e_{j'm'}}$ equation of Eqs. (4.3). The fluorescence has three components F_q ($q=0, \pm 1$) which correspond to radiative decay from the 2^3P_J state to the 2^3S_1 state with $\Delta m_J=0, \pm 1$ respectively. The fluorescence F_q is therefore given by

$$F_q = \int_{t_i}^{t_f} dt \sum_{\mu, j, m, j'} \delta_{\mu}^{m+q} \frac{\gamma_{\mu j m}^{\mu j' m}}{2} \left(\rho_{e_{j'm}e_{jm}} + \rho_{e_{jm}e_{j'm}} \right). \quad (4.8)$$

Here the Kronecker delta selects the component of the fluorescence based on the m_J quantum numbers of the upper and lower states, and the integration is over the time that the moving atom spends in the laser beam.

Applying a similar reduction technique as was done for the density-matrix equations, an expression for the terms in Eq. (4.8) that is correct to first order in η can be found:

$$F_q = \int_{t_i}^{t_f} dt \sum_{\mu, m} \delta_{\mu}^{m+q} \left\{ \gamma_{\mu J m}^{\mu J m} \rho_{e_{Jm}e_{Jm}} + \sum_{\mu'} [\zeta_{\mu\mu\mu'}^{Jm} \rho_{g_{\mu'}e_{Jm}} + (\zeta_{\mu\mu\mu'}^{Jm})^* \rho_{e_{Jm}g_{\mu'}}] \right\}. \quad (4.9)$$

For any given set of parameters I_0 , T_L , $\Delta\phi$ and $\Delta\omega_D = 2\pi\Delta f_D$, the solutions to Eqs. (4.6) can be used to obtain F_q from Eq. (4.9). Equal initial populations are

assumed for the three metastable states $|g_\mu\rangle$. As was done in Chap. 3, the system of equations is integrated using an adaptive-step solver. The integration starts at a time $2T_L$ before the peak time t_L (here T_L and t_L are the full width and center of the Gaussian envelope in Eq. (4.2), respectively), and the total integration time is chosen to be $t_f = 4T_L + 5\tau$, so that the atoms have completely passed through the laser beam, with the additional five lifetimes ensuring that the population has decayed to the metastable state.

The F_0 fluorescence profiles for the $J=1$ case (the 2^3S_1 -to- 2^3P_1 transition) using $I_0=2$ mW/cm² and $T_L=1$ μ s are shown in Fig. 4.2(a) for the $\Delta f_D=0$ ($v_y=0$) Doppler group. Solutions for various values of the relative phase $\Delta\phi$ are plotted, and it is evident that the signal depends strongly on the phase angle. When the laser beams are in phase, this corresponds to interaction with a maximum in the standing wave field, resulting in maximum fluorescence, while at $\Delta\phi = \pi$, the atoms are passing through a node in the laser field and the fluorescence vanishes since no atoms are excited.

When the calculations are repeated using a slightly larger Δf_D (larger v_y) of 0.4 MHz, the dependence on $\Delta\phi$ weakens quickly, as seen in Fig. 4.2(b). The atoms now have a large enough transverse velocity to sample all portions of the standing wave during their interaction with the laser. Since the relative phase varies in practice, an average over all values of $\Delta\phi$ is taken when computing the fluorescence profile, especially for small Doppler groups, as shown by the solid lines in Fig. 4.2(a), (b),

and (c).

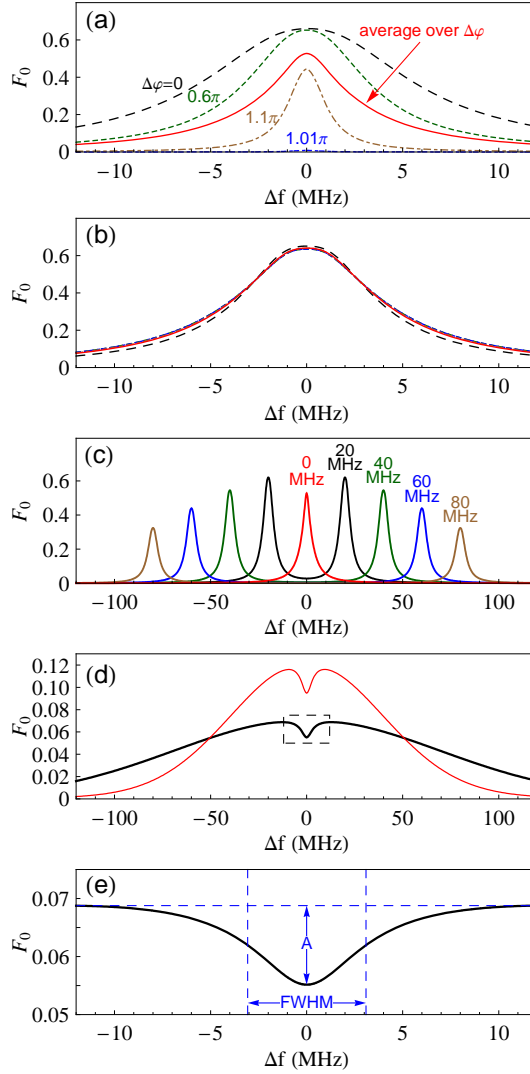


Figure 4.2: The fluorescence signals F_0 as a function of detuning Δf from the 2^3S_1 -to- 2^3P_1 resonance. Individual Doppler groups Δf_D , (a)–(c), give resonances at $\Delta f = \pm\Delta f_D$. For small Δf_D , F_0 depends on the relative phase, as shown for four values of $\Delta\phi$ in (a). At larger Δf_D , the dependence is reduced substantially, as shown for the same values of $\Delta\phi$ for $\Delta f_D = 0.4$ MHz in (b). The solid curves represent averages over $\Delta\phi$. The average of F_0 over all Doppler groups leads to the saturated fluorescence dip, as shown in (d) for $\Delta f_D^{\text{HWHM}} = 45$ MHz (thin red line) and 80 MHz (thick line). An expanded view of the saturated fluorescence dip within the dashed area in (d) is shown in (e), along with the amplitude (A) and full width at half maximum (FWHM) of the dip.

Each Doppler group in the atomic beam contributes its own fluorescence signal, with dual resonances at $\Delta f = \pm \Delta f_D$, as seen in Fig. 4.2(c) for a few representative Doppler groups. The total F_0 fluorescence signal is then computed as a weighted average over all Doppler groups present in the beam. A Gaussian velocity distribution is assumed, with half-width-at-half-maximum of Δf_D^{HWHM} , and Fig. 4.2(d) shows the resulting line shape for values of $\Delta f_D^{\text{HWHM}} = 45$ MHz (thin red line) and 80 MHz (thick line). The reduced signal near resonance is the saturated-fluorescence dip, and is shown in an expanded view in Fig. 4.2(e) with its amplitude (A) and FWHM indicated.

The amplitude and width of the dip as a function of laser intensity I_0 are shown in Fig. 4.3(a) and (b), respectively, for three values of interaction time T_L . For the dip to have a substantial amplitude, the laser intensity must be above the saturation intensity for the transition, causing the width to be significantly broadened relative to the 1.6-MHz natural line width. For precision measurements of the saturated-fluorescence dip, there is therefore a trade-off between the signal amplitude and width.

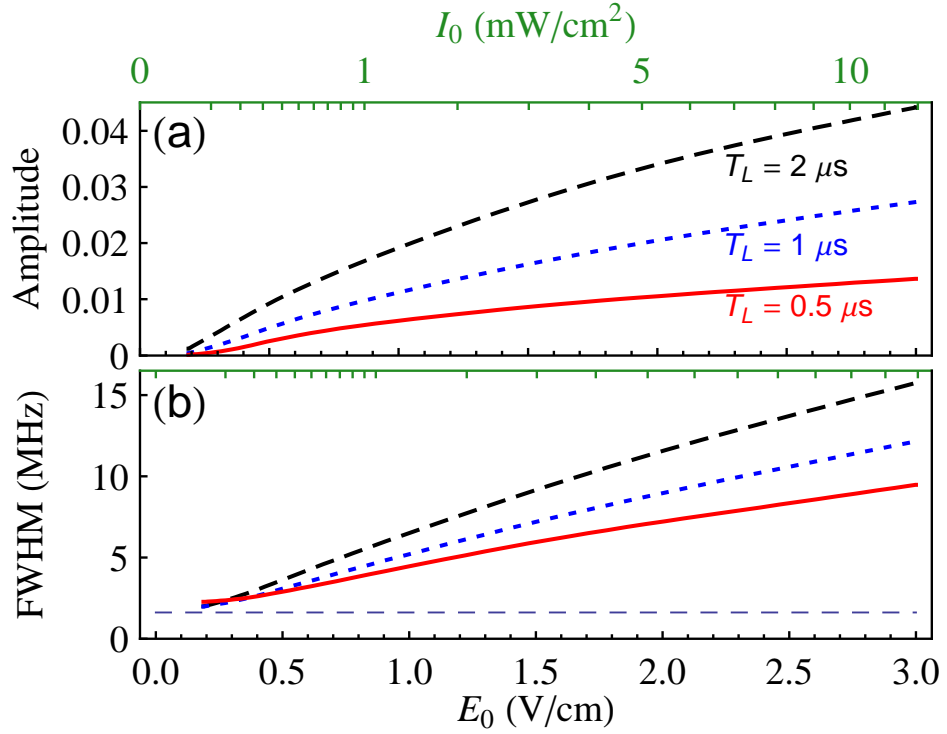


Figure 4.3: The amplitude (a) and width (b) of the 2^3S_1 -to- 2^3P_1 saturated-fluorescence dip as a function of intensity I_0 , for three choices of interaction time T_L . The natural width is shown as a thin dashed line in (b). The width of the dip is significantly broader than the natural width for intensities that lead to dips of substantial amplitude.

4.4 AC-Stark Shifts

It is instructive to first consider only the AC-Stark shifts of the fluorescence signal. These shifts are isolated when interference effects are artificially suppressed, by setting the off-diagonal $\gamma_{\mu jm}^{\mu' j' m'}$ terms to zero in Eqs. (4.6) and (4.9). The AC-Stark shift, resulting from the ϵ_μ terms of Eqs. (4.7), moves all of the resonances of Figs. 4.2(a), (b) and (c) to the left (for all Doppler groups).

The net amount of shift in the fluorescence dip however, is quite complicated, due to the many parameters in the electric field amplitude of Eq. (4.2) that affect the line shape. Firstly, the atom-laser interaction time T_L determines how many cycles of excitation and decay the atom undergoes, and thus the amount of fluorescence produced. The laser intensity I_0 also plays a role in the magnitude of the signal, and both T_L and I_0 cause broadening of the resonance.

The dependence on the phase difference $\Delta\phi$ is also significant for the small Doppler groups which contribute the most to the central dip. As the average is taken over all the phases, this includes cases of constructive interference ($\Delta\phi=0$ of Fig. 4.2(a)) which lead to both a large resonance and a large shift, as well as destructive interference ($\Delta\phi\approx\pi$ in the same figure) which produces no signal and no shift.

Finally, the shift is complicated by the Δf_D dependence, in that a leftward shift of the peak in small Δf_D contributions, such as the $\Delta f_D=0$ curve in Fig. 4.2(c), causes the dip of Fig. 4.2(d) to move to the right. Conversely, the profiles at higher Δf_D , such as the $\Delta f_D=20$ MHz line in Fig. 4.2(c), have minima rather than peaks at the center, so the leftward shift of these Doppler profiles causes the dip to shift to the left instead.

Fig. 4.4(a) shows the integrated contribution to the AC-Stark shift for all Doppler groups in the range $-|\Delta f_D|$ to $|\Delta f_D|$, assuming a Gaussian distribution of Doppler groups with $\Delta f_D^{\text{HWHM}} = 80$ MHz. The shifts are determined from the fre-

quencies of the half-maximum points of the line shapes obtained from the numerical integration and averaging over Doppler groups and phases $\Delta\phi$ (see Fig. 4.2(e)).

One observes that the net AC-Stark shift from all Doppler groups is negative, as can be seen from the values on the right side of Fig. 4.4(a), with positive shifts for low Δf_D , and larger negative shifts for intermediate Δf_D . The curves of Fig. 4.4(a) approach their final values at $\Delta f_D \sim 30$ MHz, since the contributions from the larger Doppler groups (cf. Fig. 4.2(c)) are well-separated in frequency from the saturated-fluorescence dip.

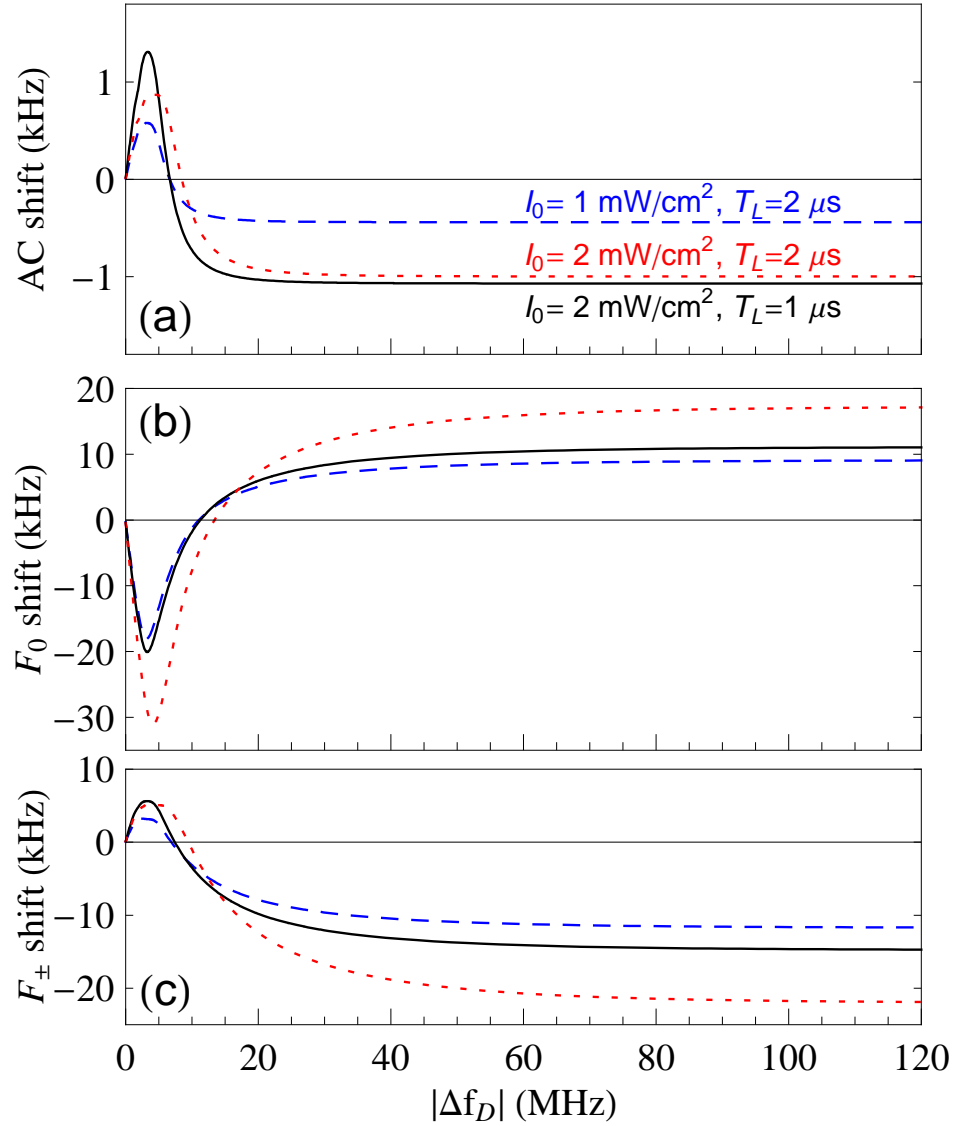


Figure 4.4: The cumulative AC-Stark shifts (a) and interference shifts (b) and (c) of the 2^3S_1 -to- 2^3P_1 saturated-fluorescence dips for various choices of intensity (I_0) and interaction time (T_L). The graphs display integrated shifts due to Doppler groups ranging from $-\lvert\Delta f_D\rvert$ to $\lvert\Delta f_D\rvert$ and show that the shifts change sign for larger Doppler groups. The total shift (from all Doppler groups) is the value at the right of each curve. The F_0 shifts for linearly-polarized fluorescence in (b) and the $F_{\pm 1}$ shifts for circularly-polarized radiation in (c) are of opposite sign due to the opposite signs in the respective γ_{111}^{121} and γ_{011}^{021} cross-damping factors.

Shifts for a larger range of interaction times T_L and intensities I_0 are shown in Table 4.1 and in Figs. 4.5(a) and (b). The AC-Stark shifts are identical for F_{-1} , F_0 , and F_{+1} fluorescence. Note that the net shifts depend mostly on I_0 , as expected for AC-Stark shifts, but there is dependence on T_L as well. These shifts are small compared to the interference shifts discussed in the next section.

Table 4.1: AC-Stark and interference shifts for F_0 and $F_{\pm 1}$ fluorescence, in kHz. The shifts are given for a selection of interaction times T_L and laser electric-field amplitudes E_0 . A Doppler profile with $\Delta f_D^{\text{HWHM}}=80$ MHz is assumed. The middle three columns list the shifts in the fluorescence dips for the 2^3S_1 -to- 2^3P_0 resonance, using the AC-Stark-only signal (same for all polarizations), the linearly-polarized fluorescence (F_0), and the circularly-polarized fluorescence ($F_{\pm 1}$) signals respectively. The last three columns are similar results for the 2^3S_1 -to- 2^3P_1 transition.

E_0 (V/cm)	T_L (μ s)	2^3S_1 -to- 2^3P_0			2^3S_1 -to- 2^3P_1		
		AC	F_0	$F_{\pm 1}$	AC	F_0	$F_{\pm 1}$
0.375	0.25	0.09	0.03	-0.08	0.62	0.26	-1.16
0.375	0.5	0.03	0.08	-0.10	0.21	0.47	-1.48
0.375	1	0.01	0.11	-0.13	0.07	0.67	-2.07
0.375	1.5	0.00	0.15	-0.16	0.01	0.89	-2.49
0.375	2	0.00	0.18	-0.18	-0.01	1.15	-2.89
0.375	4	-0.01	0.35	-0.28	-0.06	2.38	-4.47
0.75	0.25	0.05	0.14	-0.14	0.21	1.12	-2.23
0.75	0.5	-0.01	0.28	-0.24	-0.17	2.45	-4.51
0.75	1	-0.02	0.48	-0.37	-0.26	3.74	-6.37
0.75	1.5	-0.03	0.65	-0.47	-0.30	4.95	-7.80
0.75	2	-0.03	0.83	-0.56	-0.31	6.22	-9.23
0.75	4	-0.03	1.51	-0.94	-0.33	11.3	-14.8
1.5	0.25	-0.25	0.98	-0.67	-3.41	12.8	-17.0
1.5	0.5	-0.17	1.48	-0.94	-2.04	13.4	-17.0
1.5	1	-0.15	2.06	-1.25	-1.72	17.0	-21.1
1.5	1.5	-0.15	2.64	-1.55	-1.63	21.2	-25.3
1.5	2	-0.14	3.22	-1.85	-1.56	25.5	-29.8
1.5	4	-0.14	5.48	-3.01	-1.50	42.7	-47.1
2.25	0.25	-0.54	2.87	-1.68	-3.91	19.5	-21.7
2.25	0.5	-0.47	3.36	-1.88	-5.31	30.7	-33.4
2.25	1	-0.38	4.43	-2.42	-4.18	37.4	-40.4
2.25	1.5	-0.35	5.56	-2.99	-3.82	45.8	-48.5
2.25	2	-0.34	6.72	-3.57	-3.65	54.6	-56.8
2.25	4	-0.33	11.2	-5.70	-3.46	89.8	-88.3
3	0.25	-0.68	3.30	-1.71	-11.0	40.0	-38.6
3	0.5	-0.86	5.79	-2.97	-9.79	53.7	-52.8
3	1	-0.68	7.44	-3.80	-7.60	64.6	-63.5
3	1.5	-0.63	9.29	-4.70	-6.89	78.3	-75.9
3	2	-0.61	11.2	-5.58	-6.57	92.8	-88.5
3	4	-0.59	18.6	-8.77	-6.21	152	-136

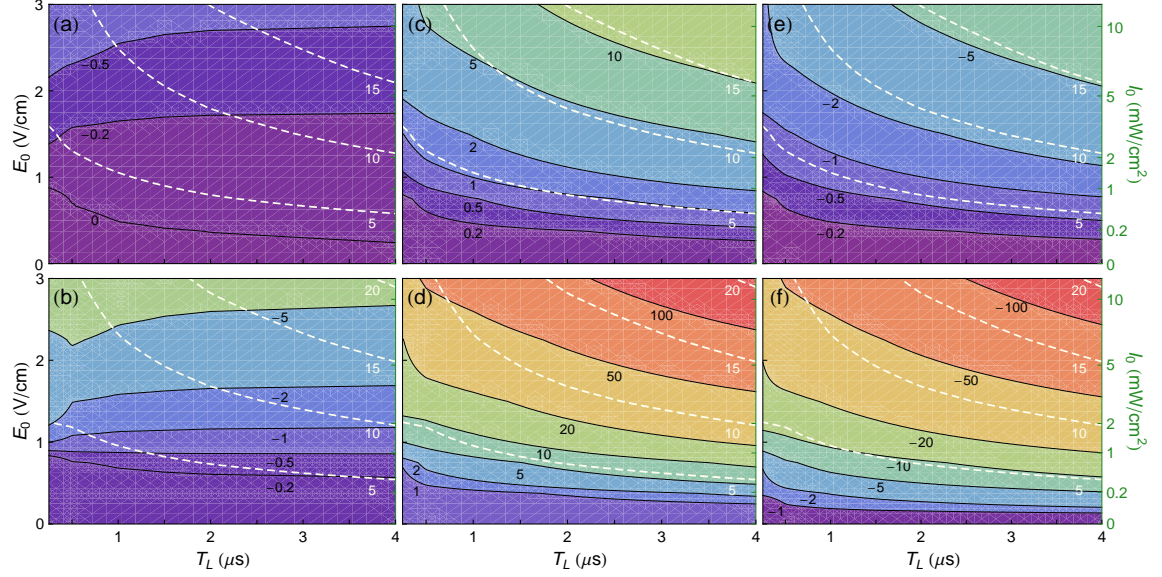


Figure 4.5: Contour graphs for AC-Stark and interference shifts versus interaction times T_L and laser intensities I_0 . Top row (a,c,e): 2^3S_1 -to- 2^3P_0 transition, bottom row (b,d,f): 2^3S_1 -to- 2^3P_1 transition. Plots (a) and (b) represent AC-Stark shifts, while plots (c) and (d) show interference shifts (to be added to the AC-Stark shift) for $\Delta mJ = 0$ decays [F_0 in Eq. (4.9)], and (e) and (f) are interference shifts for $F_{\pm 1}$ fluorescence. A Doppler profile with $\Delta f_D^{\text{WHM}} = 80$ MHz is used. The shift values, given along the black contour lines, are in kHz. Also shown on the plots (white dashed lines) are the widths of the saturated-fluorescence dips in MHz.

4.5 Interference Shifts

The interference shifts are obtained in the same way as the AC-Stark shifts in the previous section, except that the numerical integration of Eq. (4.9) now includes the off-diagonal $\gamma_{\mu j m}^{\mu' j' m'}$ cross-damping terms.

The fluorescence line shapes are similarly complicated by their dependence on laser intensity I_0 and atom-laser interaction time T_L , as well as the averaging over the relative beam phase $\Delta\phi$ and Doppler groups Δf_D present in the atomic beam.

As with the AC-Stark shift, the interference shifts are determined from the frequencies of the calculated half-maximum points of the saturated fluorescence dips, and Figs. 4.4(b) and (c) show that the sign of the shift also changes with increasing values of $|\Delta f_D|$. The size of the shifts is an order of magnitude larger than that of the AC-Stark shifts, and the final values of the shifts for F_0 and F_{\pm} fluorescence are of opposite sign.

More detailed results of the calculations (for a Doppler profile with $\Delta f_D^{\text{HWHM}}=80$ MHz) are shown in Table 4.1 and Fig. 4.5. The interference shifts in both the table and the figure do not include the AC-Stark shifts discussed in the previous section. The contour graphs show that the interference shifts depend strongly on both T_L and I_0 . In an actual experiment, the shift for different atoms in the beam would differ, since I_0 depends on which part of the Gaussian laser beam the atom intersects, while T_L depends on the axial velocity component of the atom.

The shifts (in kHz) shown in Fig. 4.5(a), (c), and (e) are for the 2^3S_1 -to- 2^3P_0 transition, while those in Fig. 4.5(b), (d), and (f) are for 2^3S_1 -to- 2^3P_1 . The plots (c) and (d) display interference shifts for $\Delta m_J = 0$ decays (F_0 in Eq. (4.9)), and (e) and (f) show interference shifts for $F_{\pm 1}$. The corresponding AC-Stark shifts are shown in parts (a) and (b), respectively. The white dashed lines on the plots show the corresponding widths of the saturated-fluorescence dips in MHz.

Table 4.2 shows shifts for other Doppler profiles. From this table it can be seen that the interference shift also depends on which Doppler groups are present in the

Table 4.2: Dependence of AC-Stark and interference shifts on the width (Δf_D^{HWHM}) of the beam's Doppler profile. Shifts in the 2^3S_1 -to- 2^3P_1 saturated fluorescence dip, along with its FWHM and amplitude A , are given for two laser intensities I_0 and two interaction times T_L .

I_0 (mW/cm ²)	T_L (μ s)	Δf_D^{HWHM} (MHz)	AC (kHz)	F_0 (kHz)	$F_{\pm 1}$ (kHz)	FWHM (MHz)	A
1	1	30	-0.45	3.8	-6.1	4.00	0.032
1	1	45	-0.43	4.5	-7.1	4.33	0.024
1	1	60	-0.42	4.9	-7.7	4.52	0.019
1	1	80	-0.41	5.2	-8.2	4.68	0.015
1	1	110	-0.41	5.6	-8.7	4.82	0.011
2	1	30	-1.10	8.2	-10.6	5.05	0.041
2	1	45	-1.09	9.5	-12.5	5.57	0.032
2	1	60	-1.08	10.4	-13.8	5.89	0.026
2	1	80	-1.07	11.3	-15.1	6.16	0.020
2	1	110	-1.06	12.0	-16.2	6.40	0.016
1	2	30	-0.48	6.4	-8.6	4.93	0.054
1	2	45	-0.47	7.4	-10.1	5.34	0.040
1	2	60	-0.46	8.0	-11.0	5.59	0.032
1	2	80	-0.45	8.5	-11.9	5.79	0.025
1	2	110	-0.44	9.0	-12.7	5.97	0.019
2	2	30	-1.04	13.0	-14.6	6.36	0.067
2	2	45	-1.03	14.8	-17.5	7.02	0.053
2	2	60	-1.02	16.1	-19.5	7.42	0.043
2	2	80	-1.01	17.3	-21.4	7.76	0.035
2	2	110	-1.00	18.4	-23.2	8.08	0.027

beam, as would be expected from the dependence on Δf_D shown in Figs. 4.4(b) and (c). The table shows that the interference shifts for a beam with a Doppler width $\Delta f_D^{\text{HWHM}}=110$ MHz are approximately 50% larger than those for $\Delta f_D^{\text{HWHM}}=30$ MHz.

4.5.1 Scale and Sign of Interference Shifts

The interference shift results from quantum-mechanical interference between the amplitude for obtaining fluorescence via an on-resonance laser excitation and the much smaller amplitude for fluorescence via a far-off-resonance transition to a distant state. For example, the shift in the $2^3S_1(m=0)$ -to- $2^3P_0(m=0)$ transition (the dashed arrow in Fig. 4.1) is due to the far-off-resonance $2^3S_1(m=0)$ -to- $2^3P_2(m=0)$ transition, which is 31.9 GHz away (20 000 natural widths), yet still perturbs the saturated-fluorescence line shape at a level (5 kHz in 10MHz) that is relevant for precision spectroscopy.

As is the case for other instances of interference shifts due to off-resonant transitions [33, 34, 42, 43], the scale of the shifts is given by the ratio of the square of the resonance width to the frequency separation between the interfering resonances. This scaling can be seen in Fig. 4.5(c)-(f), where the resonance width contours have the same general shape as the interference shift contours.

The opposite sign of the shifts for the different polarizations of fluorescence (positive for the F_0 shifts and negative in the case of the $F_{\pm 1}$ shifts) is a direct result of the opposite signs of γ_{000}^{020} and $\gamma_{\pm 100}^{\pm 120}$. The first of these cross-damping rates (γ_{000}^{020}) is relevant for the production of F_0 fluorescence, where there is interference as $2^3S_1(m=0)$ atoms are laser-excited to both the on-resonant $2^3P_0(m=0)$ state and the far-off-resonant $2^3P_2(m=0)$ state, followed by decay back down to

the $2^3S_1(m=0)$ state. The second rate ($\gamma_{\pm 100}^{\pm 120}$) determines the amount of interference when $2^3S_1(m=0)$ atoms are driven to the same $2^3P_0(m=0)$ and $2^3P_2(m=0)$ excited states, but decay down to the $2^3S_1(m=\pm 1)$ states instead, with the emission of circularly-polarized $F_{\pm 1}$ fluorescence. In a typical saturated-fluorescence measurement (e.g., [11, 14, 36, 44]), the width of the saturated-fluorescence dip is approximately 10 MHz (about 6 natural linewidths). Referring to Figs. 4.5(c) and (e) one can see resultant shifts with magnitudes between 3 and 6 kHz.

Whether a measured signal is subject to a net positive or negative shift depends on the detector's relative sensitivity to F_0 vs. $F_{\pm 1}$ fluorescence. For example, if the fluorescence detector is placed above the laser beam (in the \hat{z} direction), it is sensitive only to $F_{\pm 1}$ fluorescence since the angular distribution of F_0 fluorescence is zero in this direction. In general, the shift is some linear combination of the shifts of Figs. 4.5(c) and (e), with proportions that depend on the geometry of the experiment and the polarization sensitivity of the detectors.

This strong dependence on detector geometry and sensitivity to the polarization of the measured fluorescence was shown to be important in measurements of the hyperfine D-lines in atomic lithium [32, 45], where interference effects are substantial since the splitting between the relevant neighboring excited states is of the order of their line widths.

The shifts for the 2^3S_1 -to- 2^3P_1 transition (the dotted arrows in Fig. 4.1) are much larger, since for this case the neighboring resonance (the 2^3S_1 -to- 2^3P_2 tran-

sition) is 1400 natural widths away. These shifts are shown in Figs. 4.5(d) and (f) for F_0 and $F_{\pm 1}$ fluorescence. Shifts of between 30 and 60 kHz for 10-MHz-wide saturated-fluorescence dips can be seen on the contour graphs, which are very large compared to the kHz or sub-kHz uncertainties of recent measurements [9–17, 35, 36, 46] of the intervals. As before, F_0 and $F_{\pm 1}$ have opposite shifts, so again the actual shift seen by a saturated-fluorescence experiment depends on the sensitivity and geometry of the fluorescence detector.

With regard to the measurement of [36], a determination of the interference shift to $\lesssim 1$ kHz level of accuracy is not feasible given the lack of some details about the experiment. It is evident from Table 4.1, Table 4.2 and Fig. 4.5 that the shifts depend strongly on model parameters such as the peak laser intensity I_0 , the Doppler-width Δf_D^{HWHM} of the atomic beam, and the atom-laser interaction time T_L . This latter quantity is itself a function of the laser beam’s waist and the atomic beam’s angular spread and speed distribution.

A realistic calculation of the saturated-fluorescence signal would involve a properly weighted average over line shapes for atoms that experience a range of values of T_L , I_0 , and Δf_D . Such a simulation would require detailed information about the possible trajectories of an atom through the laser beam, which depends on the laser beam power and waist, as well as the distribution of velocities in the atomic beam.

Furthermore, as previously mentioned, the detector geometry and sensitivity

to fluorescence of different polarizations must be carefully modeled, in order to correctly combine the opposing shifts with their relative weights. This involves specification (at the percent level of accuracy) of the placement and aperture of the detectors, and their relative efficiency for different polarizations of light.

Although some cancellation can be expected between the positive and negative shifts for most detector geometries, the scale of the expected shifts is still of the order of 10 kHz, and therefore must be estimated for precision measurements of the intervals. In summary, a specific correction to the measured value of the 2^3P_0 — 2^3P_1 interval due to quantum interference is not given, but an increased uncertainty of ± 10 kHz is proposed to reflect the scale of the residual shift.

5 Saturated-absorption Spectroscopy

Precision measurements of all three 2^3P fine-structure intervals have been performed using saturated-absorption spectroscopy in a gas cell [15], so it is important to understand the scale of interference effects on this type of laser measurement. The technique presents its own set of systematic challenges, and consequently this chapter analyzes only the 2^3P_1 — 2^3P_2 interval, as measurements of the other 2^3P intervals are complicated by shifts due to deflection of the atoms by laser light. Interference shifts are obtained [47] for this interval that are larger than the uncertainty of the saturated-absorption measurement of [15].

5.1 Measurement Technique

The saturated-absorption technique uses a sample of dilute helium gas in a cell, where a dc discharge excites a tiny fraction of the atoms to the metastable 2^3S state. A linearly-polarized laser then excites the atoms to the 2^3P states, and the transmission of the beam is detected after it has passed through the atomic cloud. A uniform external magnetic field lifts the degeneracy of the magnetic sub-levels,

and isolates the individual 2^3S -to- 2^3P transitions for $m_J=-1,0$, and $+1$ states, separating each resonance.

The measurement is performed both with a single laser beam, and also with a second counter-propagating beam present, and the saturated-absorption signal is formed from the difference in the absorption of the forward beam between the two cases. As the laser frequency is tuned across the resonance, decreased absorption of the forward beam is observed when both beams are on. This reduction is caused by the Doppler shifts seen by the moving thermal atoms.

When the laser frequency is near resonance, both beams address the same group of atoms (those nearly at rest), which can absorb photons from either laser beam with equal probability, resulting in less absorption from the forward beam. When tuned off-resonance, however, each laser beam couples to a different group of moving atoms, each of which absorbs photons from a separate beam. The resulting saturated-absorption signal has a line width much narrower than the Doppler-broadened laser resonance, and can approach the natural width of the resonance in the limit of low laser power.

The triplet states involved in the saturated-absorption measurement of the 2^3P_1 — 2^3P_2 interval are shown in Fig. 5.1, and were previously shown in Fig. 2.3 to illustrate the four-level atom.

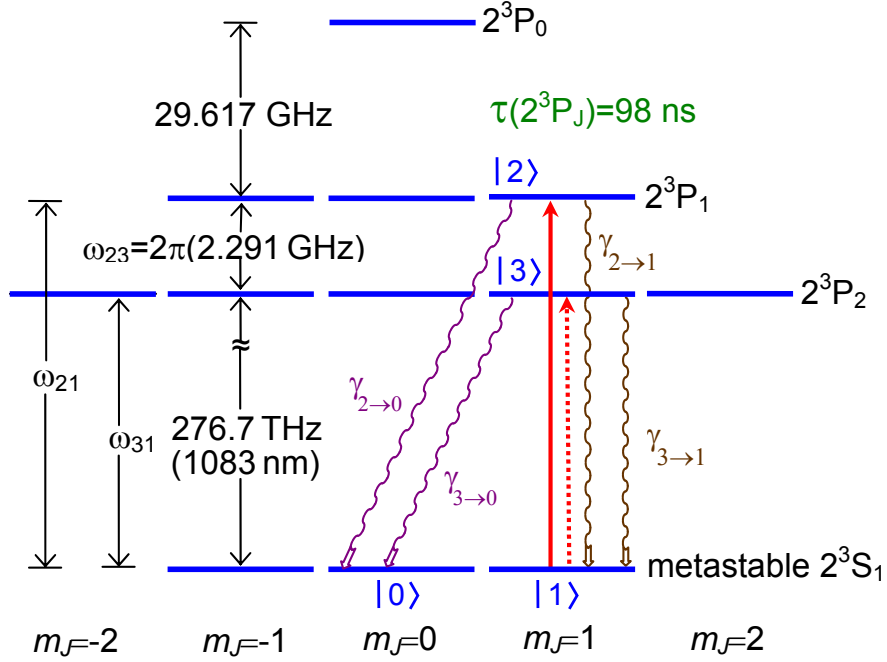


Figure 5.1: The $n=2$ triplet energy levels of helium, illustrating states involved in the saturated-absorption measurement of the $2^3S_{1,m_J=1}$ -to- $2^3P_{1,m_J=1}$ transition. Both resonant (solid arrow) and off-resonant (dotted arrow) transitions are shown, along with possible decay pathways.

This diagram depicts an experiment probing the $2^3S_{1,m_J=1}$ -to- $2^3P_{1,m_J=1}$ transition frequency. Atomic population starting in the metastable state $|1\rangle$ ($2^3S_{1,m_J=1}$) is excited by a linearly-polarized laser tuned close to the $|1\rangle \rightarrow |2\rangle$ resonance. Most of the transfer (solid arrow) is to state $|2\rangle$ ($2^3P_{1,m_J=1}$), but there is a small amplitude (dotted arrow) to reach the far-off-resonance state $|3\rangle$ ($2^3P_{2,m_J=1}$). The atom then can radiatively decay back to $|1\rangle$ or to the $|0\rangle$ state ($2^3S_{1,m_J=0}$). The latter is a dark state since the $2^3S_{1,m_J=0}$ -to- $2^3P_{1,m_J=0}$ transition is electric-dipole-forbidden.

Tuning the laser frequency to the $2^3P_{2,m_J=1}$ state reverses the roles of $|2\rangle$ and $|3\rangle$ as dominant and off-resonant state, respectively, and probes the $2^3S_{1,m_J=1}$ -to- $2^3P_{2,m_J=1}$ transition instead, with the difference of the two transition frequencies used to determine the fine-structure interval. Although this latter case is not strictly a closed four-level system (since the $2^3S_{1,m_J=0}$ -to- $2^3P_{2,m_J=0}$ transition is not dipole-forbidden), the large Zeeman shift effectively suppresses the transition out of $2^3S_{1,m_J=0}$, so $|0\rangle$ can still be treated as dark state, and the four-level model is recovered.

In either case, there is quantum-mechanical interference between the two processes of resonant vs. off-resonant excitation and subsequent decay. As discussed in chapter 2, this leads to a perturbation of the branching ratio for decay to the $|0\rangle$ dark state compared to decay back to the metastable $|1\rangle$ state, where the atom can be repeatedly excited to remove photons from the laser field. This effect translates to a distortion and a resultant shift in the absorption profile as the laser scans over the resonance.

5.1.1 Systematic Effects

The saturated-absorption measurement of [15] must be corrected for several systematic effects. The first of these are velocity-changing collisions (VCC) between excited and ground-state helium atoms. Such collisions limit the amount of time an atom in a particular Doppler group interacts with the laser before either moving

to a different velocity class, or being removed from the region of laser interaction altogether. Velocity-changing collisions lead to a broad Gaussian background, upon which the narrow Lorentzian transition resonances sit, and this feature is included in the fits to the experimental line shapes.

The measured intervals, derived from differences in transition frequencies, are also affected by magnetic field shifts, gas-pressure shifts, and light-pressure shifts. The linear Zeeman shifts cancel out, while theoretical corrections for the much-smaller nonlinear Zeeman shifts are explicitly calculated and applied. The pressure shifts are due to perturbations to the internal energy levels of the atoms, and are proportional to the gas pressure.

Light-pressure shifts refer to the recoil effect of photon scattering on the helium atoms, which alters the velocity distribution of the atoms in the cloud. The shift is proportional to the average number of photons absorbed by an atom before being optically-pumped to a dark state, which varies for the different 2^3S -to- 2^3P_J transitions. These light-pressure shifts are measured and compensated for in the experiment, except in the case of the 2^3P_1 — 2^3P_2 interval, for which the light-pressure shifts cancel. Due to the difficulty of properly modeling the light-pressure shifts, this chapter's analysis of interference effects focuses on the 2^3P_1 — 2^3P_2 splitting.

5.2 Theoretical Description

To model the saturated-absorption technique of [15], one should consider a laser with angular frequency $\omega=2\pi f$ and linear polarization \hat{z} interacting with a cloud of metastable helium atoms. The forward beam and the counter-propagating beam travel in the $+\hat{y}$ and $-\hat{y}$ directions, respectively, and both laser beams have a uniform intensity I_0 over the volume of atoms that contribute to the signal. An atom with velocity component v_y sees equal and opposite Doppler shifts $\pm\Delta\omega_D=\pm2\pi\Delta f_D=\pm\omega v_y/c$ for the two laser beams, and experiences a total electric field (in the dipole approximation) of

$$\vec{E}(t) = \hat{z}E_0 \cos [(\omega + \Delta\omega_D)t] + s\hat{z}E_0 \cos [(\omega - \Delta\omega_D)t + \Delta\phi]. \quad (5.1)$$

As before, $E_0=\sqrt{\frac{2I_0}{\epsilon_0 c}}$, and $\Delta\phi$ is the phase difference between the two laser beams. The parameter $s = 1$ or 0 indicates if the counter-propagating laser beam is switched on or off. The lack of a Gaussian laser envelope is justified, as the absorption is detected from a narrow region at the center of the laser beam, where the spatial intensity profile is essentially flat.

The measurement of the $2^3S_{1,m_J=1}$ -to- $2^3P_{1,m_J=1}$ transition is considered first. The reduced density-matrix equations for the four-level atom developed in Chapter 2 are applied, as these Eqs. (2.11) describe the transfer of population in the system of Fig. 5.1 where the laser is nearly resonant with the $|1\rangle \rightarrow |2\rangle$ transition. They involve only the initial state $|1\rangle$ and the on-resonant state $|2\rangle$, but include

first-order corrections due to the presence of the distant state $|3\rangle$:

$$\dot{\rho}_{11} = \left(\frac{i\Omega_2^*}{2} + \frac{\Omega_3^* \gamma_{23 \rightarrow 1}}{2\omega_{23}} \right) \rho_{12} + \gamma_{2 \rightarrow 1} \rho_{22} - \left(\frac{i\Omega_2}{2} - \frac{\Omega_3 \gamma_{23 \rightarrow 1}}{2\omega_{23}} \right) \rho_{12}^*, \quad (5.2a)$$

$$\dot{\rho}_{12} = \frac{i\Omega_2}{2} \rho_{11} - \frac{i\Omega_2}{2} \rho_{22} - \left[\frac{\gamma_2}{2} + i \left(\Delta_2 + \frac{|\Omega_3|^2}{4\omega_{23}} \right) \right] \rho_{12}, \quad (5.2b)$$

$$\dot{\rho}_{22} = \frac{i\Omega_2}{2} \rho_{12}^* - \frac{i\Omega_2^*}{2} \rho_{12} - \gamma_2 \rho_{22}. \quad (5.2c)$$

Here ω_{23} is the fine-structure splitting between $|2\rangle$ and $|3\rangle$ of Fig. 5.1, while $\Delta_2 = 2\pi \Delta f$ is the detuning of the laser from the $|1\rangle \rightarrow |2\rangle$ transition frequency. The radiative decay terms involve the quantities $\gamma_2 = \gamma$, $\gamma_{2 \rightarrow 1} = \gamma/2$, and $\gamma_{23 \rightarrow 1} = \gamma/2$, where $\gamma = 1/\tau$ and $\tau = 98$ ns is the lifetime of the 2^3P_J states. The γ_{23} terms in Eqs. (2.11) vanish since $\gamma_{23} = \gamma_{23 \rightarrow 0} + \gamma_{23 \rightarrow 1} = 0$.

Invoking once again the rotating-wave approximation, the Rabi frequencies Ω_2 and Ω_3 associated with the driven transitions between the metastable state $|1\rangle$ and the two excited states $|2\rangle$ and $|3\rangle$ can be written as:

$$\Omega_i(t) = \Omega_i^{(+)} + s\Omega_i^{(-)}, \quad (5.3a)$$

$$\Omega_i^{(+)} = e^{i\Delta\omega_D t} \frac{eE_0}{\hbar} \langle 1|z|i\rangle, \quad (5.3b)$$

$$\Omega_i^{(-)} = e^{-i(\Delta\omega_D t + \Delta\phi)} \frac{eE_0}{\hbar} \langle 1|z|i\rangle. \quad (5.3c)$$

The (+) and (−) superscripts refer to the forward and backward beams, and, as in Eq. (5.1), the value of s indicates whether the counter-propagating beam is

switched on or off.

5.3 Absorption Lineshapes

The net absorption from the laser field during the atom-laser interaction time T can be calculated by integrating the atom-field driving terms in the excited-state population rates $\dot{\rho}_{22}$ and $\dot{\rho}_{33}$ of Eqs. (2.3) (b),(c), which describe the full four-level system:

$$\alpha_s = \frac{i}{2} \int_0^T \left(\Omega_2^{(+)} \rho_{21} - \Omega_2^{*(+)} \rho_{12} + \Omega_3^{(+)} \rho_{31} - \Omega_3^{*(+)} \rho_{13} \right) dt \quad (5.4)$$

Note that only partial Rabi-frequencies, $\Omega_2^{(+)}$ and $\Omega_3^{(+)}$ (c.f. Eq. (5.3)(b)), appear in the above expression, i.e., only the coupling to the forward laser beam is used. The absorption still depends on the parameter s , as indicated by the subscript, since the density-matrix elements ρ_{12} and ρ_{13} can be calculated either using a single forward laser beam ($s = 0$) or with a reflected backward beam included ($s = 1$).

The same procedure used to derive Eqs. (5.2) can be applied to Eq. (5.4), in order to obtain a reduced expression for the absorption rate compatible with the reduced Eqs. (5.2), as follows:

1. Define the usual ordering parameter $\eta \sim \frac{\Omega_i}{\omega_{23}}, \frac{\gamma_i}{\omega_{23}} \ll 1$, i.e., the ratio of the two frequency scales in the system, where the fine-structure splitting frequency $\omega_{23} \gg \Omega_i, \gamma_i, \Delta_i$ (the Rabi frequencies, decay rates and laser detuning) and start

with expressions from the full four-level Eqs (2.3), dropping terms of $\mathcal{O}(\eta^2)$:

$$\dot{\alpha} = \frac{i}{2}\Omega_2\rho_{21} - \frac{i}{2}\Omega_2^*\rho_{12} + \frac{i}{2}\Omega_3\rho_{31} - \frac{i}{2}\Omega_3^*\rho_{13}, \quad (5.5a)$$

$$\dot{\rho}_{13} = \left(-i\Delta_3 - \frac{\gamma_3}{2}\right)\rho_{13} + \frac{i}{2}\Omega_3\rho_{11} - \frac{i}{2}\Omega_2\rho_{23} - \frac{i}{2}\Omega_3\rho_{33}, \quad (5.5b)$$

$$\dot{\rho}_{31} = \left(i\Delta_3 - \frac{\gamma_3}{2}\right)\rho_{31} - \frac{i}{2}\Omega_3^*\rho_{11} + \frac{i}{2}\Omega_2^*\rho_{32} + \frac{i}{2}\Omega_3^*\rho_{33}, \quad (5.5c)$$

where $\Delta_3 = \Delta_2 + \omega_{23}$.

2. Form a linear combination of Eqs. (5.5) to eliminate ρ_{13} and ρ_{31} from the

absorption equation: (a) + (b) $\left[\frac{i}{2}\Omega_3^*\frac{1}{(-i\Delta_3 - \frac{1}{2}\gamma_3)}\right]$ + (c) $\left[-\frac{i}{2}\Omega_3\frac{1}{(i\Delta_3 - \frac{1}{2}\gamma_3)}\right]$.

3. This linear combination leads to a left-hand side of

$$\begin{aligned} LHS &= \dot{\alpha} + \frac{i}{2}\frac{\Omega_3^*}{(-i\Delta_3 - \frac{1}{2}\gamma_3)}\dot{\rho}_{13} - \frac{i}{2}\frac{\Omega_3}{(i\Delta_3 - \frac{1}{2}\gamma_3)}\dot{\rho}_{31} \\ &= \dot{\alpha} + \mathcal{O}(\eta^2), \end{aligned}$$

and a right-hand side of

$$\begin{aligned}
RHS &= \frac{i}{2}\Omega_2\rho_{21} - \frac{i}{2}\Omega_2^*\rho_{12} + \frac{i}{2}\Omega_3\rho_{31} - \frac{i}{2}\Omega_3^*\rho_{13} \\
&+ \frac{i}{2}\Omega_3^*\frac{(-i\Delta_3 - \frac{1}{2}\gamma_3)}{(-i\Delta_3 - \frac{1}{2}\gamma_3)}\rho_{13} + \frac{\frac{i}{2}\Omega_3\frac{i}{2}\Omega_3^*}{(-i\Delta_3 - \frac{1}{2}\gamma_3)}\rho_{11} - \frac{\frac{i}{2}\Omega_3\frac{i}{2}\Omega_2^*}{(-i\Delta_3 - \frac{1}{2}\gamma_3)}\rho_{23} - \frac{\frac{i}{2}\Omega_3\frac{i}{2}\Omega_3^*}{(-i\Delta_3 - \frac{1}{2}\gamma_3)}\rho_{33} \\
&- \frac{i}{2}\Omega_3\frac{(i\Delta_3 - \frac{1}{2}\gamma_3)}{(i\Delta_3 - \frac{1}{2}\gamma_3)}\rho_{31} + \frac{\frac{i}{2}\Omega_3^*\frac{i}{2}\Omega_3}{(i\Delta_3 - \frac{1}{2}\gamma_3)}\rho_{11} - \frac{\frac{i}{2}\Omega_3^*\frac{i}{2}\Omega_2}{(i\Delta_3 - \frac{1}{2}\gamma_3)}\rho_{32} - \frac{\frac{i}{2}\Omega_3^*\frac{i}{2}\Omega_3}{(i\Delta_3 - \frac{1}{2}\gamma_3)}\rho_{33} \\
&= \frac{i}{2}\Omega_2\rho_{21} - \frac{i}{2}\Omega_2^*\rho_{12} - \frac{1}{4}\frac{|\Omega_3|^2}{(-i\Delta_3 - \frac{1}{2}\gamma_3)}\rho_{11} - \frac{1}{4}\frac{|\Omega_3|^2}{(i\Delta_3 - \frac{1}{2}\gamma_3)}\rho_{11} + \mathcal{O}(\eta^2) \\
&= \frac{i}{2}\Omega_2\rho_{21} - \frac{i}{2}\Omega_2^*\rho_{12} - \frac{1}{4}|\Omega_3|^2\frac{i\Delta_3 - \frac{\gamma_3}{2} - i\Delta_3 - \frac{\gamma_3}{2}}{(-i\Delta_3 - \frac{\gamma_3}{2})(i\Delta_3 - \frac{\gamma_3}{2})}\rho_{11} \\
&= \frac{i}{2}\Omega_2\rho_{21} - \frac{i}{2}\Omega_2^*\rho_{12} + \frac{1}{4}|\Omega_3|^2\frac{\gamma_3}{(\Delta_3^2 - \frac{\gamma_3^2}{4})}\rho_{11} \\
&= \frac{i}{2}\Omega_2\rho_{21} - \frac{i}{2}\Omega_2^*\rho_{12} + \mathcal{O}(\eta^2)
\end{aligned}$$

The reduced expression for the absorption therefore does not contain any first-order corrections, and is simply that naively obtained from Eqs. (5.2):

$$\alpha_s = \frac{i}{2} \int_0^T \left(\Omega_2^{(+)} \rho_{12}^* - \Omega_2^{*(+)} \rho_{12} \right) dt. \quad (5.6)$$

This integral, when combined with ρ_{12} obtained by integrating Eqs. (5.2), is complete to order η . Numerical integration of Eqs. (5.2) and (5.6) must be done twice: with $s=0$ (a single forward beam) and with $s=1$ (including the counter-propagating beam).

The total absorption α_0 and α_1 is computed over a range of frequencies near resonance to obtain saturated-absorption line shapes. Such line shapes are calculated for a large set of Doppler groups ($\Delta\omega_D$ of Eq. (5.1)), as well as relative phases in the

two-beam case ($\Delta\phi$ of Eq. (5.1)). Absorption profiles $\bar{\alpha}_0$ and $\bar{\alpha}_1$ are then obtained by averaging over these parameters, and the difference $\overline{\Delta\alpha} = \bar{\alpha}_0 - \bar{\alpha}_1$ is taken as the saturated-absorption signal, from which width and line center parameters are derived. An example of this is shown in Fig. 5.2.

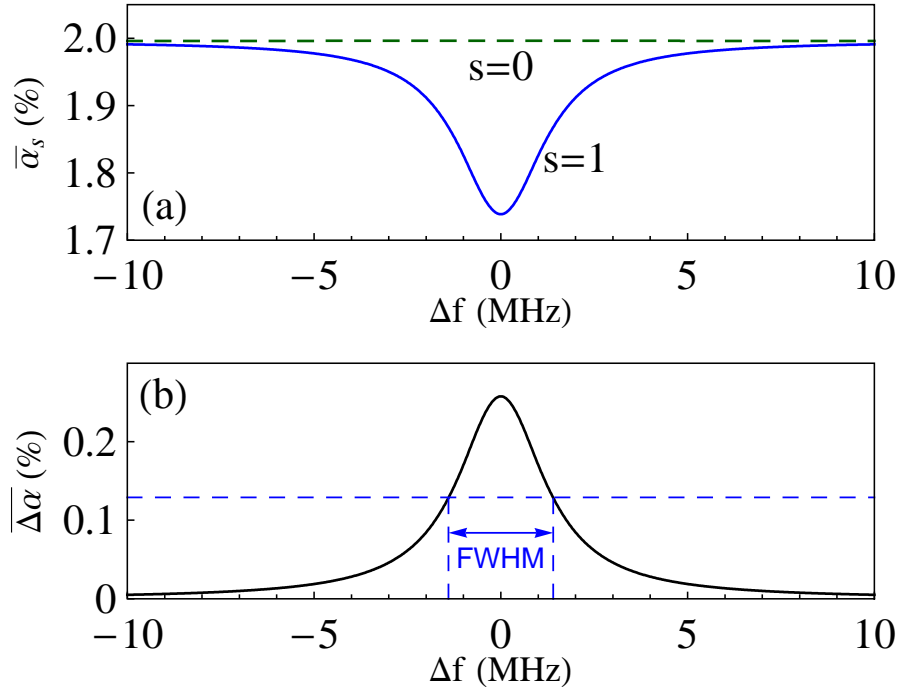


Figure 5.2: Phase- and Doppler-averaged saturated-absorption line shape of the 2^3S_1 -to- 2^3P_1 resonance, for a laser intensity of $I=0.1 \text{ mW/cm}^2$ and interaction time of $T=1 \text{ }\mu\text{s}$. Single-beam ($s = 0$) and two-beam ($s = 1$) absorption profiles are shown at the top (a), with the difference in absorption at the bottom (b). The points defining the FWHM of the line shape (in this case 2.8 MHz) are indicated.

While the thermal atomic cloud used in the experiment has a Gaussian velocity distribution with a Doppler-width on the order of 1000 MHz, the calculation of the saturated-absorption line shapes only averages over a narrow range of Doppler

groups ($|\Delta\omega_D| \leq 2\pi \cdot 80$ MHz) since it can be shown that the other Doppler groups make no significant contribution. A uniform velocity distribution is used since the cloud's broad velocity profile is almost constant over this range of Doppler groups.

The half-maximum points (see Fig. 5.2) are then used to determine the shift.

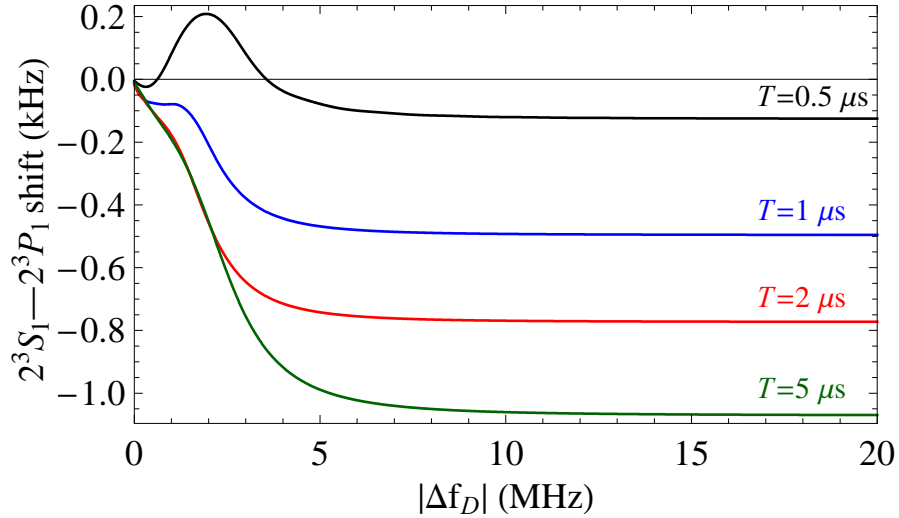


Figure 5.3: Shifts in the 2^3S_1 -to- 2^3P_1 resonance as a function of included Doppler groups. The line shapes are calculated using uniformly-distributed Doppler groups ranging from $-|\Delta f_D|$ to $|\Delta f_D|$. Results are shown for a laser intensity of 0.1 mW/cm², with four choices of atom-laser interaction time T .

The simplification of only including a limited range of Doppler groups can be justified by referring to Fig. 5.3. The value of the shift is seen to depend on the number of Doppler groups that are included in the calculation, but has already converged (to a 10 Hz level of precision) when all Doppler groups with $|\Delta f_D| < 20$ MHz are included. The rapid convergence illustrates how the signal is dominated by atoms that are nearly at rest, a tiny, essentially flat region of the velocity distri-

bution. A similar convergence of the resonance line widths is seen in Fig. 5.4, and the $|\Delta f_D| < 80$ MHz range is sufficient to cover even the largest widths encountered in the calculations.

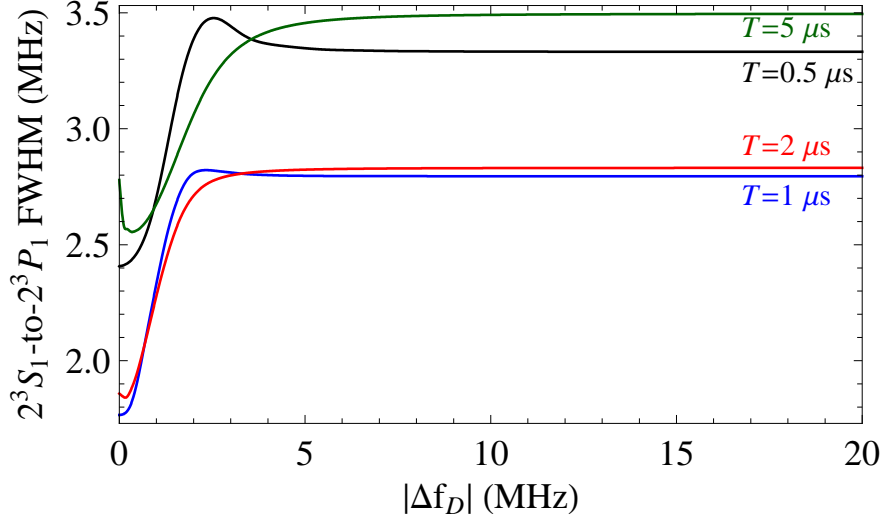


Figure 5.4: Widths of the 2^3S_1 -to- 2^3P_1 resonance as a function of included Doppler groups. The line shapes are calculated using uniformly-distributed Doppler groups ranging from $-|\Delta f_D|$ to $|\Delta f_D|$. Results are shown for a laser intensity of 0.1 mW/cm^2 , with four choices of atom-laser interaction time T .

The preceding treatment involved the $2^3S_{1,m_J=1}$ -to- $2^3P_{1,m_J=1}$ transition, but identical shifts are obtained when considering the $m_J=-1$ transition.

A similar analysis can be carried out for a laser nearly resonant with the 2^3S_1 -to- 2^3P_2 transition instead. As discussed earlier, this scenario is still amenable to the four-level model, since the large magnetic field in the experiment [15] separates the m_J levels sufficiently to suppress the transition out of the $|0\rangle$ state in Fig. 5.1 once the atom has decayed to that level.

Every part of the calculation is the same, except for a sign difference due to the fact that the on-resonance process is now at a lower frequency than the off-resonant 2^3S_1 -to- 2^3P_1 transition, i.e., $\omega_{32} = -\omega_{23}$. This alternate case results in shifts in the resonance of equal magnitude but opposite sign. Since the 2^3P_1 — 2^3P_2 fine-structure interval is determined by subtracting the observed line centers for the 2^3S_1 -to- 2^3P_1 and 2^3S_1 -to- 2^3P_2 resonances, the net shift in the interval is thus twice the individual shift for 2^3S_1 -to- 2^3P_1 .

5.4 Interference Shifts

Saturated-absorption line shapes are calculated for a wide range of atom-laser interaction times T and for a number of laser intensities I , including the value of $I=0.1$ mW/cm² used in the measurements of Ref. [15]. Figure 5.5 shows the FWHM of the 2^3S_1 -to- 2^3P_1 resonance (solid lines) as a function of laser intensity I and interaction time T (top axis). The feature is broadened both at short interaction times ($T \ll 2\pi\tau$) and above saturation ($\Omega_2 T \gg 1$), but can approach the natural width (dashed line) for sufficiently-long T and low enough I .

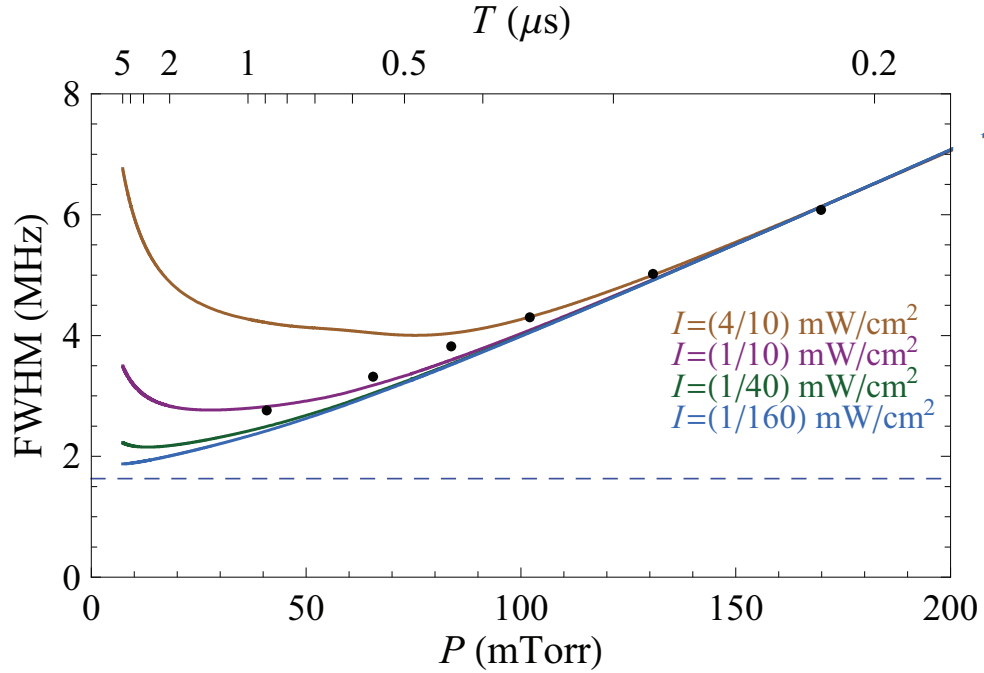


Figure 5.5: Widths of the calculated saturated-absorption line shapes (solid lines) for the 2^3S_1 -to- 2^3P_1 resonance, over a range of interaction times T , and for various laser intensities I . The data points are experimental widths from [48], which are used to calibrate the pressure scale (bottom axis) with the time scale (top axis). The natural width of the resonance is shown as a dashed line.

The experiment of Ref. [15] varied the gas pressure in the cell and extrapolated the measured fine-structure intervals down to zero pressure, to correct for the systematic effect of velocity-changing collisions, and other pressure-dependent effects.

These collisions, between $n=2$ helium atoms in the discharge and the much larger number of ground-state atoms in the cell, determine the interaction time T . The rate of the collisions limits the average amount of time an atom in a particular Doppler group interacts with the laser and contributes to the saturated-absorption

signal, before moving to a different velocity class, or being removed from the region of laser interaction altogether.

To connect the model calculations with experiment [15], a correspondence can be made between the atom-laser interaction time T and the reciprocal of the pressure in the cell, $T \propto 1/P$, as higher gas pressures result in larger collision rates and shorter interaction times. The constant of proportionality is found by matching the calculated line widths-vs.-time to measured [48] widths-vs.-pressure (the points in Fig. 5.5) at a laser intensity of $I=0.1$ mW/cm². This calibrates the time-pressure scale and allows extrapolation of calculated shifts to zero pressure. The corresponding shifts in the fine-structure interval are shown in Fig. 5.6 using thin solid curves, with interaction time T also calibrated to the experimental widths.

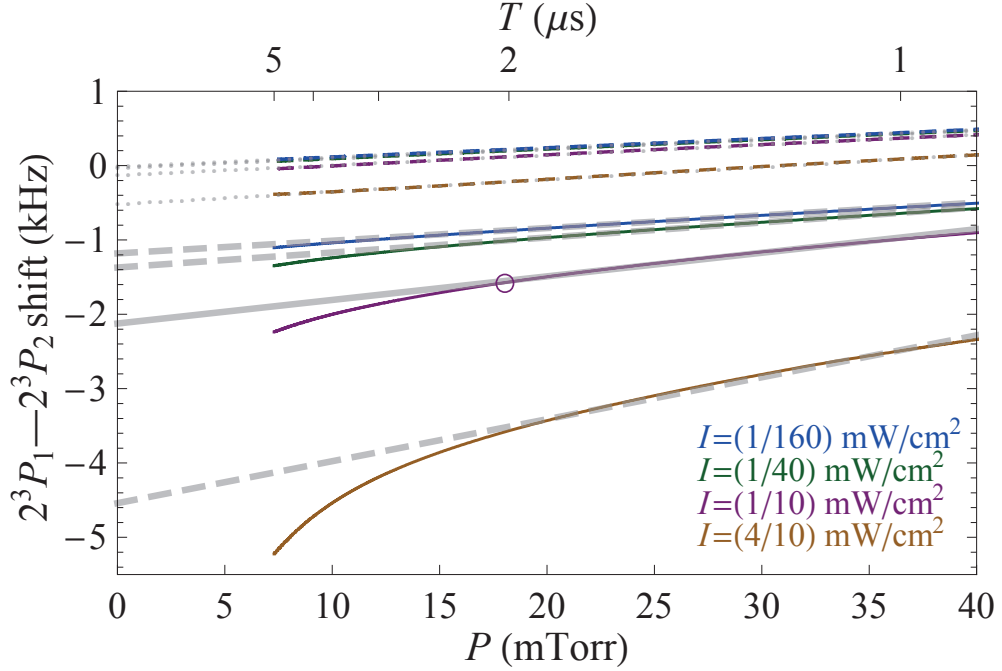


Figure 5.6: Total shifts (solid thin lines) in the $2^3P_1—2^3P_2$ interval over a range of interaction times T (which correspond to helium cell pressures P) and laser intensities I . The thin dashed lines give the effect when only the AC-Stark shift term is included. The thick lines show least-squares fits of the shifts over the pressure range of 18 to 38 mTorr, extrapolated to zero pressure. The circle indicates the intensity and pressure at which the most significant data in [15] were taken.

5.5 Correction to the $2^3P_1—2^3P_2$ Interval

For the measurement in [15], the most precise data were taken at helium cell pressures between 18 and 38 mTorr, and were then extrapolated to zero pressure. In Fig. 5.5 this range of pressures yields the smallest line widths at the nominal intensity of $I=0.1$ mW/cm², minimizing the interference with the neighboring resonance that would result from the larger widths at lower pressures (larger T).

In this pressure range, the corresponding interference shifts in Fig. 5.6 (thin solid lines) have a linear dependence on P , avoiding the larger shifts that grow nonlinearly at lower pressures. The thick gray lines in Fig. 5.6 show extrapolations of the calculated shifts from linear fits to this range.

AC-Stark-only shifts (thin dashed lines in Fig. 5.6) are also computed, by artificially suppressing the $\frac{\Omega_3 \gamma_{23 \rightarrow 1}}{2\omega_{23}}$ interference term in Eqs. (5.2). These curves represent the effect of the $\frac{|\Omega_3|^2}{4\omega_{23}}$ term alone, and the shifts vanish when extrapolated to zero pressure, and as the laser intensity approaches zero, as indicated by the dotted gray lines.

In contrast, extrapolation to $P=0$ of the full interference shifts leads to residual values, even in the limit of zero laser intensity I . Thus, a repetition of experiments down to lower pressures and laser intensities will not eliminate the interference shift. As shown by the thick dashed line on the lowest-intensity curve, the interference shift in the limit of zero pressure and intensity is -1.2 kHz, which exceeds the 0.51-kHz uncertainty of the saturated-absorption measurement of this interval, and thus a correction of $+1.2$ kHz to the measured value from [15] must be applied.

The net -1.2 kHz shift can be broken up into three parts. The shift at 18 mTorr and 0.1 mW/cm² is -1.6 kHz (this is the pressure and intensity at which the most precise data were taken in [15], as indicated by the circle in Fig. 5.6). The extrapolation to zero pressure (the thick solid line) causes an additional shift of -0.6 kHz. Finally, an extrapolation of the $P=0$ intercepts of Fig. 5.6 to zero

intensity causes an additional shift of +1.0 kHz.

The extrapolations of the calculated shifts to $P=0$ and $I=0$ are subject to some uncertainty. For example, an atom in a helium cell at a pressure P would experience a range of times T between velocity-changing collisions (ranging from approximately 50% to 150% of the average T), and therefore the correspondence between T and P assumed in Fig. 5.6 is only approximate. Furthermore, the current model does not explicitly include magnetic fields, and the degree to which state $|0\rangle$ of Fig. 5.1 is a dark state might depend on magnetic field, on laser intensity, and on the pressure in the cell. Because of these unknowns, a 50% uncertainty is assumed for each component of the shift, to arrive at an estimate of the total shift of $(-1.6 \pm 0.8 \text{ kHz}) + (-0.6 \pm 0.3 \text{ kHz}) + (+1.0 \pm 0.5 \text{ kHz}) = -1.2 \pm 1.0 \text{ kHz}$ for this measurement.

6 Microwave Spectroscopy

The discussion of precision helium fine-structure measurements has so far examined methods based on laser spectroscopy, where helium atoms are initially in the 2^3S metastable states. By driving 1083-nm transitions from these states to the excited $2^3P_{J=0,1,2}$ levels, the fine-structure splittings were determined from the difference between the resonance line centers of any pair of these transitions.

A more direct measurement of the fine-structure intervals can be made by using a microwave field to drive magnetic-dipole transitions between the 2^3P states themselves. Experiments performed with single microwave pulses have obtained values of $2,291,174.0 \pm 1.4$ kHz for the 2^3P_1 — 2^3P_2 interval [12] and $29,616,950.9 \pm 0.9$ kHz for the 2^3P_0 — 2^3P_1 interval [13], respectively.

A subsequent experiment [16] using the Ramsey method of separated oscillatory-fields obtained a more precise measurement of the 2^3P_1 — 2^3P_2 interval, with a value of $2,291,177.53 \pm 0.35$ kHz.

Calculations of the interference effect associated with these types of measurements result in shifts that are much smaller than the experimental uncertainty [42],

which underscores the technique’s robustness against this systematic effect. However, the interference effects will be of importance for the next generation of higher-precision microwave measurements.

6.1 Measurement Technique

Using the experimental technique of [10, 12, 13, 16] one prepares a beam of thermal He atoms using a series of optical pumping lasers, so that the $2^3P_1, m_J=0$ excited state is populated while the $2^3S_1, m_J=0$ metastable state is vacant. An atom in $2^3P_1, m_J=0$ is forbidden by electric-dipole selection rules from decaying to $2^3S_1, m_J=0$, so this latter state can only accumulate population if an applied microwave field drives transitions to either the $2^3P_0, m_J=0$, or one of the $2^3P_2, m_J=0, \pm 1$ states, which can subsequently decay down to $2^3S_1, m_J=0$.

The relevant triplet states are illustrated in Fig. 6.1, where a linearly-polarized microwave field that is nearly resonant with the $|1\rangle \rightarrow |2\rangle$ transition drives population out of $2^3P_1, m_J=0$ ($|1\rangle$) to the $2^3P_2, m_J=0$ state ($|2\rangle$), as shown by the solid arrow. To maximize the signal, the field is applied before any significant portion of the initial population in $|1\rangle$ has had a chance to decay back to the metastable states.

The field also drives the far-off-resonance $|1\rangle \rightarrow |0\rangle$ transition, transferring a small amount of population to $2^3P_0, m_J=0$ ($|0\rangle$), indicated by the dotted arrow.

Atoms in either state $|1\rangle$ or $|0\rangle$ then spontaneously decay to the metastable states $2^3S_1, m_J = -1, 0, +1$ (denoted in Fig. 6.1 by $|a\rangle$, $|b\rangle$, and $|c\rangle$ respectively).

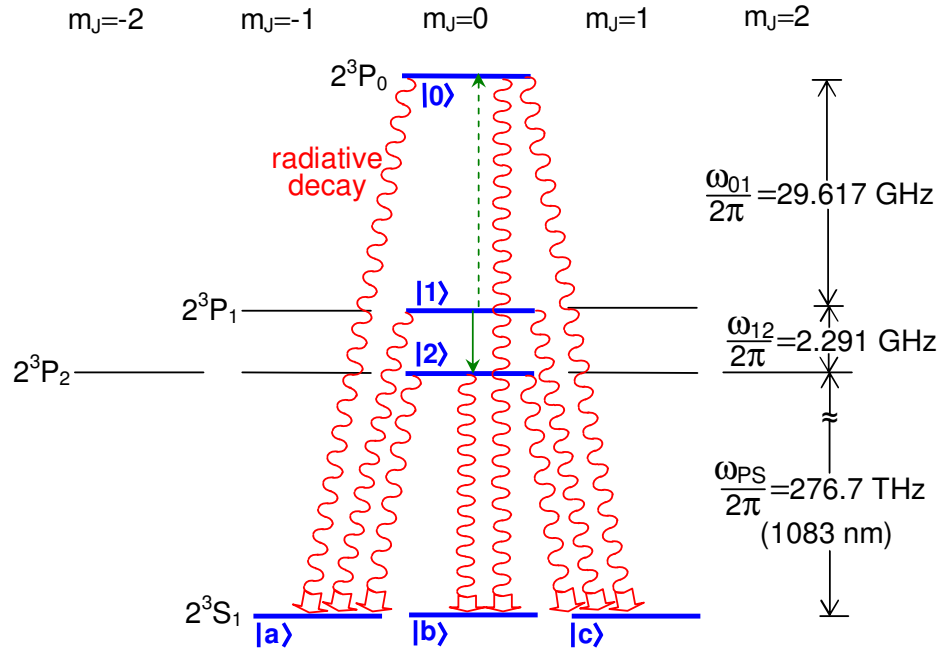


Figure 6.1: A direct microwave measurement of the He fine-structure intervals. The population starts in the $|1\rangle$ state, and an applied microwave field either drives the $|1\rangle \rightarrow |2\rangle$ transition (solid arrow) or the $|1\rangle \rightarrow |0\rangle$ transition (dashed arrow). The allowed radiative decay paths from states $|1\rangle$, $|2\rangle$ and $|0\rangle$ are indicated.

The atoms in $|b\rangle$ are then laser-excited back to $|0\rangle$, and the resulting fluorescence from radiative decay is measured to obtain the signal, which is directly proportional to the population of the $|b\rangle$ state after the beam has passed through the microwave field.

The applied field can be resonant with the $|1\rangle \rightarrow |0\rangle$ transition instead, and then $|1\rangle \rightarrow |2\rangle$ becomes the distant resonance. In either case there are two excitation-

and-decay processes, 27.3 GHz out of resonance from each other, that start in state $|1\rangle$ and end up in the final state $|b\rangle$. Quantum-mechanical interference between these pathways distorts the line shape of the probed resonance and manifests itself as a shift in the measured line center.

The measurement of the 2^3P intervals can be done either with a single pulse of microwaves, or by using the Ramsey method of separated oscillatory fields (SOF), in which the atoms interact with two microwave pulses separated in time. The two pulses are either in phase with each other, or 180° out-of-phase, and the SOF line shape is obtained by subtracting the out-of-phase signal from that obtained using in-phase pulses. The SOF method is more precise, resulting in line shapes that are narrower than the 3.2 MHz natural width of the magnetic-dipole microwave resonances. The natural width is double that seen for the laser transitions, since both the initial and final states are unstable.

6.2 Theoretical Description

The transitions $|1\rangle \rightarrow |0\rangle$ and $|1\rangle \rightarrow |2\rangle$ among the $2^3P_{J,m_J=0}$ states are due to the comparatively weak magnetic-dipole atom-field coupling, which is given in the dipole approximation as:

$$U(t) = -\vec{\mu} \cdot \vec{B}(t) = -\mu_B/\hbar B_0 g(t) \cos(\omega t + \phi)(\hat{L}_z + 2\hat{S}_z), \quad (6.1)$$

for a linearly-polarized field $\vec{B}(t) = \hat{z}B_0 g(t) \cos(\omega t + \phi)$.

The function $g(t)$ modulates the peak microwave field amplitude B_0 , and is equal to $g(t) = \sigma_D(t)$ for the single-pulse case shown in Fig. 6.2(a), where $\sigma_D(t)$ is a pulse of unit amplitude and FWHM duration D . Dual microwave pulses separated by a time interval T , are modeled by $g(t) = [\sigma_D(t) \pm \sigma_D(t - T)]$. The relative sign of the terms corresponds to the in-phase vs. out-of-phase pulses shown in Fig. 6.2(b) and (c), respectively.

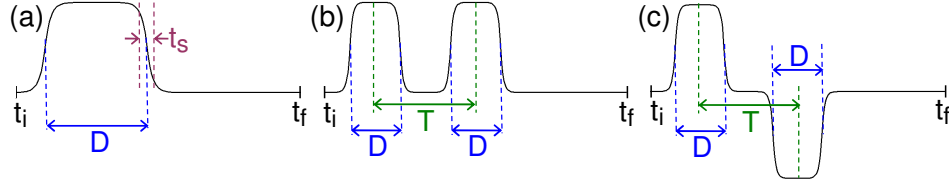


Figure 6.2: Timing for the microwave pulses. A single microwave pulse is depicted in (a), while the in-phase and 180°-out-of-phase cases for two pulses are represented in (b) and (c). A switching time of $t_s=1$ ns (cf. (a)) is included in the calculations.

As the applied microwave frequencies are of comparable size to the spacings between the excited states, the rotating-wave approximation is no longer applicable to this system, nor is it viable to use the reduction process employed in previous chapters to simplify the density-matrix equations.

A full set of density matrix equations involving the states $|1\rangle$, $|2\rangle$, $|0\rangle$, and $|b\rangle$

must therefore be used [42] (see also Appendix A):

$$\begin{aligned}\dot{\rho}_{11} &= i\Omega_{12}^*\rho_{12} - i\Omega_{12}\rho_{21} + i\Omega_{10}^*\rho_{10} - i\Omega_{10}\rho_{01} \\ &\quad - \gamma_1\rho_{11} - \frac{\gamma_{10}}{2}(\rho_{10} + \rho_{01}) - \frac{\gamma_{12}}{2}(\rho_{12} + \rho_{21}),\end{aligned}\tag{6.2a}$$

$$\begin{aligned}\dot{\rho}_{12} &= i\Omega_{12}(\rho_{11} - \rho_{22}) - i\Omega_{10}\rho_{02} - \left(\frac{\gamma_1 + \gamma_2}{2} - i\omega_{21}\right)\rho_{12} \\ &\quad - \frac{\gamma_{20}}{2}\rho_{10} - \frac{\gamma_{12}}{2}(\rho_{11} + \rho_{22}) - \frac{\gamma_{10}}{2}\rho_{02},\end{aligned}\tag{6.2b}$$

$$\dot{\rho}_{22} = i\Omega_{12}\rho_{21} - i\Omega_{12}^*\rho_{12} - \gamma_2\rho_{22} - \frac{\gamma_{20}}{2}(\rho_{20} + \rho_{02}) - \frac{\gamma_{12}}{2}(\rho_{21} + \rho_{12}),\tag{6.2c}$$

$$\begin{aligned}\dot{\rho}_{10} &= i\Omega_{10}(\rho_{11} - \rho_{00}) - i\Omega_{12}\rho_{20} - \left(\frac{\gamma_1 + \gamma_0}{2} - i\omega_{01}\right)\rho_{10} \\ &\quad - \frac{\gamma_{20}}{2}\rho_{12} - \frac{\gamma_{10}}{2}(\rho_{11} + \rho_{00}) - \frac{\gamma_{12}}{2}\rho_{20},\end{aligned}\tag{6.2d}$$

$$\begin{aligned}\dot{\rho}_{20} &= i\Omega_{10}\rho_{21} - i\Omega_{12}^*\rho_{10} - \left(\frac{\gamma_2 + \gamma_0}{2} - i\omega_{02}\right)\rho_{20} \\ &\quad - \frac{\gamma_{20}}{2}(\rho_{22} + \rho_{00}) - \frac{\gamma_{12}}{2}\rho_{10} - \frac{\gamma_{10}}{2}\rho_{21},\end{aligned}\tag{6.2e}$$

$$\dot{\rho}_{00} = i\Omega_{10}\rho_{01} - i\Omega_{10}^*\rho_{10} - \gamma_0\rho_{00} - \frac{\gamma_{20}}{2}(\rho_{02} + \rho_{20}) - \frac{\gamma_{10}}{2}(\rho_{01} + \rho_{10}),\tag{6.2f}$$

$$\begin{aligned}\dot{\rho}_{bb} &= \gamma_{1\rightarrow b}\rho_{11} + \gamma_{2\rightarrow b}\rho_{22} + \gamma_{0\rightarrow b}\rho_{00} + \gamma_{12\rightarrow b}(\rho_{21} + \rho_{12}) \\ &\quad + \gamma_{10\rightarrow b}(\rho_{01} + \rho_{10}) + \gamma_{20\rightarrow b}(\rho_{02} + \rho_{20}).\end{aligned}\tag{6.2g}$$

Here, $\Omega_{ij} = \langle i|U(t)|j\rangle/\hbar$ is the Rabi-frequency for the magnetic-dipole coupling between states $|i\rangle$ and $|j\rangle$, and the radiative decay rates $\gamma_1 = \tau_1^{-1}$, $\gamma_2 = \tau_2^{-1}$, and $\gamma_0 = \tau_0^{-1}$ are related to the lifetimes of states $|1\rangle$, $|2\rangle$, and $|0\rangle$. These total rates can be expressed as $\gamma_i = \gamma_{i\rightarrow a} + \gamma_{i\rightarrow b} + \gamma_{i\rightarrow c}$ in terms of the partial rates for the radiative decays shown in Fig. 6.1. Similarly, the cross-damping rates are defined

as $\gamma_{ij} = \gamma_{ij \rightarrow a} + \gamma_{ij \rightarrow b} + \gamma_{ij \rightarrow c}$, where (in the electric dipole approximation)

$$\gamma_{i \rightarrow b} = \frac{e^2 |\omega_{PS}|^3}{3\pi\epsilon_0 \hbar c^3} \langle i | \vec{r} | b \rangle \cdot \langle b | \vec{r} | i \rangle \quad (6.3a)$$

$$\gamma_{ij \rightarrow b} = \frac{e^2 |\omega_{PS}|^3}{3\pi\epsilon_0 \hbar c^3} \langle i | \vec{r} | b \rangle \cdot \langle b | \vec{r} | j \rangle. \quad (6.3b)$$

Solving Eqs. (6.2) for ρ_{11} , ρ_{22} , ρ_{00} , and ρ_{bb} , gives the populations of states $|1\rangle$, $|2\rangle$, $|0\rangle$, and $|b\rangle$, which are the only ones relevant to the measurement.

Density matrix equations for the quantities $\dot{\rho}_{ai}$, $\dot{\rho}_{bi}$, $\dot{\rho}_{ci}$ are not required, since they do not appear on the right-hand side of Eqs. (6.2), and therefore are decoupled from the rest of the system.

Since $\omega_{PS} \gg \omega_{12}, \omega_{01}$ (as shown in Fig. 6.1), $\gamma_1 = \gamma_2 = \gamma_0 = \gamma = 1/\tau$, where $\tau = 97.9$ ns. When computing the electric-dipole matrix elements, one obtains further cancellations and simplifications:

$$\gamma_{12} = \gamma_{10} = \gamma_{20} = 0, \quad (6.4a)$$

$$\gamma_{1 \rightarrow b} = \gamma_{12 \rightarrow b} = \gamma_{10 \rightarrow b} = 0, \quad (6.4b)$$

$$\gamma_{2 \rightarrow b} = 2\gamma/3, \quad (6.4c)$$

$$\gamma_{0 \rightarrow b} = \gamma/3, \quad (6.4d)$$

and

$$\gamma_{20 \rightarrow b} = -\sqrt{2}\gamma/3 \quad (6.4e)$$

The nonzero $\gamma_{20 \rightarrow b}$ term in Eqs. (6.2) represents the quantum-mechanical interfer-

ence in the radiative decay to the final measured state $|b\rangle$.

Computing the ratio of the magnetic-dipole matrix-elements gives $\Omega_{10} = \Omega_{01} = \Omega$ and $\Omega_{21} = \Omega_{12} = \Omega/\sqrt{2}$, where

$$\Omega(t) = \sqrt{\frac{2}{3}}(\mu_B/\hbar)B_0g(t)\cos(\omega t + \phi). \quad (6.5)$$

Substituting the results of Eqs. (6.4) and (6.5), Eqs. (6.2) simplify to

$$\dot{\rho}_{11} = \frac{i\Omega}{\sqrt{2}}(\rho_{12} - \rho_{21}) + i\Omega(\rho_{10} - \rho_{01}) - \gamma\rho_{11}, \quad (6.6a)$$

$$\dot{\rho}_{12} = \frac{i\Omega}{\sqrt{2}}(\rho_{11} - \rho_{22}) - (\gamma - i\omega_{21})\rho_{12} - i\Omega\rho_{02}, \quad (6.6b)$$

$$\dot{\rho}_{22} = \frac{i\Omega}{\sqrt{2}}(\rho_{21} - \rho_{12}) - \gamma\rho_{22}, \quad (6.6c)$$

$$\dot{\rho}_{10} = i\Omega(\rho_{11} - \rho_{00}) - \frac{i\Omega}{\sqrt{2}}\rho_{20} - (\gamma - i\omega_{01})\rho_{10}, \quad (6.6d)$$

$$\dot{\rho}_{20} = i\Omega\rho_{21} - \frac{i\Omega}{\sqrt{2}}\rho_{10} - (\gamma - i\omega_{02})\rho_{20}, \quad (6.6e)$$

$$\dot{\rho}_{00} = i\Omega(\rho_{01} - \rho_{10}) - \gamma\rho_{00}, \quad (6.6f)$$

$$\dot{\rho}_{bb} = \frac{2\gamma}{3}\rho_{22} + \frac{\gamma}{3}\rho_{00} - \frac{\sqrt{2}\gamma}{3}(\rho_{02} + \rho_{20}). \quad (6.6g)$$

Note that neither Eqs. (6.2) nor Eqs. (6.6) use the rotating-wave approximation and that $\Omega(t)$ in Eqs. (6.6) carries the full time dependence of the oscillating field. The equations also include both the resonant and off-resonance states.

Eqs. (6.6) are integrated numerically using a fourth-order Runge-Kutta method with initial conditions of $\rho_{11}(t_i) = 1$ and all other entries set to zero, to determine

the value of ρ_{bb} at $t = t_f$ of Fig. 6.2. This calculation follows the technique of [10, 12, 13, 16], where the atomic population is initially in state $|1\rangle$, and the final amount of population in $|b\rangle$ is a direct measure of the probability that a microwave transition has been made. Line shapes are generated by solving the equations for a range of applied frequencies $\omega = 2\pi f$ scanning around the resonance of interest, and the shifts caused by the distant neighboring resonance are then extracted.

The numerical solver uses a time step of 30 fs to accurately integrate through the approximately 30-GHz frequencies of the applied microwave field and the complex phase factor of the atomic wavefunction. The results are verified by using both higher-precision arithmetic and shorter time steps, and further checked by comparing to numerical integrations using an adaptive-step Runge-Kutta-Fehlberg method.

The integration is started at a time t_i that is 50 ns before the start of the first microwave pulse and continued until time t_f that is 500 ns after the end of the last pulse (see Fig. 6.2). This final 500 ns allows almost all of the 2^3P atoms to decay back down to the 2^3S states. As indicated in Fig. 6.2, the microwave pulses were chosen to have a time constant t_s for turn-on and turn-off. The shifts obtained are found to be essentially independent of t_s for values between 1 and 10 ns, which corresponds to experimentally realizable turn-on and turn-off times, and $t_s = 1$ ns is used for all integrations presented here. For much shorter t_s , the high frequencies associated with the sudden turn on and turn off modify the shifts by approximately

10%.

6.3 Single Microwave Pulse Shifts

Line shapes for both $|1\rangle \rightarrow |2\rangle$ and $|1\rangle \rightarrow |0\rangle$ transitions are obtained for a given pulse-width D and magnetic field amplitude B_0 by numerical solution of Eqs. (6.6) using the single-pulse timing envelope $g(t) = \sigma_D(t)$. A sample line shape can be seen in Fig. 6.3 for a pulse duration of $D = 200$ ns and magnetic field amplitude of $B_0 = 0.2$ gauss, and shows that the initially empty $|b\rangle$ state of Fig. 6.1 is populated when the microwave transition is driven. The calculation is repeated with the $\gamma_{20 \rightarrow b}$ interference term in Eqs. (6.2) artificially set to zero, so that only AC-Stark shifts affect the resonance profile in this type of simulation.

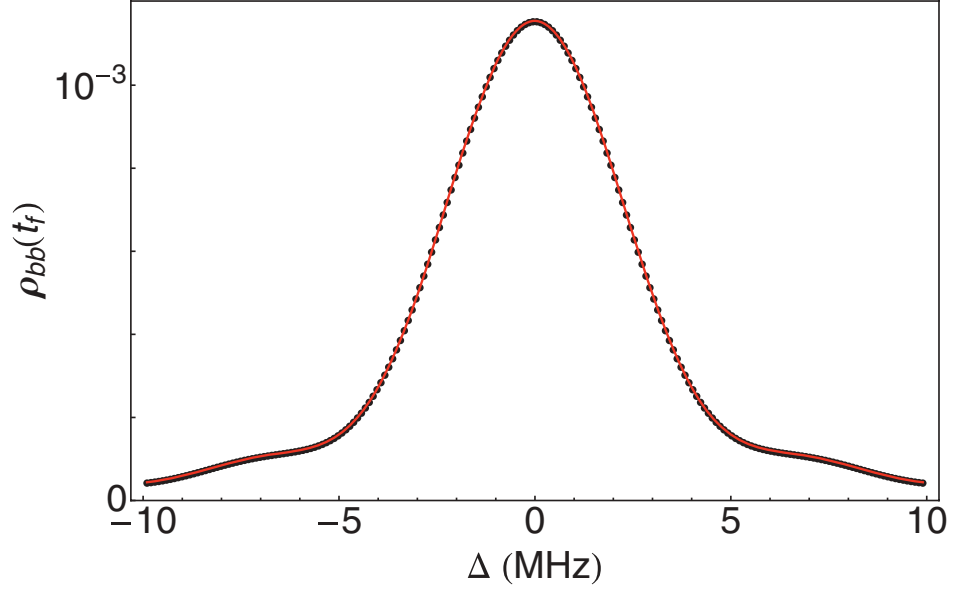


Figure 6.3: Line shape of the 2^3P_1 -to- 2^3P_2 ($|1\rangle \rightarrow |2\rangle$) resonance, obtained from numerical integrations using a single microwave pulse with a duration $D = 200$ ns and microwave magnetic field amplitude $B_0=0.2$ gauss. The fit (solid line) is obtained using Eq. (6.9)

To determine the shifts of the numerically-generated profiles, least-squares fits are made to an ideal line shape for a two-level atom interacting with a microwave field. This line shape can be obtained by evolving the atom's wavefunction (in the rotating-wave approximation) as it interacts with a square microwave pulse of duration D , to calculate the population in the final metastable $|b\rangle$ state. The expression is given by:

$$\rho_{bb}(\Delta) = \gamma_{i \rightarrow b} \int_{t=0}^D P_i(t) e^{-\gamma t} dt + \gamma_{i \rightarrow b} P_i(D) \int_{t=D}^{\infty} e^{-\gamma t} dt, \quad (6.7)$$

with

$$P_i(t) = \frac{\Omega_i^2 \sin^2(\sqrt{\Omega_i^2 + \Delta^2}t/2)}{\Omega_i^2 + \Delta^2} \quad (6.8)$$

being the probability of the atom being in the 2^3P_2 or 2^3P_0 state at time t ($i = 2, 0$, respectively). Here $\Delta = (\omega - \omega_0)$ is the detuning of the applied field from the resonant frequency, and $\gamma_{i \rightarrow b}$ is the rate of decay from state $|2\rangle$ (or $|0\rangle$) to state $|b\rangle$. $\Omega_2 = \sqrt{\frac{1}{3}}(\mu_B/\hbar)B_0$ and $\Omega_0 = \sqrt{\frac{2}{3}}(\mu_B/\hbar)B_0$ are the Rabi frequencies for the coupling of the $|2\rangle, |0\rangle$ excited states to the initial state $|1\rangle$.

The first term in Eq. (6.7) integrates over the period when the microwave pulse is on, and the population $P_i(t)$ in the $|2\rangle$ (or $|0\rangle$) state is undergoing Rabi oscillation between that state and the initial state $|1\rangle$, while simultaneously decaying to the $|b\rangle$ metastable state. The second term models the time after the atom has passed through the microwave field and evolves in a field-free manner, where the population $P_i(D)$ left in the $|2\rangle$ (or $|0\rangle$) state at time D simply decays to $|b\rangle$. During both intervals, population in $|b\rangle$ is accumulating at the partial rate $\gamma_{2 \rightarrow b}$ (or $\gamma_{0 \rightarrow b}$).

The fit function applied to the generated line shape is then taken to be

$$\tilde{\rho}_{bb}(\Delta; C, \Delta_0) = C\gamma_{i \rightarrow b}\Omega_i^2 \frac{\Omega_R - e^{-\gamma D} [\Omega_R \cos(\Omega_R D) + \gamma \sin(\Omega_R D)]}{2\gamma\Omega_R (\gamma^2 + \Omega_R^2)}, \quad (6.9)$$

where the integrals in Eq. (6.7) have been evaluated, and $\Omega_R^2 \equiv \Omega_i^2 + (\Delta - \Delta_0)^2$. The C and Δ_0 fit parameters are allowed to vary, with the latter's value representing the shift in the resonance line center.

As an alternative, the shifts may be determined based on the positions and slopes

at the half maximum points in Fig. 6.3. This approach leads to nearly identical values as those obtained by the fitting procedure, with very small differences due to the minute distortion in the line shape caused by the $\gamma_{20 \rightarrow b}$ interference term, which is not captured by the symmetric form of Eq. (6.9).

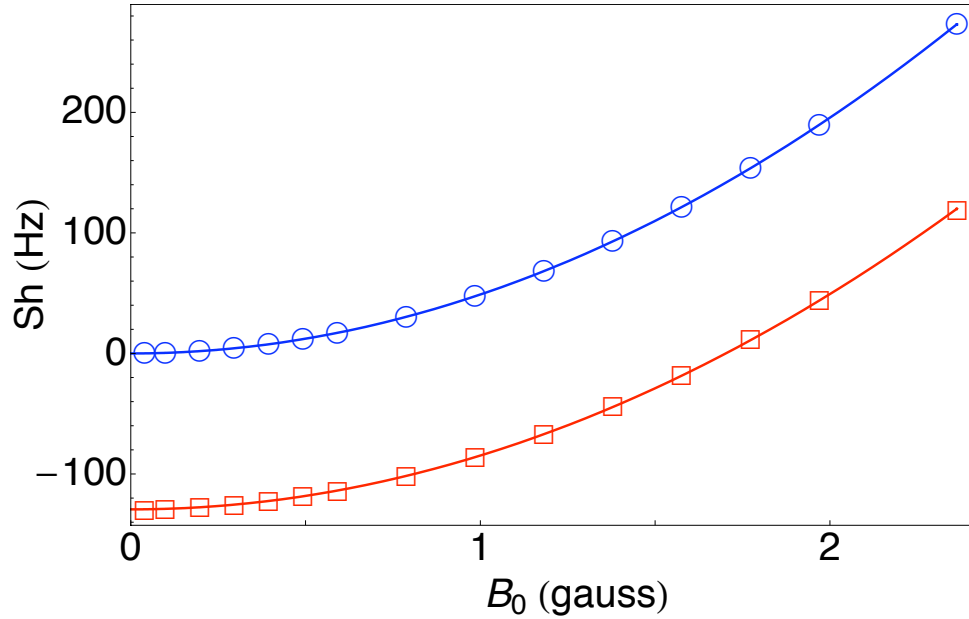


Figure 6.4: Shifts of the 2^3P_1 -to- 2^3P_2 resonance versus magnetic field amplitude, for a single microwave pulse with a duration $D = 200$ ns. The squares represent the full shifts, while circles are the AC-Stark shifts, which are obtained by artificially suppressing the $\gamma_{20 \rightarrow b}$ interference term in Eq. (6.2).

Shifts obtained by the fits are shown in Fig. 6.4 for a range of magnetic field amplitudes. The circles in the figure show the shifts that result when the $\gamma_{20 \rightarrow b}$ interference term in Eqs. (6.2) is excluded. These shifts scale as the square of the microwave field strength due to the expected AC-Stark power shifts, and extrapolate to zero for zero field intensity. The square symbols in the plots represent the full

Table 6.1: Frequency shifts extrapolated to zero microwave intensity using Eq. (6.10), for helium 2^3P_1 -to- 2^3P_0 ($|1\rangle \rightarrow |0\rangle$) and 2^3P_1 -to- 2^3P_2 ($|1\rangle \rightarrow |2\rangle$) single-microwave-pulse transitions.

D (ns)	$Sh^{(0)}$ (Hz)	
	$ 1\rangle \rightarrow 0\rangle$	$ 1\rangle \rightarrow 2\rangle$
50	-429	-429
100	-224	-224
200	-129	-129
400	-87	-88
800	-82	-82

shift, and these values do not extrapolate to zero, but rather have the quadratic form

$$Sh = Sh^{(0)} + kB_0^2, \quad (6.10)$$

where B_0 is the amplitude of the applied microwave field, k is the AC-Stark shift rate, and $Sh^{(0)}$ is the residual shift at zero intensity. These shifts $Sh^{(0)}$ are listed in Table 6.1 and are almost identical for the 2^3P_1 -to- 2^3P_0 and 2^3P_1 -to- 2^3P_2 intervals. Their magnitude is approximately inversely proportional to the pulse duration D .

6.4 Microwave SOF Shifts

Resonance profiles are also generated for Ramsey SOF measurements, which are obtained by solution of Eqs. (6.6) using the dual-pulse envelopes $g(t) = [\sigma_D(t) \pm \sigma_D(t - T)]$, for selected pulse width D and time separation T . The calculation is more involved, as both in-phase and out-of-phase cases must be computed, with the difference between the line shapes forming the SOF signal. An example is shown in

Fig. 6.5 for pulses of duration $D = 100$ ns, separated by $T = 500$ ns. The microwave magnetic field amplitude is $B_0=0.2$ gauss, and the graph again demonstrates that the initially empty $|b\rangle$ state of Fig. 6.1 is populated when the microwave transition is driven.

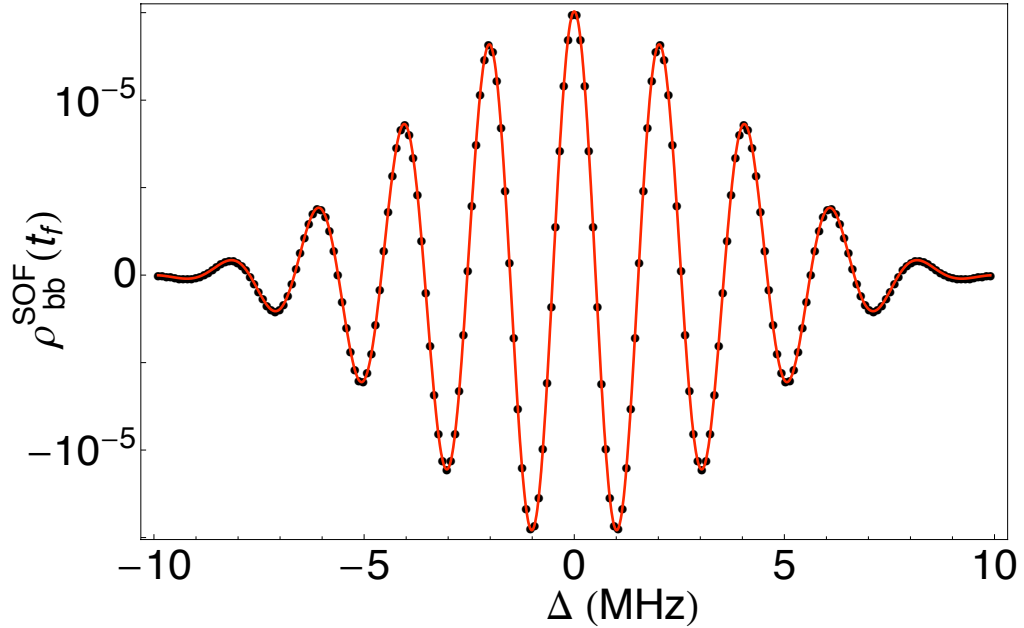


Figure 6.5: SOF line shape of the 2^3P_1 -to- 2^3P_2 resonance obtained from numerical integration with two microwave pulses of $D = 100$ ns, separated by $T = 500$ ns. The microwave magnetic field amplitude is $B_0=0.2$ gauss. The fit (solid line) is obtained using Eq. (6.12).

The sub-natural line width resolution of the microwave resonance can be seen in Fig. 6.5, where the internal structure has zero-crossings spaced apart by about 1.5 MHz, while the natural width is 3.2 MHz. While the oscillatory SOF lineshape is more complicated than in the single-pulse case, the shift is determined by a similar process of fitting to an ideal two-level resonance profile. The atomic wavefunction

is again evolved in time, but in this case there is interaction with two successive microwave fields. The population in the final $|b\rangle$ state after the atom has interacted with both pulses is obtained by summing the decay probability in all four intervals: during the first pulse, in-between pulses, during the second pulse, and after both pulses have subsided:

$$\begin{aligned}
\rho_{bb}^{SOF}(\Delta, \delta) &= \gamma_{i \rightarrow b} \int_{t=0}^D P_i(t) e^{-\gamma t} dt \\
&+ \gamma_{i \rightarrow b} P_i(D) \int_{t=D}^{D+t_0} e^{-\gamma t} dt \\
&+ \gamma_{i \rightarrow b} \int_{t=D+t_0}^{2D+t_0} P_i^{SOF}(D, t_0, t - (D + t_0), \delta) e^{-\gamma t} dt \\
&+ \gamma_{i \rightarrow b} P_i^{SOF}(D, t_0, D, \delta) \int_{t=2D+t_0}^{\infty} e^{-\gamma t} dt \\
&\equiv I_1(\Delta) + I_2(\Delta) + I_3(\Delta, \delta) + I_4(\Delta, \delta). \tag{6.11}
\end{aligned}$$

Here $\Delta = (\omega - \omega_0)$, $\gamma_{i \rightarrow b}$ and $P_i(t)$ are defined as in the single-pulse case. The first two terms I_1 and I_2 in Eq. (6.11) evolve the atom's state through the first pulse, of duration D , and a subsequent field-free period t_0 .

The third and fourth integrals $I_3(\delta)$ and $I_4(\delta)$ represent the atom's interaction with the second microwave pulse, and the final period of field-free evolution afterward. They involve the quantity $P_i^{SOF}(t_1, t_0, t_2, \delta)$ which is the probability of the atom being in the state $|2\rangle$ ($|0\rangle$) at time t_2 from the start of the second pulse, after interaction with a first pulse of duration t_1 followed by a field-free period t_0 . The

parameter δ is the phase-difference between the two pulses.

The fit function used for the calculated SOF line shape is the difference signal

$$\begin{aligned} \tilde{\rho}_{bb}^{SOF}(\Delta; C, \Delta_0) = & C[I_3(\Delta - \Delta_0, 0) + I_4(\Delta - \Delta_0, 0) \\ & - I_3(\Delta - \Delta_0, \pi) - I_4(\Delta - \Delta_0, \pi)], \end{aligned} \quad (6.12)$$

with I_1 and I_2 from Eq. (6.11) having cancelled since they do not depend on the phase difference δ . As before, the parameters C and Δ_0 are varied, and a pure shift Δ_0 in the line shape is extracted.

Similar to the single-pulse case, shifts can also be determined from the zero-crossing points in Fig. 6.5, but this yields nearly identical values, with the small distortions in the line shape ignored by the symmetric fit function.

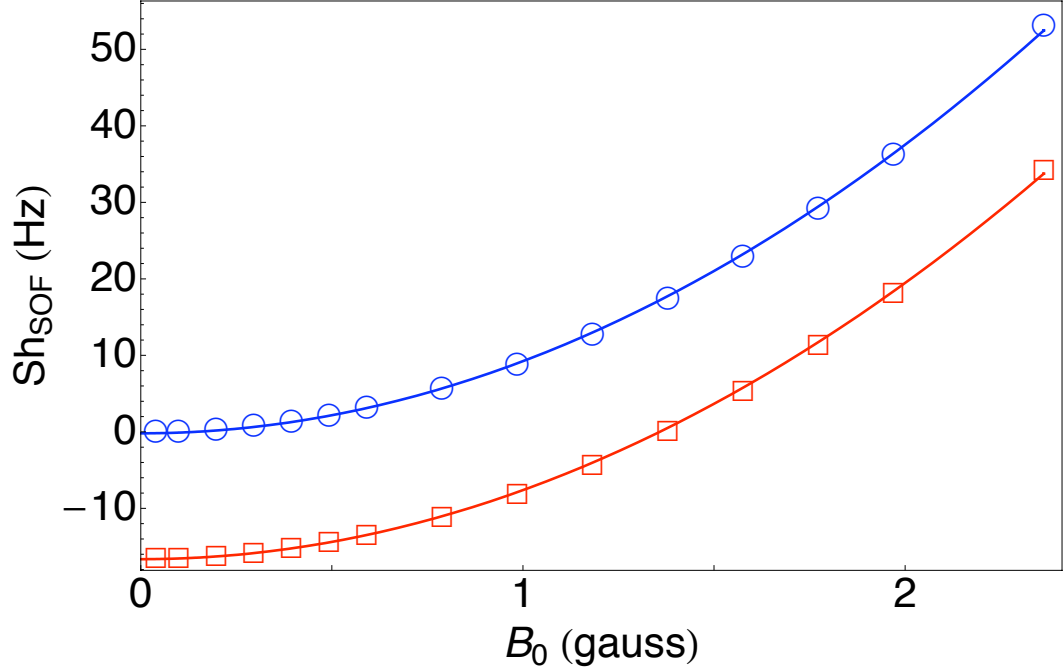


Figure 6.6: SOF shifts of the 2^3P_1 -to- 2^3P_2 resonance versus magnetic field amplitude, for two microwave pulses of $D = 100$ ns, separated by $T = 500$ ns. Shifts are obtained by fits similar to those shown in Fig. 6.5. The squares represent the full shift, while circles show the shifts that would result in the absence of the $\gamma_{20 \rightarrow b}$ interference term in Eq. (6.2).

SOF shifts obtained by the fits of Eq. (6.12) are plotted in Fig. 6.6 for a range of magnetic field amplitudes. Again, the pure AC-Stark shifts (circles), obtained by setting $\gamma_{20 \rightarrow b}$ in Eqs. (6.2) to zero, scale as the square of the microwave field strength, and extrapolate to zero for zero field intensity. The full shifts (square symbols) have the quadratic form of Eq. (6.10) with a residual shift $Sh^{(0)}$ at zero intensity. These shifts, listed in Table 6.2, are almost identical for the 2^3P_1 -to- 2^3P_0 and 2^3P_1 -to- 2^3P_2 intervals. Their magnitudes are much smaller than those in the single-pulse analysis however, and approximately inversely proportional to

Table 6.2: Frequency shifts extrapolated to zero microwave intensity using Eq. (6.10), for helium 2^3P_1 -to- 2^3P_0 ($|1\rangle \rightarrow |0\rangle$) and 2^3P_1 -to- 2^3P_2 ($|1\rangle \rightarrow |2\rangle$) SOF transitions.

D (ns)	T (ns)	$Sh_{SOF}^{(0)}$ (Hz)	
		$ 1\rangle \rightarrow 0\rangle$	$ 1\rangle \rightarrow 2\rangle$
50	200	-41	-41
50	300	-27	-27
50	400	-20	-20
50	500	-16	-16
50	600	-14	-14
50	800	-10	-10
100	300	-27	-28
100	400	-20	-21
100	500	-16	-17
100	600	-14	-14
100	800	-10	-10
150	400	-21	-22
150	500	-16	-17
150	600	-14	-14
150	800	-10	-11

the pulse separation T .

Although the shifts shown in Tables 6.1 and 6.2 are small, microwave measurements of the intervals are now approaching an accuracy where the shifts will need to be considered. The most accurate single-pulse microwave measurements of [13] and [12] have a pulse duration D determined by the travel time through the microwave region, typically 950 and 1700 ns for the two measurements, respectively. From Table 6.1 it can be seen that the interference corrections are less than 10% of the 900 and 1400 Hz measurement uncertainties. The most accurate SOF measurement [16] of the helium 2^3P fine structure uses $D=50, 100$ and 150 ns and $T=300, 400, 500$ and 600 ns for the pulse parameters. From Table 6.2, it is evident that the

corrections that need to be applied are again less than 10% of the 350 Hz measurement uncertainty. The corrections shown in the $|1\rangle \rightarrow |0\rangle$ columns of Tables 6.1 and 6.2 indicate shifts of 0.5 to 15 ppb of the 29.6 GHz interval and these will be important in the anticipated next generation of microwave measurements that aim towards a ppb determination of α from helium 2^3P fine structure.

7 Conclusion

In the preceding chapters an analysis of quantum interference effects on measurements of the helium 2^3P fine-structure intervals performed with a variety of experimental techniques was presented. Corrections to specific measured values were derived where feasible, or else the scale of the interference shifts was calculated. A summary of the interference shifts for the different measurements that were considered is displayed in Fig. 7.1. The original experimental data are shown using solid error bars, along with the theoretically-calculated value of each interval. The dashed error bars indicate the revised values and their estimated uncertainties.

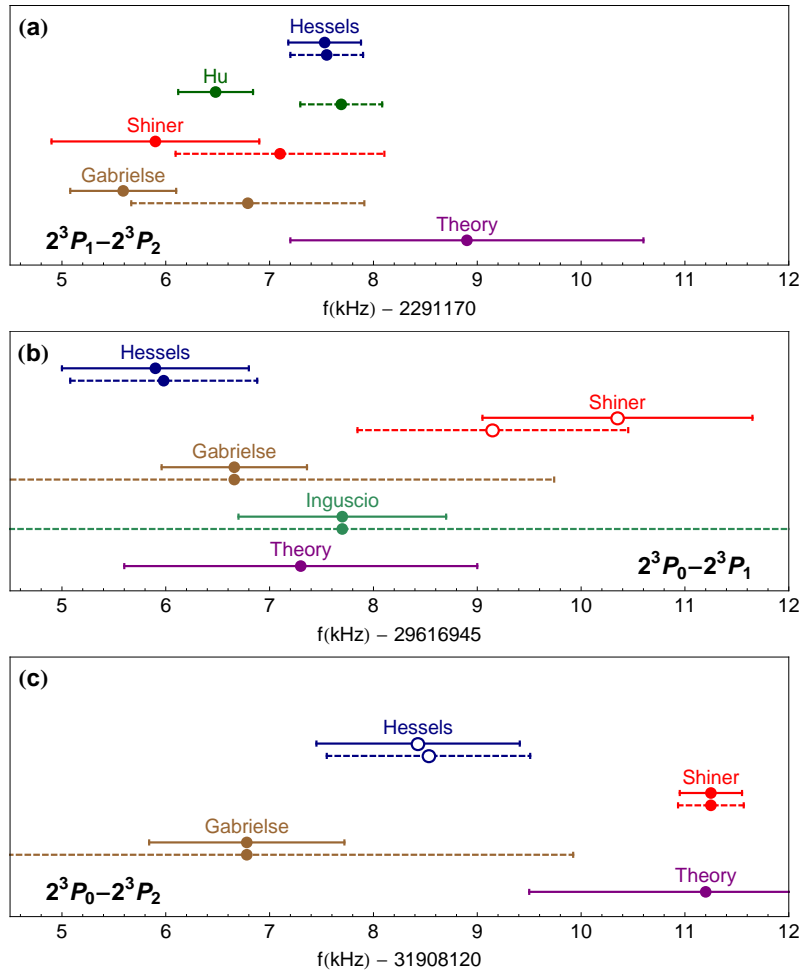


Figure 7.1: Corrected measurements for the 2^3P fine-structure intervals in helium. Filled symbols denote direct measurements, while open symbols represent inferred values based on measurements of the other two intervals. The points labeled Theory show the calculations of Pachucki and Yerokhin [8] adjusted for the CODATA 2014 [19] value of α .

Fig. 7.1(a) shows the results for the $2^3P_1 - 2^3P_2$ fine-structure interval. This interval is susceptible to interference effects in laser spectroscopy, since the interfering resonances (the $J=1$ and $J=2$ levels) used to determine this interval are, at 2.3 GHz, relatively close to one another. Their correspondingly large individual shifts

then additively combine to reduce the measured value of the level splitting. Similar positive corrections are thus applied to each of the three laser measurements of this interval, namely 1.2 ± 0.1 kHz for the Shiner-group value, 1.2 ± 1.0 kHz for the Gabrielse-group data point, and 1.2 ± 0.16 kHz for the value obtained by Hu et. al. The lone microwave measurement by Hessels et. al. used the extremely accurate SOF technique, and receives a correction of only 0.02 ± 0.01 kHz, which is well within the original value’s uncertainty of 0.35 kHz. After correction, all of the values for the interval are seen to be more consistent with each other and with the value predicted by theory.

The measurements of the 2^3P_0 — 2^3P_1 interval are shown in Fig. 7.1(b). A specific correction was not calculated for the saturated-absorption experiment of Gabrielse et. al., due to the complications with light-pressure effects in the measurement of this interval. However, an estimated additional uncertainty of ± 3 kHz is given due to the interference effect, shown using the expanded dotted error bars. It is also not possible, as explained in Chap. 4, to state a correction for the Inguscio group saturated-fluorescence value for this interval, since the experimental parameters are not known in sufficient detail. Nevertheless, an additional measurement uncertainty of ± 10 kHz is proposed, due to incomplete cancellation of the opposing interference shifts, possibly as large as ± 50 kHz, that can arise for the different polarizations of measured fluorescence in such an experiment. The open data point for the Shiner group experiment indicates that its value was inferred from actual measurements of

the other two intervals, and hence its correction of -1.2 ± 0.1 is due primarily to the interference effect on the $2^3P_1-2^3P_2$ interval. The shifted data point is now closer to the other measurements, and more in line with the theoretical value. Finally, the very accurate Hessels group microwave measurement (± 0.9 kHz) is once again corrected by only a small 0.08 ± 0.02 kHz shift.

Lastly, Fig. 7.1(c) shows the experimental values obtained for the $2^3P_0-2^3P_2$ interval. The Gabrielse group value receives the same increase in its uncertainty as in Fig. 7.1(b), since the measurement of this interval is similarly affected by light-pressure effects. The direct laser measurement of the Shiner et. al for this interval was not explicitly modeled in Chap. 3, so it is only given an additional estimated uncertainty of ± 0.1 kHz. The microwave value (Hessels group) for the interval is derived from measurements of the other two, and so obtains a combined correction of 0.1 ± 0.03 kHz, which moves it only slightly closer to the theoretical value.

In general, while the scale of the shift depends on the particular experimental method, the quantum interference effect is seen to be important for precision fine-structure spectroscopy, despite the large separation of the resonances (the two closest resonances, the J=1 and J=2 levels, are 1400 natural line widths apart). The microwave SOF experiment, however, is particularly robust against the interference effect, due to the sub-natural SOF resolution and the relatively-large 27 GHz separation between the measured microwave resonance and the nearest off-resonant transition. It is evident from this work that interference effects should

be examined carefully in any precision measurement for which the experimental uncertainty is of comparable magnitude to that of the interference shift, given by the rule of thumb as the width of the observed resonance squared, divided by the frequency separation to the nearest neighboring resonance.

While correction for quantum interference effects brings precision fine-structure measurements into greater agreement with each other (at the kilohertz level), both experimental values and theoretical calculations will need to improve in accuracy by an order of magnitude in order to achieve a competitive determination of the fine-structure constant from helium spectroscopy.

Since parts of the current work were published, a number of groups have incorporated the quantum-interference phenomenon in a variety of experimental and theoretical analyses. Feng, et. al. applied interference corrections to their laser measurement [18] of the helium fine-structure, as mentioned in Chap. 3. Quantum interference was also considered in precision hydrogen spectroscopy for determination of the Rydberg constant and the proton RMS charge radius [37]. A theoretical study of quantum interference in laser spectroscopy of muonic hydrogen, deuterium, and helium-3 was conducted [49], also of importance to the proton charge radius program. The interference effect was also shown [45] to be significant in precision measurements of the $^{6,7}\text{Li}$ D2 lines, and subsequent determination of relative nuclear isotope charge radii. Quantum interference in two-photon frequency-comb spectroscopy was also studied [50]. Finally, Truong, et. al. produced a detailed

analysis in which quantum interference was shown to vanish for precision measurements of the $6P_{1/2}$ hyperfine splitting in Cs [51], which are used to determine the Boltzmann constant to high accuracy.

A Master Equations

The quantum state of an atom interacting with an external field can be represented by the density operator

$$\rho = \sum_i P_i |\Psi_i\rangle\langle\Psi_i|, \quad (\text{A.1})$$

where in general ρ represents an incoherent superposition (mixture) of states $\{|\Psi_i\rangle\}$ with P_i the probability of being in state $|\Psi_i\rangle$. The density operator can thus model an ensemble of identical atoms in possibly different states. The density-matrix equations describing the evolution of the atom's state may be then obtained from a Liouville-vonNeumann (or master) equation [52] for the density operator, of the form

$$\dot{\rho} = -\frac{i}{\hbar} [H_A + H_{AF}, \rho] + \mathcal{D}[G]\rho. \quad (\text{A.2})$$

Here $[A, B]$ denotes the commutator of A and B, and $\mathcal{D}[c]\rho \equiv c\rho c^\dagger - \frac{1}{2}(c^\dagger c\rho + \rho c^\dagger c)$ is the Lindblad superoperator. In Eq. (A.2), H_A is the atomic free-evolution Hamiltonian, while H_{AF} is the atom-field interaction, which generates driving terms in the density-matrix equations that model absorption and stimulated-emission processes.

The operator G is a suitably-chosen damping operator, and represents relaxation processes in the atom. These processes include both radiative decay, which changes atomic populations, and elastic atom-atom collisions, which only alter the phases of coherent superpositions. This part of the master equation leads to decay terms in the density-matrix equations, including terms that incorporate quantum interference.

A.1 The Two-level Atom

It is instructive to first consider the simplest case, a two-level atom interacting with an applied field. The ground and excited states are denoted $|1\rangle$ and $|2\rangle$ respectively, with the energy of the ground state chosen as zero, so that $E_2 = \hbar\omega_0$, where ω_0 is the transition frequency between the states. The free-atom Hamiltonian is then simply written as $H_A = \hbar\omega_0|2\rangle\langle 2|$.

An applied electric field \vec{E} (e.g. the field of a laser), of frequency ω , amplitude E_0 , and unit polarization-vector $\hat{\epsilon}$ induces electric-dipole transitions between the states $|1\rangle$ and $|2\rangle$, which are necessarily of opposite parity. The field consists of positive and negative frequency components

$$\vec{E} = \frac{E_0}{2} (\hat{\epsilon}e^{i\omega t} + \hat{\epsilon}^*e^{-i\omega t}) = \vec{E}_0^{(+)}e^{-i\omega t} + \vec{E}_0^{(-)}e^{i\omega t}, \quad (\text{A.3})$$

while the dipole operator can be represented as

$$\vec{d} = \langle 1|\vec{d}|2\rangle|1\rangle\langle 2| + \langle 2|\vec{d}|1\rangle|2\rangle\langle 1| = \langle 1|\vec{d}|2\rangle\sigma + \langle 2|\vec{d}|1\rangle\sigma^\dagger, \quad (\text{A.4})$$

where $\sigma = |1\rangle\langle 2|$ and $\sigma^\dagger = |2\rangle\langle 1|$ are atomic lowering and raising operators. The atom-field interaction energy in the dipole approximation is thus

$$\begin{aligned} H_{AF} &= -\vec{d} \cdot \vec{E} \\ &= -\langle 1|\vec{d}|2\rangle \cdot \vec{E}_0^{(+)} e^{-i\omega t} \sigma - \langle 1|\vec{d}|2\rangle \cdot \vec{E}_0^{(-)} e^{i\omega t} \sigma \\ &\quad - \langle 2|\vec{d}|1\rangle \cdot \vec{E}_0^{(+)} e^{-i\omega t} \sigma^\dagger - \langle 2|\vec{d}|1\rangle \cdot \vec{E}_0^{(-)} e^{i\omega t} \sigma^\dagger. \end{aligned} \quad (\text{A.5})$$

A.1.1 Rotating-wave Approximation

The atom-field Hamiltonian can be expressed in the interaction picture by applying the unitary transformation $U = e^{iH_A t/\hbar} = e^{i\omega_0 t|2\rangle\langle 2|} = |1\rangle\langle 1| + e^{i\omega_0 t}|2\rangle\langle 2|$, so that

$$\begin{aligned} H_{AF,I} &= -\langle 1|\vec{d}|2\rangle \cdot \vec{E}_0^{(+)} e^{-i(\omega+\omega_0)t} \sigma - \langle 1|\vec{d}|2\rangle \cdot \vec{E}_0^{(-)} e^{i(\omega-\omega_0)t} \sigma \\ &\quad - \langle 2|\vec{d}|1\rangle \cdot \vec{E}_0^{(+)} e^{-i(\omega-\omega_0)t} \sigma^\dagger - \langle 2|\vec{d}|1\rangle \cdot \vec{E}_0^{(-)} e^{i(\omega+\omega_0)t} \sigma^\dagger. \end{aligned} \quad (\text{A.6})$$

The first and last terms in Eq. (A.6) oscillate rapidly as $e^{\pm i(\omega+\omega_0)t}$ (i.e., at optical frequencies), compared to the much slower time-dependence $e^{\pm i\Delta t}$ of the middle terms, where $\Delta = \omega - \omega_0$ is the detuning of the field from the atomic transition. If the applied field is near resonance, so that $|\Delta| \ll \omega + \omega_0$, then the former terms may be neglected, since they average to zero on the longer time scale characterized by the detuning frequency. Dropping the rapidly-varying terms, and

transforming back to the Schrödinger picture results in the atom-field interaction in the rotating-wave approximation,

$$\begin{aligned} H_{AF} &= -\langle 1|\vec{d}|2\rangle \cdot \vec{E}_0^{(-)} e^{i\omega t} \sigma - \langle 2|\vec{d}|1\rangle \cdot \vec{E}_0^{(+)} e^{-i\omega t} \sigma^\dagger \\ &= \frac{\hbar}{2} \Omega_{12} e^{i\omega t} \sigma + \frac{\hbar}{2} \Omega_{12}^* e^{-i\omega t} \sigma^\dagger. \end{aligned} \quad (\text{A.7})$$

The last line of Eq. (A.7) is written using the Rabi frequency, which characterizes the strength of the electric-dipole coupling, and is defined as

$$\Omega_{ij} = -\frac{E_0}{\hbar} \langle i|\hat{\epsilon} \cdot \vec{d}|j\rangle = \frac{eE_0}{\hbar} \hat{\epsilon} \cdot \langle i|\vec{r}|j\rangle, \quad (\text{A.8})$$

where e is the magnitude of the elementary charge (so that the electron has charge $q = -e$), and $\langle i|\vec{r}|j\rangle$ is the dipole matrix element between states $|i\rangle$ and $|j\rangle$.

A.1.2 Corotating Frame

The atomic Hamiltonian is typically further transformed to a frame corotating with the applied field, in order to remove the time-dependence on the field frequency.

This is accomplished by the unitary transformation $U = e^{i\omega t|2\rangle\langle 2|} = |1\rangle\langle 1| + e^{i\omega t}|2\rangle\langle 2|$,

resulting in a total atomic Hamiltonian in the rotating frame

$$\begin{aligned} \tilde{H} &= U H U^\dagger + i\hbar (\partial_t U) U^\dagger \\ &= -\hbar\Delta|2\rangle\langle 2| + \frac{\hbar}{2} (\Omega_{12}|1\rangle\langle 2| + \Omega_{12}^*|2\rangle\langle 1|) \\ &= -\hbar\Delta\sigma^\dagger\sigma + \frac{\hbar}{2} (\Omega_{12}\sigma + \Omega_{12}^*\sigma^\dagger) \\ &= \tilde{H}_A + \tilde{H}_{AF}. \end{aligned} \quad (\text{A.9})$$

A.1.3 Density-matrix Equations

Using the forms of \tilde{H}_A and \tilde{H}_{AF} in Eq. (A.9), and modeling spontaneous decay by the operator

$$G = \Gamma|g\rangle\langle e| = \Gamma\sigma, \quad (\text{A.10})$$

(where $\gamma = \Gamma^2$ is the decay rate back to the ground state), the master equation for the two-level atom is

$$\dot{\rho} = -\frac{i}{\hbar} \left[-\hbar\Delta\sigma^\dagger\sigma + \frac{\hbar}{2} (\Omega_{12}\sigma + \Omega_{12}^*\sigma^\dagger), \rho \right] + \gamma \mathcal{D}[\sigma]\rho. \quad (\text{A.11})$$

Carrying out the algebra leads to the optical Bloch equations,

$$\dot{\rho}_{11} = \frac{i}{2}\Omega_{12}^*\rho_{12} - \frac{i}{2}\Omega_{12}\rho_{21} + \gamma\rho_{22} \quad (\text{A.12a})$$

$$\dot{\rho}_{12} = -\left(\frac{\gamma}{2} + i\Delta_2\right)\rho_{12} - \frac{i}{2}\Omega_{12}(\rho_{22} - \rho_{11}) \quad (\text{A.12b})$$

$$\dot{\rho}_{21} = -\left(\frac{\gamma}{2} - i\Delta_2\right)\rho_{21} + \frac{i}{2}\Omega_{12}^*(\rho_{22} - \rho_{11}) \quad (\text{A.12c})$$

$$\dot{\rho}_{22} = -\frac{i}{2}\Omega_{12}^*\rho_{12} + \frac{i}{2}\Omega_{12}\rho_{21} - \gamma\rho_{22}. \quad (\text{A.12d})$$

A.2 The Three-level Atom

For a three-level atom with ground state $|1\rangle$ and excited states $|2\rangle$ and $|3\rangle$, the energies are $E_2 = \hbar\omega_{21}$ and $E_3 = \hbar\omega_{31}$ for the transition frequencies ω_{21} and ω_{31} .

With atomic operators $\sigma_2 = |1\rangle\langle 2|$ and $\sigma_3 = |1\rangle\langle 3|$ the Hamiltonian and decay operators are written

$$\begin{aligned}\tilde{H}_A &= -\hbar\Delta_2|2\rangle\langle 2| - \hbar\Delta_3|3\rangle\langle 3| \\ &= -\hbar\left(\Delta_2\sigma_2^\dagger\sigma_2 + \Delta_3\sigma_3^\dagger\sigma_3\right),\end{aligned}\tag{A.13a}$$

$$\begin{aligned}\tilde{H}_{AF} &= \frac{\hbar}{2}\left(\Omega_{12}|1\rangle\langle 2| + \Omega_{12}^*|2\rangle\langle 1| + \Omega_{13}|1\rangle\langle 3| + \Omega_{13}^*|3\rangle\langle 1|\right) \\ &= \frac{\hbar}{2}\left(\Omega_{12}\sigma_2 + \Omega_{12}^*\sigma_2^\dagger + \Omega_{13}\sigma_3 + \Omega_{13}^*\sigma_3^\dagger\right),\end{aligned}\tag{A.13b}$$

$$\begin{aligned}G &= \Gamma_2|1\rangle\langle 2| + \Gamma_3|1\rangle\langle 3| \\ &= \Gamma_2\sigma_2 + \Gamma_3\sigma_3,\end{aligned}\tag{A.13c}$$

where $\Delta_2 = \omega - \omega_{21}$, and $\Delta_3 = \omega - \omega_{31}$ are the detunings of the field from the transition frequencies to the excited states $|2\rangle$, and $|3\rangle$ respectively. The quantities Γ_2 and Γ_3 are defined so that $\gamma_2 = \Gamma_2^2$ and $\gamma_3 = \Gamma_3^2$ are the corresponding rates of spontaneous decay. The master equation is then

$$\begin{aligned}\dot{\rho} &= -\frac{i}{\hbar}\left[-\hbar\left(\Delta_2\sigma_2^\dagger\sigma_2 + \Delta_3\sigma_3^\dagger\sigma_3\right), \rho\right] \\ &\quad - \frac{i}{\hbar}\left[\frac{\hbar}{2}\left(\Omega_{12}\sigma_2 + \Omega_{12}^*\sigma_2^\dagger + \Omega_{13}\sigma_3 + \Omega_{13}^*\sigma_3^\dagger\right), \rho\right] \\ &\quad + \mathcal{D}[\Gamma_2\sigma_2 + \Gamma_3\sigma_3]\rho.\end{aligned}\tag{A.14}$$

Of particular note is the damping term in Eq. (A.14), in which the decays from the excited states $|2\rangle$ and $|3\rangle$ to the ground state $|1\rangle$ are added into a single Lindblad superoperator term. This represents the physical situation where the two decay pathways to $|1\rangle$ are indistinguishable, and hence are interfering processes. The

master equation (A.14) yields the three-level density-matrix equations

$$\begin{aligned} \dot{\rho}_{11} = & \frac{i}{2}\Omega_{12}^*\rho_{12} - \frac{i}{2}\Omega_{12}\rho_{21} + \frac{i}{2}\Omega_{13}^*\rho_{13} - \frac{i}{2}\Omega_{13}\rho_{31} \\ & + \gamma_2\rho_{22} + \gamma_3\rho_{33} + \gamma_{23}(\rho_{23} + \rho_{32}) \end{aligned} \quad (\text{A.15a})$$

$$\dot{\rho}_{22} = -\frac{i}{2}\Omega_{12}^*\rho_{12} + \frac{i}{2}\Omega_{12}\rho_{21} - \gamma_2\rho_{22} - \frac{\gamma_{23}}{2}(\rho_{23} + \rho_{32}) \quad (\text{A.15b})$$

$$\dot{\rho}_{33} = -\frac{i}{2}\Omega_{13}^*\rho_{13} + \frac{i}{2}\Omega_{13}\rho_{31} - \gamma_3\rho_{33} - \frac{\gamma_{23}}{2}(\rho_{23} + \rho_{32}) \quad (\text{A.15c})$$

$$\dot{\rho}_{12} = -i\Delta_2\rho_{12} - \frac{i}{2}\Omega_{12}(\rho_{22} - \rho_{11}) - \frac{i}{2}\Omega_{13}\rho_{32} - \frac{\gamma_2}{2}\rho_{12} - \frac{\gamma_{23}}{2}\rho_{13} \quad (\text{A.15d})$$

$$\dot{\rho}_{13} = -i\Delta_3\rho_{13} - \frac{i}{2}\Omega_{13}(\rho_{33} - \rho_{11}) - \frac{i}{2}\Omega_{12}\rho_{23} - \frac{\gamma_3}{2}\rho_{13} - \frac{\gamma_{23}}{2}\rho_{12} \quad (\text{A.15e})$$

$$\dot{\rho}_{23} = -i\omega_{23}\rho_{23} - \frac{i}{2}\Omega_{12}^*\rho_{13} + \frac{i}{2}\Omega_{13}\rho_{21} - \frac{\gamma_{23}}{2}\rho_{22} - \left(\frac{\gamma_2}{2} + \frac{\gamma_3}{2}\right)\rho_{23}. \quad (\text{A.15f})$$

The cross-damping rate γ_{23} in Eq. (A.15) is defined as $\gamma_{23} = \Gamma_2\Gamma_3$, and represents quantum interference between the radiative decay channels.

A.3 The Four-level Atom

For the four-level atom introduced in Chap. 2, there are two ground states ($|0\rangle$ and $|1\rangle$) and two excited states ($|2\rangle$ and $|3\rangle$), where the applied field couples $|1\rangle$ to both excited states, but $|0\rangle$ is a dark state. Using atomic operators $\sigma_{ij} = |i\rangle\langle j|$ ($i = 0, 1,$

$j = 2, 3$) the Hamiltonian and damping operators are written as

$$\begin{aligned}\tilde{H}_A &= -\hbar\Delta_2|2\rangle\langle 2| - \hbar\Delta_3|3\rangle\langle 3| \\ &= -\hbar\left(\Delta_2\sigma_{12}^\dagger\sigma_{12} + \Delta_3\sigma_{13}^\dagger\sigma_{13}\right),\end{aligned}\tag{A.16a}$$

$$\begin{aligned}\tilde{H}_{AF} &= \frac{\hbar}{2}\left(\Omega_{12}|1\rangle\langle 2| + \Omega_{12}^*|2\rangle\langle 1| + \Omega_{13}|1\rangle\langle 3| + \Omega_{13}^*|3\rangle\langle 1|\right) \\ &= \frac{\hbar}{2}\left(\Omega_{12}\sigma_{12} + \Omega_{12}^*\sigma_{12}^\dagger + \Omega_{13}\sigma_{13} + \Omega_{13}^*\sigma_{13}^\dagger\right),\end{aligned}\tag{A.16b}$$

$$G_1 = \Gamma_{21}|1\rangle\langle 2| + \Gamma_{31}|1\rangle\langle 3| = \Gamma_{21}\sigma_{12} + \Gamma_{31}\sigma_{13},\tag{A.16c}$$

$$G_2 = \Gamma_{20}|0\rangle\langle 2| + \Gamma_{30}|0\rangle\langle 3| = \Gamma_{20}\sigma_{02} + \Gamma_{30}\sigma_{03}.\tag{A.16d}$$

Here $\Delta_2 = \omega - \omega_{21}$ and $\Delta_3 = \omega - \omega_{31}$ are the detunings of the field from the excited-state transitions as before, and now $\gamma_{20} = \Gamma_{20}^2$ and $\gamma_{21} = \Gamma_{21}^2$ are the partial rates of spontaneous decay from $|2\rangle$ to the ground states $|0\rangle$ and $|1\rangle$, respectively. The partial rates $\gamma_{31} = \Gamma_{31}^2$ and $\gamma_{30} = \Gamma_{30}^2$ are similarly defined. The corresponding master equation is

$$\begin{aligned}\dot{\rho} &= -\frac{i}{\hbar}\left[-\hbar\left(\Delta_2\sigma_{12}^\dagger\sigma_{12} + \Delta_3\sigma_{13}^\dagger\sigma_{13}\right), \rho\right] \\ &\quad - \frac{i}{\hbar}\left[\frac{\hbar}{2}\left(\Omega_{12}\sigma_{12} + \Omega_{12}^*\sigma_{12}^\dagger + \Omega_{13}\sigma_{13} + \Omega_{13}^*\sigma_{13}^\dagger\right), \rho\right] \\ &\quad + \mathcal{D}[\Gamma_{21}\sigma_{12} + \Gamma_{31}\sigma_{13}]\rho + \mathcal{D}[\Gamma_{20}\sigma_{02} + \Gamma_{30}\sigma_{03}]\rho.\end{aligned}\tag{A.17}$$

There are two decay terms in Eq. (A.17), which models distinguishable decay processes to either one of the two ground states. These different pathways can in principle be detected by probing which ground state the atom occupies, or by measuring different polarizations of fluorescence. The excited state from which the

atom decays to a ground state is not known, however, so quantum interference occurs between the two possible decay channels in each case (i.e., $|2\rangle \rightarrow |1\rangle$ interferes with $|3\rangle \rightarrow |1\rangle$), and similarly for decay to $|0\rangle$), and this is reflected in the form of the operators. Eq. (A.17) leads to the density-matrix Eqs. (2.3) for the four-level system

$$\begin{aligned} \dot{\rho}_{11} = & \frac{i}{2}\Omega_{12}^*\rho_{12} - \frac{i}{2}\Omega_{12}\rho_{21} + \frac{i}{2}\Omega_{13}^*\rho_{13} - \frac{i}{2}\Omega_{13}\rho_{31} \\ & + \gamma_{2\rightarrow 1}\rho_{22} + \gamma_{3\rightarrow 1}\rho_{33} + \gamma_{23\rightarrow 1}(\rho_{23} + \rho_{32}) \end{aligned} \quad (\text{A.18a})$$

$$\dot{\rho}_{22} = -\frac{i}{2}\Omega_{12}^*\rho_{12} + \frac{i}{2}\Omega_{12}\rho_{21} - \gamma_2\rho_{22} - \frac{\gamma_{23}}{2}(\rho_{23} + \rho_{32}) \quad (\text{A.18b})$$

$$\dot{\rho}_{33} = -\frac{i}{2}\Omega_{13}^*\rho_{13} + \frac{i}{2}\Omega_{13}\rho_{31} - \gamma_3\rho_{33} - \frac{\gamma_{23}}{2}(\rho_{32} + \rho_{23}) \quad (\text{A.18c})$$

$$\dot{\rho}_{12} = -i\Delta_2\rho_{12} - \frac{i}{2}\Omega_{12}(\rho_{22} - \rho_{11}) - \frac{i}{2}\Omega_{13}\rho_{32} - \frac{\gamma_2}{2}\rho_{12} - \frac{\gamma_{23}}{2}\rho_{13} \quad (\text{A.18d})$$

$$\dot{\rho}_{13} = -i\Delta_3\rho_{13} - \frac{i}{2}\Omega_{13}(\rho_{33} - \rho_{11}) - \frac{i}{2}\Omega_{12}\rho_{23} - \frac{\gamma_3}{2}\rho_{13} - \frac{\gamma_{23}}{2}\rho_{12} \quad (\text{A.18e})$$

$$\dot{\rho}_{23} = -i\omega_{23}\rho_{23} - \frac{i}{2}\Omega_{12}^*\rho_{13} + \frac{i}{2}\Omega_{13}\rho_{21} - \left(\frac{\gamma_2}{2} + \frac{\gamma_3}{2}\right)\rho_{23} - \frac{\gamma_{23}}{2}(\rho_{22} + \rho_{33}). \quad (\text{A.18f})$$

Eqs. (A.18) use the notation of Chap. 2, where $\gamma_{i\rightarrow j} \equiv \gamma_{ij}$, with total decay rates from each excited state $\gamma_2 = \gamma_{2\rightarrow 0} + \gamma_{2\rightarrow 1}$ and $\gamma_3 = \gamma_{3\rightarrow 0} + \gamma_{3\rightarrow 1}$. The cross-damping rates are defined as $\gamma_{23\rightarrow 0} = \Gamma_{20}\Gamma_{30}$ and $\gamma_{23\rightarrow 1} = \Gamma_{21}\Gamma_{31}$, with a redefinition of $\gamma_{23} = \gamma_{23\rightarrow 0} + \gamma_{23\rightarrow 1}$.

A.4 General Systems

Derivation of general density-matrix equations for transitions among the $n=2$ triplet helium states may be carried out in an analogous manner. Denoting the $2^3S_1(m_J = \mu)$ metastable states as ground states $\{|g_\mu\rangle\}$ and the $2^3P_{J=j}(m_J = m)$ excited states as $\{|e_{jm}\rangle\}$, the atom-field Hamiltonian can be written using lowering and raising operators of the form $\sigma_{\mu,jm} = |g_\mu\rangle\langle e_{jm}|$ and $\sigma_{\mu,jm}^\dagger = |e_{jm}\rangle\langle g_\mu|$, respectively. The decay terms in the master equation involve radiative decay rates $\gamma_{jm \rightarrow \mu}$, which are given by the expression of Eq. (4.4)b as $\gamma_{jm \rightarrow \mu} = \gamma_{\mu jm}^{\mu jm}$, while the cross-damping rates are $\gamma_{jm,j'm' \rightarrow \mu} = \gamma_{\mu jm}^{\mu j'm'}$. Insertion of these operator forms into the master equation (A.2) results in the density-matrix Eqs. (4.3).

Similarly, Eqs. (6.2), used to model the microwave measurements in Chap. 6, may be derived using the appropriate atom-field and decay operators which describe the specific driven transitions and spontaneous decay processes involved in the measurement. In this case, the Rabi frequencies involve magnetic-dipole matrix elements, and explicitly include the frequency of the applied field, as the rotating-wave approximation is no longer valid for this system.

A.5 Rabi Frequency Conventions

The density matrix equations listed in Chaps. 2—6 (see Eqs. (2.3), (2.11), (3.4), (4.3), (5.2), and (6.2)) are consistent with the derivations developed here, but

originally appeared [40, 42, 43, 47] following the notation of [31], in which the Rabi frequencies and their conjugates are interchanged. While both formulations preserve explicitly complex forms of the Rabi frequencies, for the case of a linearly-polarized field (as in Chaps. 4—6), the Rabi frequency is real-valued. Furthermore, the phases of the states $|i\rangle$ and $|j\rangle$ can be chosen so that the dipole matrix element, and hence the Rabi frequency is always real, and in the literature $\Omega_{ij} = \Omega_{ij}^*$ is usually considered a real quantity. Thus, the density-matrix equations in either convention are equivalent descriptions of the physics of the atom-field interaction, and result in identical interference shifts.

B Matrix Elements

Determination of matrix elements $\langle i|\vec{r}|j\rangle$ between the metastable 2^3S_1 states and excited 2^3P_J states is necessary in order to compute the Rabi frequencies for laser-driven electric-dipole transitions, as well for calculation of spontaneous decay and cross-damping rates. Denoting the metastable $2^3S_{1,m=\mu}$ states as $|g_\mu\rangle$ and the excited $2^3P_{J,m_J=m}$ states as $|e_{Jm}\rangle$, the matrix elements $\langle g_\mu|\vec{r}|e_{Jm}\rangle$ can be derived by applying the Wigner-Eckart theorem, and are expressed in the spherical basis $q \in \{-1, 0, 1\}$ as:

$$\langle g_\mu|r_q|e_{Jm}\rangle = \frac{(-1)^{1-\mu}}{\sqrt{3}}\sqrt{2J+1} \begin{pmatrix} 1 & 1 & J \\ -\mu & q & m \end{pmatrix} \langle g||r||e_J\rangle, \quad (\text{B.1})$$

where $\langle g||r||e_J\rangle$ is the reduced matrix element, and the brackets denote a Wigner-3j symbol.

Calculation of $\langle g||r||e_J\rangle$ would typically involve explicit helium wavefunctions, but in this work it is obtained instead using the expression for the decay rate, which includes the square of the reduced element.

The theoretical expression for the total rate of decay γ_J from any $2^3P_{J,m}$ state to the metastable states $2^3S_{1,\mu}$ is given by $\gamma_J = \sum_{\mu} \gamma_{\mu Jm}^{\mu Jm}$, where the sum is over $\mu \in \{-1, 0, 1\}$, and the partial decay rates are:

$$\begin{aligned} \gamma_{\mu Jm}^{\mu Jm} &= \frac{e^2 \bar{\omega}^3}{3\pi\epsilon_0 \hbar c^3} \langle g_{\mu} | \vec{r} | e_{Jm} \rangle \cdot \langle e_{Jm} | \vec{r} | g_{\mu} \rangle \\ &= \Gamma_{\mu Jm} (\langle g || r || e_J \rangle)^2. \end{aligned} \quad (\text{B.2})$$

Here, $\bar{\omega}$ is the average $2S - 2P$ frequency interval, which is about four orders of magnitude greater than the fine-structure splittings, and thus all of the excited triplet states decay at essentially the same rate, $\gamma_J = \gamma$. In the last line of Eq. (B.2), the quantity $\Gamma_{\mu Jm}$ includes all factors except the reduced matrix elements, and equating the total decay rate γ to the numerical value $\gamma_{num} = 1/\tau$ (where $\tau = 97.9$ ns is the lifetime of the states [41]) lets us solve for $\langle g || r || e_J \rangle$:

$$\begin{aligned} \frac{1}{\tau} &= (\langle g || r || e_J \rangle)^2 \sum_{\mu} \Gamma_{\mu Jm}, \text{ or} \\ \langle g || r || e_J \rangle &= \left(\tau \sum_{\mu} \Gamma_{\mu Jm} \right)^{-1/2}. \end{aligned} \quad (\text{B.3})$$

Eq. (B.3) yields the same value of the reduced element for all J , and any choice of m , of $\langle g || r || e_J \rangle \approx 4.385a_0$, where a_0 is the Bohr radius. Table B.1 lists the values of the matrix elements (with the reduced elements omitted), to illustrate the relative strengths of the various dipole couplings. In practice, the ratios of these matrix elements are used to express all decay and cross-damping rates in the density-matrix equations in terms of the total decay rate γ .

Table B.1: Electric-dipole matrix elements $\{\langle 2^3S_{1,\mu}|r_q|2^3P_{J,m}\rangle\}$ ($q=-1,0,1$) between metastable and excited triplet states (the reduced-element factor $\langle g||r||e_J\rangle$ is not shown).

$\langle 2^3S_{1,\mu} r_q 2^3P_{J,m}\rangle$	$2^3S_{1,-1}$	$2^3S_{1,0}$	$2^3S_{1,1}$
$2^3P_{2,-2}$	$\{0, 0, \frac{1}{\sqrt{3}}\}$	0	0
$2^3P_{2,-1}$	$\{0, -\frac{1}{\sqrt{6}}, 0\}$	$\{0, 0, \frac{1}{\sqrt{6}}\}$	0
$2^3P_{2,0}$	$\{\frac{1}{3\sqrt{2}}, 0, 0\}$	$\{0, -\frac{\sqrt{2}}{3}, 0\}$	$\{0, 0, \frac{1}{3\sqrt{2}}\}$
$2^3P_{2,1}$	0	$\{\frac{1}{\sqrt{6}}, 0, 0\}$	$\{0, -\frac{1}{\sqrt{6}}, 0\}$
$2^3P_{2,2}$	0	0	$\{\frac{1}{\sqrt{3}}, 0, 0\}$
$2^3P_{1,-1}$	$\{0, -\frac{1}{\sqrt{6}}, 0\}$	$\{0, 0, -\frac{1}{\sqrt{6}}\}$	0
$2^3P_{1,0}$	$\{\frac{1}{\sqrt{6}}, 0, 0\}$	0	$\{0, 0, -\frac{1}{\sqrt{6}}\}$
$2^3P_{1,1}$	0	$\{\frac{1}{\sqrt{6}}, 0, 0\}$	$\{0, \frac{1}{\sqrt{6}}, 0\}$
$2^3P_{0,0}$	$\{\frac{1}{3}, 0, 0\}$	$\{0, \frac{1}{3}, 0\}$	$\{0, 0, \frac{1}{3}\}$

Bibliography

1. Schwartz, C. Fine Structure of Helium. *Phys. Rev.* **134**, A1181–A1187 (5A June 1964).
2. Yan, Z.-C. & Drake, G. W. F. High Precision Calculation of Fine Structure Splittings in Helium and He-Like Ions. *Phys. Rev. Lett.* **74**, 4791–4794 (24 June 1995).
3. Zhang, T., Yan, Z.-C. & Drake, G. W. F. QED Corrections of $O(mc^2\alpha^7\ln\alpha)$ to the Fine Structure Splittings of Helium and He-like Ions. *Phys. Rev. Lett.* **77**, 1715–1718 (9 Aug. 1996).
4. Drake, G. W. F. Progress in helium fine-structure calculations and the fine-structure constant. *Can. J. Phys.* **80**, 1195–1212 (2002).
5. Pachucki, K. & Sapirstein, J. Contributions to helium fine structure of order $m\alpha^7$. *J. Phys. B* **33**, 5297 (2000).
6. Pachucki, K. & Sapirstein, J. Higher-order recoil corrections to helium fine structure. *J. Phys. B* **36**, 803 (2003).
7. Pachucki, K. Improved Theory of Helium Fine Structure. *Phys. Rev. Lett.* **97**, 013002 (1 July 2006).
8. Pachucki, K. & Yerokhin, V. A. Fine Structure of Heliumlike Ions and Determination of the Fine Structure Constant. *Phys. Rev. Lett.* **104**, 070403 (7 Feb. 2010).
9. Shiner, D., Dixon, R. & Zhao, P. Precise measurement of the Lamb shift and fine structure of the 2S-2P transition in triplet helium. *Phys. Rev. Lett.* **72**, 1802–1805 (12 Mar. 1994).
10. Storry, C. H. & Hessels, E. A. Precision microwave measurement of the $2^3P_1 \rightarrow 2^3P_0$ interval in atomic helium. *Phys. Rev. A* **58**, R8–R11 (1 July 1998).
11. Minardi, F. *et al.* Measurement of the Helium $2^3P_0 - 2^3P_1$ Fine Structure Interval. *Phys. Rev. Lett.* **82**, 1112–1115 (6 Feb. 1999).
12. Storry, C. H., George, M. C. & Hessels, E. A. Precision Microwave Measurement of the $2^3P_1 - 2^3P_2$ Interval in Atomic Helium. *Phys. Rev. Lett.* **84**, 3274–3277 (15 Apr. 2000).

13. George, M. C., Lombardi, L. D. & Hessels, E. A. Precision Microwave Measurement of the $2^3P_1 - 2^3P_0$ Interval in Atomic Helium: A Determination of the Fine-Structure Constant. *Phys. Rev. Lett.* **87**, 173002 (17 Oct. 2001).
14. Pastor, P. C. *et al.* Absolute Frequency Measurements of the $2^3S_1 \rightarrow 2^3P_{1,2}$ Atomic Helium Transitions around 1083 nm. *Phys. Rev. Lett.* **92**, 023001 (Jan. 2004).
15. Zelevinsky, T., Farkas, D. & Gabrielse, G. Precision Measurement of the Three 2^3P_J Helium Fine Structure Intervals. *Phys. Rev. Lett.* **95**, 203001 (Nov. 2005).
16. Borbely, J. S. *et al.* Separated oscillatory-field microwave measurement of the $2^3P_1 - 2^3P_2$ fine-structure interval of atomic helium. *Phys. Rev. A* **79**, 060503 (June 2009).
17. Smiciklas, M. & Shiner, D. Determination of the Fine Structure Constant Using Helium Fine Structure. *Phys. Rev. Lett.* **105**, 123001 (Sept. 2010).
18. Feng, G.-P., Zheng, X., Sun, Y. R. & Hu, S.-M. Laser-spectroscopy measurement of the fine-structure splitting $2^3P_1 \rightarrow 2^3P_2$ of ^4He . *Phys. Rev. A* **91**, 030502 (2015).
19. Mohr, P. J., Taylor, B. N. & Newell, D. B. CODATA Recommended Values of the Fundamental Physical Constants: 2014. <http://arxiv.org/abs/1507.07956v1> (2015).
20. Kinoshita, T. Fine-structure constant obtained from an improved calculation of the electron g-2. *IEEE Transactions on Instrumentation and Measurement* **46**, 108–111. ISSN: 0018-9456 (Apr. 1997).
21. Hanneke, D., Fogwell, S. & Gabrielse, G. New Measurement of the Electron Magnetic Moment and the Fine Structure Constant. *Phys. Rev. Lett.* **100**, 120801 (12 Mar. 2008).
22. Kruger, E., Nistler, W. & Weirauch, W. Constant by measuring the quotient of the Planck constant and the neutron mass. *IEEE Transactions on Instrumentation and Measurement* **46**, 101–103. ISSN: 0018-9456 (Apr. 1997).
23. Wicht, A., Hensley, J. M., Sarajlic, E. & Chu, S. A Preliminary Measurement of the Fine Structure Constant Based on Atom Interferometry. *Physica Scripta* **2002**, 82 (2002).
24. Gerginov, V. *et al.* Optical frequency measurements of $6s^2S_{1/2} - 6p^2P_{1/2}(D_1)$ transitions in ^{133}Cs and their impact on the fine-structure constant. *Phys. Rev. A* **73**, 032504 (3 Mar. 2006).
25. Bouchendira, R., Cladé, P., Guellati-Khélifa, S., Nez, F. & Biraben, F. New Determination of the Fine Structure Constant and Test of the Quantum Electrodynamics. *Phys. Rev. Lett.* **106**, 080801 (8 Feb. 2011).

26. Liu, W. *et al.* High Precision Measurements of the Ground State Hyperfine Structure Interval of Muonium and of the Muon Magnetic Moment. *Phys. Rev. Lett.* **82**, 711–714 (4 Jan. 1999).
27. Taylor, B. N. & Cohen, E. R. How accurate are the Josephson and quantum Hall effects and QED? *Physics Letters A* **153**, 308–312. ISSN: 0375-9601 (1991).
28. Jeffery, A. M., Elmquist, R. E., Lee, L. H., Shields, J. Q. & Dziuba, R. F. NIST comparison of the quantized Hall resistance and the realization of the SI OHM through the calculable capacitor. *IEEE Transactions on Instrumentation and Measurement* **46**, 264–268. ISSN: 0018-9456 (Apr. 1997).
29. Hodgman, S. S. *et al.* Metastable Helium: A New Determination of the Longest Atomic Excited-State Lifetime. *Phys. Rev. Lett.* **103**, 053002 (5 July 2009).
30. Herman, R. M., Grotch, H., Kornblith, R. & Eberly, J. H. Quantum electrodynamic and semiclassical interference effects in spontaneous radiation. *Phys. Rev. A* **11**, 1389–1396 (Apr. 1975).
31. Cardimona, D. A., Raymer, M. G. & Stroud Jr, C. R. Steady-state quantum interference in resonance fluorescence. *J. Phys. B* **15**, 55 (1982).
32. Sansonetti, C. J. *et al.* Absolute Transition Frequencies and Quantum Interference in a Frequency Comb Based Measurement of the $^{6,7}\text{Li}$ D Lines. *Phys. Rev. Lett.* **107**, 023001 (July 2011).
33. Horbatsch, M. & Hessels, E. A. Shifts from a distant neighboring resonance. *Phys. Rev. A* **82**, 052519 (Nov. 2010).
34. Horbatsch, M. & Hessels, E. A. Shifts from a distant neighboring resonance for a four-level atom. *Phys. Rev. A* **84**, 032508 (3 Sept. 2011).
35. Castilleja, J., Livingston, D., Sanders, A. & Shiner, D. Precise Measurement of the $J = 1$ to $J = 2$ Fine Structure Interval in the 2^3P State of Helium. *Phys. Rev. Lett.* **84**, 4321–4324 (May 2000).
36. Giusfredi, G. *et al.* Present status of the fine-structure frequencies of the 2^3P helium level. *Can. J. Phys.* **83**, 301–310 (2005).
37. Beyer, A. *et al.* Precision spectroscopy of $2S$ - nP transitions in atomic hydrogen for a new determination of the Rydberg constant and the proton charge radius. *Physica Scripta* **2015**, 014030 (2015).
38. Scully, M. O. & Zubairy, M. S. *Quantum Optics* (Cambridge University Press, 1997).
39. Cardimona, D. A. & Stroud, C. R. Spontaneous radiative coupling of atomic energy levels. *Phys. Rev. A* **27**, 2456–2461 (May 1983).

40. Marsman, A., Hessels, E. A. & Horbatsch, M. Shifts due to quantum-mechanical interference from distant neighboring resonances for saturated fluorescence spectroscopy of the 2^3S-2^3P intervals of helium. *Phys. Rev. A* **89**, 043403 (2014).
41. Drake, G. W. F. & Morton, D. C. A multiplet table for neutral helium (^4He I) with transition rates. *Astrophysical Journal, Supplemental Series* **170(1)**, 251–260 (2007).
42. Marsman, A., Horbatsch, M. & Hessels, E. A. Shifts due to neighboring resonances for microwave measurements of the 2^3P fine-structure of helium. *Phys. Rev. A* **86**, 012510 (2012).
43. Marsman, A., Horbatsch, M. & Hessels, E. A. Shifts due to distant neighboring resonances for laser measurements of 2^3S_1 -to- 2^3P_J transitions of helium. *Phys. Rev. A* **86**, 040501 (2012).
44. Pastor, P. C. *et al.* Frequency Metrology of Helium around 1083 nm and Determination of the Nuclear Charge Radius. *Phys. Rev. Lett.* **108**, 143001 (2012).
45. Brown, R. C. *et al.* Quantum interference and light polarization effects in unresolvable atomic lines: Application to a precise measurement of the $^6,7\text{Li}$ D_2 lines. *Phys. Rev. A* **87**, 032504 (2013).
46. Shiner, D. L. & Dixson, R. Measuring the fine structure constant using helium fine structure. *IEEE Trans. Instr. Meas.* **44**, 518–521 (1995).
47. Marsman, A., Horbatsch, M. & Hessels, E. A. Quantum interference effects in saturated absorption spectroscopy of $n = 2$ triplet-helium fine structure. *Phys. Rev. A* **91**, 062506 (6 June 2015).
48. Zelevinsky, T. *Helium 2^3P Fine Structure Measurement in a Discharge Cell; Thesis (supervisor: G. Gabrielse), Harvard University* PhD thesis (Harvard University, 2004).
49. Amaro, P. *et al.* Quantum interference effects in laser spectroscopy of muonic hydrogen, deuterium, and helium-3. *Phys. Rev. A* **92**, 022514 (2 Aug. 2015).
50. Yost, D. C. *et al.* Quantum interference in two-photon frequency-comb spectroscopy. *Phys. Rev. A* **90**, 012512 (1 July 2014).
51. Truong, G.-W., Anstie, J. D., May, E. F., Stace, T. M. & Luiten, A. N. Accurate lineshape spectroscopy and the Boltzmann constant. *Nature Communications*. doi:10.1038/ncomms9345 (2015).
52. Steck, D. A. *Quantum and Atom Optics* available online at <http://steck.us/teaching>. (2015).